MEASURING NEUTRONS IN HEAVY ION COLLISIONS

By

Kuan Zhu

A DISSERTATION

Submitted to
Michigan State University
in partial fulfillment of the requirements
for the degree of

Physics — Doctor of Philosophy

2020

ABSTRACT

MEASURING NEUTRONS IN HEAVY ION COLLISIONS

By

Kuan Zhu

The behavior of the symmetry energy above nuclear saturation density plays a significant role in the properties of neutron stars, the structure of heavy nuclei, and the dynamics of nuclear reactions. To improve constraints on the symmetry energy term in the Nuclear Equation of State (EOS), neutrons and charged-particles were measured with beams of ^{40,48}Ca at 56,140 MeV/u on targets of ^{58,64}Ni and ^{112,124}Sn. The updated High Resolution Array (HiRA10) was used for charged-particle detection. A charged-particle veto wall was designed and constructed to eliminate charged-particle contamination in neutron spectrum measured with the Large Area Neutron Arrays (LANA). Several innovative methods were developed to improve LANA's calibration and neutron/gamma discrimination procedures. Neutron light output are compared to the simulation results from SCINFUL-QMD to test the validity of neutron measurements and calculate the neutron detection efficiency. Various analysis procedures needed for neutron measurements are demonstrated and a preview of the data to come is provided.

ACKNOWLEDGMENTS

First and foremost I could not have accomplished any of this without the guidance of my advisor, Professor ManYee Betty Tsang. She was always available for idea and discussion. I would like to further acknowledge my graduate guidance committee members: William Lynch, Pawel Danielewicz, Mark Dykman and Morten Hjorth-Jensen. Thank you for your time and thoughtful advice. Thanks to all previous and current HiRA lab members: Kyle Brown, Giordano Cerizza, Daniele Dell'Aquila, Genie Jhang, Pierre Morfouace, Chenyang Niu, Clémentine Santamaria, Rensheng Wang, Adam Anthony, Jon Barney, Justin Estee, Sean Sweany, Tommy Tsang, Chi-En Fanurs Teh and Joseph Wieske. It has always been joyful to keep learning and work with you. I would also like to thank the many talented undergraduates I worked with: Corinne Anderson, Hananiel Setiawan, Suhas Kodali, Mira Ghazali, Shuqi Han and Jiashen Ron Tang.

Special thanks to Zbigniew Chajecki group in Western Michigan University. The experiments and the construction of the Charged-Particle Veto Wall can not be accomplished without the strong collaboration with his team.

Last and certainly not least, thank you to all my fellow graduate students for your help and support. Maxwell Cao, Mengzhi Chen, Brandon Elman, Rongzheng He, Kuan-Yu Lin, Hao Lin, Dan Liu, Han Liu, Tong Li, Didi Luo, Xingze Mao, Samuel Marinelli, Pierre Nzabahimana, Omokuyani Udiani, Qi Wang, ChunYan Jonathan Wong, Huyan Xueying and Faran Zhou, thank you for your encouragement and friendship.

This work was in part funded by National Science Foundation (NSF) and Michigan State University (MSU).

TABLE OF CONTENTS

LIST OF TABLES

LIST OF FIGURES

Chapter 1

Introduction

1.1 The Atomic Nucleus

All visible things on earth are made of atoms. Each atom consists of a nucleus at the center and a cloud of electrons. Although this is common knowledge nowadays, atoms were regarded as the most fundamental particles until early 19th century. In 1897, Joseph John Thomson measured the charge-to-mass-ratio (e/m) of cathode ray particle using deflection in both electric and magnetic field. He discovered that the cathode ray particle turned out to be 2000 times lighter than hydrogen (the lightest atom). This discovery, for the first time, showed that atoms are not the indivisible particles of matter. With the discovery of electron, J.J. Thomson incorrectly postulated the "plum pudding model" assuming the negative-charged electrons were distributed throughout the atom in a uniform sea of positive charge. In 1919, with the help of Hans Geiger and Ernest Marsden, Ernest Rutherford devised an experiment that observed the deflection of alpha particles bombarded at a thin sheet of metal foil [17]. He expected that the positively charged alpha particles would pass straight through the foil with little deflection if "plum pudding model" was correct. However, Geiger and Marsden spotted that some alpha particles deflected at very large angles as shown in the left panel of figure 1.1. Considering the mass of an alpha particle is about 8000 times that of an electron, Rutherford realized that the mass of the atom must be concentrated

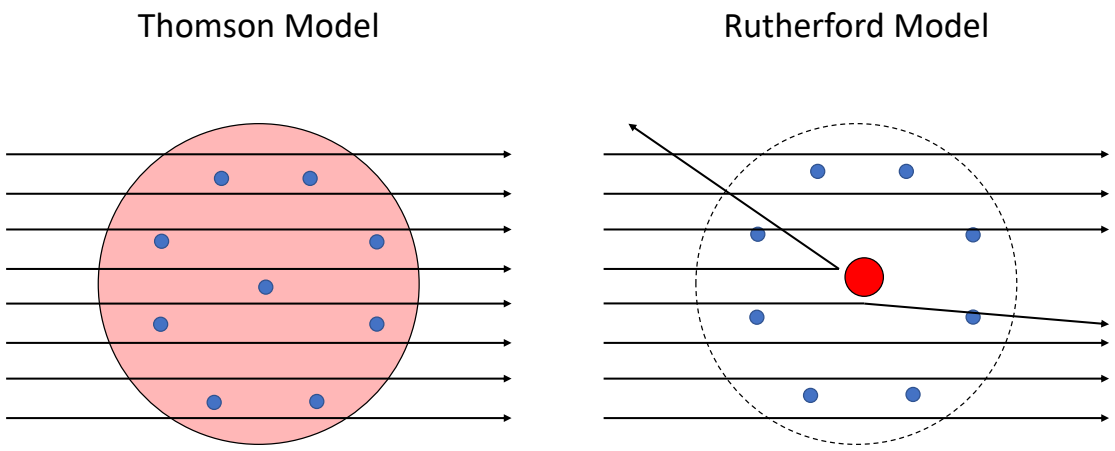

Figure 1.1: The schematic showing the "plum pudding model" proposed by J.J. Thomason (left) and the model proposed by Rutherford (right) after his discovery experiment that showed back scattering of alpha particles. Alpha particles penetrating atoms are represented by horizontal black arrow. Blue circles represents electrons and red area shows the region with positive charge. The sizes of electrons and nuclei are not drawn in scale.

at a small point with positive charge. Almost all of the mass of an atom is located in the nucleus, with a very small contribution from the electron cloud. The radius of the atom can be from about 20,000 (uranium) to 60,000 (hydrogen) times bigger than the nuclear radius, which means the density of nucleus is extraordinarily high, in the order of 10^{17} kg/m^3.

The atomic nucleus composes of even smaller constituents. Every nucleus consists of protons and neutrons. In experiments that impinge alpha particles into pure nitrogen gas, scintillation detectors showed the signatures of typical hydrogen nuclei as a product. In 1919, Rutherford interpreted this observation as the process of alpha particle knocking a hydrogen nuclei out of nitrogen. After observing Blackett's cloud chamber images in 1925, Rutherford realized that the actual process was the opposite case: the alpha particle is first

captured by nitrogen, then a proton is emitted and an oxygen nucleus is left. This was the first reported nuclear reaction: $^{14}N + \alpha = {}^{17}O + p$. Several years after the discovery of proton, in the year of 1930, Walther Bothe and Herbert Becker found that an unusually penetrating radiation was produced when energetic alpha particles were ejected on certain light elements such as beryllium, boron or lithium. In 1932, James Chadwick determined that this new type of radiation was not gamma rays but uncharged particles with about the same mass as the proton [18]. These particles are neutrons. Nuclear strong force binds protons and neutrons together against the repulsive electrical force between the positively charged protons. Studying the inner structure and interaction of such matter constituting of neutrons and protons is the topic of nuclear physics.

1.2 Nuclear Equation of State

People have been attempting to understand nuclei through a variety of models such as liquid drop model (LDM) [19], droplet model (DM) [20], Thomas-Fermi model and density functional methods [21]. Here I will discuss the LDM, the simplest one among them. It was first proposed by George Gamow and further developed by Niels Bohr and John Archibald Wheeler [19]. This model was first formulated in 1935 by German physicist Carl Friedrich von Weizsacker. Based on the short range nature of the nuclear interaction and the saturation property of nuclear matter, LDM treats the nuclei as macroscopic drops of incompressible fluid of nuclear matter [22]. In LDM, the nuclear binding energy (the minimum energy required to completely disassemble a nucleus into separate protons and neutrons) of a nucleus

of protons Z, neutrons N and mass A=Z+N is written as:

$$B(A,Z) = a_v A + a_s A^{\frac{2}{3}} + a_c \frac{Z^2}{A^{\frac{1}{3}}} + a_a \frac{(N-Z)^2}{A} + O(A,Z) \tag{1.1}$$

The first term with a_v is the volume term: the binding energy is proportional to the volume of the nuclei, so it is also proportional to the mass A, the total number of nucleons. The second term with a_s is a correction to the volume term: the strong force that binds the nucleons together has a very limited range and a nucleon only interact strongly with its closest neighbors. Therefore, the nucleons on the surface of the drop has less neighbors to interact with, thus reducing the binding energy. The third term starting with a_c takes the Coulomb repulsion between protons into account. The next term with a_a is known as the asymmetry term. Based on the Pauli exclusion principle, no two identical fermions can occupy the same quantum state within a quantum system simultaneously. Consider a nucleus with imbalanced number of protons and neutrons, e.g., with more neutrons ($N > Z$), neutrons have to occupy higher single particle energy levels than protons, reducing its binding energy, when compared to a nucleus with equal number of protons and neutrons ($N = Z$). We call the excess in the proton or neutron number as the isospin asymmetry $\delta = \frac{N-Z}{Z}$. The last term $O(A,Z)$ is called pairing term to refine the model. Due to Pauli principle, a nucleus would have lower energy if the number of protons with spin up equals to the number of protons with spin down.

To describe the collective state of a macroscopic system such as neutron star, we must move beyond the liquid drop model. Nuclear equation of state (EOS) is used to describe the relationship between pressure, temperature, energy, and density of the system. Nuclear EOS can be approximately expressed (at zero temperature) in terms of the sum of energy

from a term that describes the symmetric nuclear matter with equal densities of neutrons and protons and energy from an asymmetric term consisting of nuclear matter with different densities of proton and neutron:

$$E(\rho, \delta) = E(\rho, \delta = 0) + S(\rho)\delta^2 \tag{1.2}$$

Isospin asymmetry δ here is more generally written as:

$$\delta = \frac{\rho_n - \rho_p}{\rho_n + \rho_p} \tag{1.3}$$

where ρ_n and ρ_p is the density of neutron and proton. We call the later term $S(\rho)\delta^2$ the symmetry energy. It is approximately the energy cost of converting symmetric nuclear matter into pure neutron matter. Nuclear EOS governs many fundamental properties of the nuclear matter and plays a crucial role in understanding not only terrestrial nuclei and nuclear reaction process, but also the evolution of nuclear structure and many astrophysical objects. Over the last four decades, much knowledge about the $E(\rho, 0)$ term in Eq. 1.2, which is the EOS of symmetric nuclear matter, has been obtained through the hard work of scientists in both nuclear physics and astrophysics [23].

In more recent years, significant efforts have been taken to explore the relatively poorly known $S(\rho)$. The symmetry energy plays a fundamental role especially in the stability of neutron stars. The pressure that supports the neutron star against the collapse from gravitational force, mainly comes from the symmetry energy [24]. It also strongly influences neutron star structure, radius, moment of inertia, cooling process and prevents the collapse of a neutron star into a black hole [25, 26, 27, 28, 29, 30]. The first observation of a neutron-

star merger event in 2017, GW170817 (GW), has provided new insights to the equation of state of neutron star [31, 32, 33, 34, 35, 36]. Much progress has been made in constraining the two coefficients S_0 and L in the Taylor expansion of $S(\rho)$ around the saturation density ρ_0 (0.16 nucleon/fm^3):

$$S(\rho) = S_0 + \frac{L}{3\rho_0}(\rho - \rho_0) + \frac{K_{sym}}{18\rho_0}(\rho - \rho_0)^2 + O((\rho - \rho_0)^3) \tag{1.4}$$

Constraints of S_0 and L at sub-saturation density was obtained through various types of laboratory experiments including excitation energies of Isobaric Analog States (IAS) [37], Pygmy Dipole Resonances (PDR) [38, 39, 40], atomic mass analyses [41, 42], electric dipole polarizability [43, 44], neutron skin thickness of heavy nuclei [45] and isospin diffusion in heavy ion collision [46, 47, 48, 49, 50].

While much knowledge is obtained about $S(\rho)$ at sub-saturation density, the high density behavior of $S(\rho)$ remains rather uncertain. A set of Skyrme parameterizations, which is selected based on the fit of binding energy difference between ^{100}Sn and ^{132}Sn nuclei, gives very different predictions about the energy per nucleon in pure neutron matter at densities above saturation density [3]. Figure 1.2 shows that the uncertainties remain large when $S(\rho)$ with $\rho > \rho_0$ with selected Skyrme interactions from Ref. [2]. For simplicity, it is common to write the density dependence of $S(\rho)$ in the following form:

$$S(\rho) = S_{kin}(\frac{\rho}{\rho_0})^{\frac{2}{3}} + S_{int}(\frac{\rho}{\rho_0})^{\gamma} \tag{1.5}$$

The first term with S_{kin} is the Thomas-Fermi kinetic energy. In a uniform system of Fermions of spin S = $\frac{1}{2}$ in 3 dimensions, the relationship between Fermi momentum k_F and the

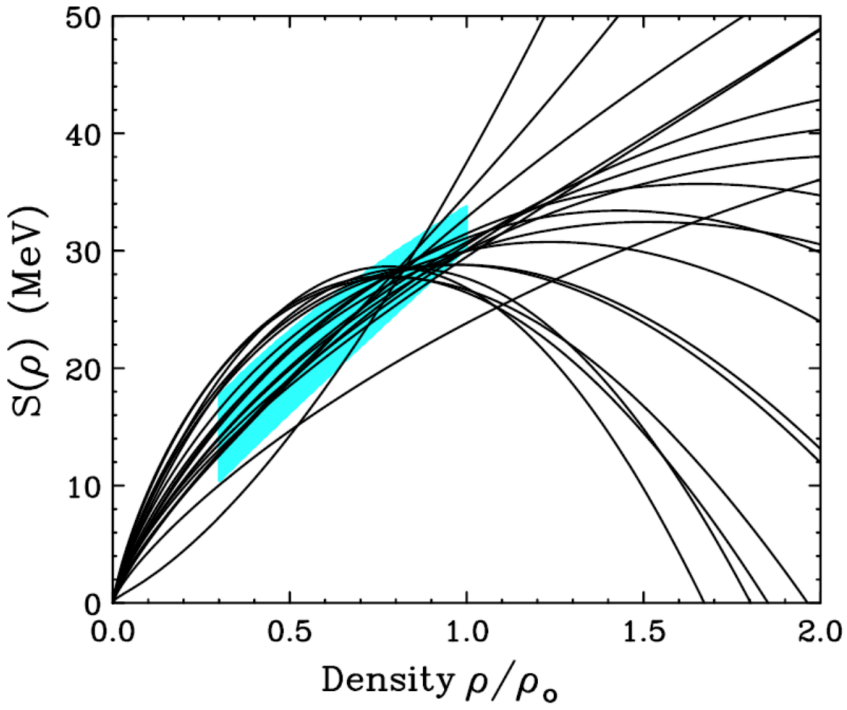

Figure 1.2: Density dependence of the symmetry energy from the Skyrme interactions used in Ref. [2].The shaded region is obtained from HIC experiments. Picture is adopted from Ref. [3].

density ρ is: $k_F = 3\pi\rho^3$. Then the kinetic energy is proportional to the square of the Fermi momentum ${k_F}^2$. Overall, the kinetic energy part in $S(\rho)$ depends on $\rho^{\frac{2}{3}}$. The second term with S_{int} is the interaction energy term. It is modeled to have power law of density dependence with factor γ. The value of γ is usually chosen between 0.5 to 2. The symmetry energy is "soft" when $\gamma < 1$ and "stiff" when $\gamma > 1$.

It is worth mentioning that the symmetry energy $S(\rho)$ is closely related to the neutron-proton effective mass splitting. From the Fock exchange term, finite range and correlation effects, the nuclear mean-field potential has momentum dependencies [51, 52, 53, 54]. The concept of effective mass was introduced to simplify the description of nucleons that are moving in a momentum-dependent mean-field potential. Consider the following Hamilton's

Equation for a nucleon:

$$\dot{x} = \frac{\partial H}{\partial p} \tag{1.6}$$

$$= \frac{p}{m} + \frac{\partial V}{\partial p} \tag{1.7}$$

Define the effective mass m^* such that:

$$\dot{x} = \frac{p}{m^*} \tag{1.8}$$

Combine Eq. 1.7 and Eq. 1.8, we have:

$$\frac{m^*}{m} = \frac{1}{1 + \frac{m}{p}\frac{\partial V}{\partial p}} \tag{1.9}$$

Nucleons can be described as moving with their effective masses, instead of with their free masses in a momentum-dependent potential. An isoscalar effective mass m_s^* is derived from the mean-field potential with $\frac{m_s^*}{m_N} \approx 0.65 - 0.75$ where m_N is the nucleon mass [7, 55]. Due to the momentum dependencies in the isovector mean-field potential, the effective masses for neutron m_n^* and proton m_p^* are different from each other [52], resulting in the effective mass splitting:

$$\Delta m_{np}^* = \frac{m_n^* - m_p^*}{m_N} \tag{1.10}$$

Based on the well-known Lane potential [56], the single nucleon potential $V_\tau(\rho, k, \delta)$ in

Equ. 1.9 can be well approximated by:

$$V_\tau(\rho, k, \delta) = V_0(\rho, k) \pm V_{sym}(\rho, k) \cdot \delta \tag{1.11}$$

where the $V_0(\rho, k)$ is the nucleon isoscalar potential and $V_{sym}(\rho, k)$ is the isovector (symmetry) potential for nucleons with momentum k and isospin asymmetry δ at density ρ. $\tau = n$ for neutrons and $\tau = p$ for protons. With the isoscalar asymmetry δ considered, equations 1.10 can be written as:

$$\Delta m^*_{np} = \frac{\frac{m_N}{\hbar^2 k_F}(dV_p/dk - dV_n/dk)}{(1 + \frac{m_N}{\hbar^2 k_F} dV_p/dk)(1 + \frac{m_N}{\hbar^2 k_F} dV_n/dk)}\Bigg|_{k_F} \tag{1.12}$$

For practical systems, δ is small and can be neglected in the denominator, but the leading order term in the numerator is proportional to δ. So to a good approximation:

$$\Delta m^*_{np} \approx -2\delta \cdot \frac{\frac{m_N}{\hbar^2 k_F}\frac{dV_{sym}}{dk}}{(1 + \frac{m_N}{\hbar^2 k_F} dV_p/dk)(1 + \frac{m_N}{\hbar^2 k_F}\frac{dV_0}{dk})^2}\Bigg|_{k_F} \tag{1.13}$$

$$= -2\delta \cdot (\frac{m^*_s}{m_N})^2 \cdot (\frac{m_N}{\hbar^2 k_F}\frac{dV_{sym}}{dk})\Big|_{k_F} \tag{1.14}$$

Here, m^*_s is the nucleonic effective mass in symmetric matter, where V_{sym} vanishes. On the other side, the symmetry energy $E_{sym}(\rho)$ and its slope $L(\rho)$ can be expressed as:

$$E_{sym}(\rho) = \frac{1}{3}\frac{\hbar^2 K_F^2}{2m_N} + \frac{1}{2}V_{sym}(\rho, k_F) \tag{1.15}$$

$$L(\rho) = \frac{2}{3}\frac{\hbar^2 K_F^2}{2m_N} + \frac{3}{2}V_{sym}(\rho, k_F) + \frac{\partial V_{sym}}{\partial k}\Big|_{k_F} k_F \tag{1.16}$$

Combining equations 1.12 to 1.16, the effective mass splitting depends on asymmetry δ

in such form [57]:

$$\Delta m^*_{np} \approx \delta \cdot \frac{3E_{sym}(\rho_0) - L(\rho_0) - \frac{1}{3}\frac{m_N}{m^*_0}E_F(\rho_0)}{E_F(\rho) \cdot (\frac{m_N}{m^*_0})^2} \tag{1.17}$$

where $m*_0 = 0.7m_N$ at normal density.

This effect influences the magnitude of shell effects in nuclei far from stability and some properties of neutrons star especially the cooling process via neutrino emission [58, 59]. However, both the sign and magnitude of the effective mass splitting Δm^*_{np} are poorly determined. Different Skyrme parameterizations contained different effective mass splitting. Moreover, some microscopic calculations performed in Landau-Fermi-liquid theory [60] and the nonrelativistic Brueckner-Hartree-Fock approach [61] have predicted that $m^*_n > m^*_p$ while other calculations using relativistic mean-field theory and relativistic Dirac-Brueckner theory [52, 62] predict that $M^*_n < M^*_p$. Additional experimental data and theoretical studies are urgently needed to resolve this issue.

1.3 Probing Effective Mass Splitting in Heavy Ion Collision

Heavy Ion Collision (HIC) is one of the main tools used to explore the density dependence of the symmetry energy and the momentum dependence of the symmetry potential. A large range of densities can be obtained in HIC by choosing different projectile-target systems [63, 64, 65] and bombarding energies. In the energy above the Fermi energy but below around 150 MeV per nucleon, nucleons that participate in the collision first form a compressed, high-density region, then expand with the emission of light clusters. The emitted particles carry the information of nuclear symmetry energy because the motions of ejected particles

are determined by the nuclear interaction during such compression-expansion process. The measurements of particles emitted from HIC include neutron/proton yield ratio spectra and isospin diffusion. This strategy has been successfully applied to constrain the symmetry energy at sub-saturation density using Sn+Sn collisions [64, 66, 47, 67, 68, 69].

Transport models that take EOS as an essential input is used to interpret the results measured in HIC and to constrain EOS quantitatively. Calculations performed in transport models have been successful in describing observables in HIC such as isoscaling ratios and elliptic flow [50, 70]. Calculations typically employs a set of parameterizations such as Skyrme interactions that characterize the density dependence of the nuclear matter energy including the symmetry energy. Aside from the density dependence of the symmetry energy, other inputs such as neutron-proton effective mass splitting Δm^*_{np} that results from a momentum-dependent mean-field potential and in-medium nucleon-nucleon cross sections δ_{NN} also impact the propagation of nucleons in collisions. Results from transport model calculation predict that neutrons with high momentum emitted from the compressed participant region will experience a more repulsive potential thus a higher acceleration process if $m^*_n < m^*_p$, compared to protons with same momentum [4, 22]. This effect will enhance ratio of neutron over proton (n/p) at high momentum for $m^*_n < m^*_p$ and calculations using $m^*_n > m^*_p$ give predictions that the acceleration of protons are enhanced, resulting in a lower n/p spectral ratio. If we use M to represent the multiplicities for a certain particle, the differential yield defined as $Y(n) = \frac{dM_n}{dE}$ and $Y(p) = \frac{dM_p}{dE}$ and the spectral yield ratio of n/p is written as:

$$R_{n/p} = \frac{Y(n)}{Y(p)} = \frac{dM_n/dE}{dM_p/dE} \tag{1.18}$$

Eq. 1.18 is called "single ratio". Another observable is defined as "double ratio":

$$DR(n/p) = \frac{(R_{n/p})_{system1}}{(R_{n/p})_{system2}} \tag{1.19}$$

which takes the ratio of single ratios from two reaction systems. Double ratio is commonly used to take the advantage of cancellation of systematic errors which are difficult to determine experimentally such as detector efficiencies and to a certain extent, inadequacies in models. such as the Coulomb effects and clustering mechanisms.

Figure 1.3 shows simulation results of $R_{n/p}$ and $DR_{n/p}$ using Improved Quantum Molecular Dynamics (ImQMD) model [71, 72, 73] with two Skyrme interaction parameter sets, SLy4 [74] and SkM* [75]. SLy4 and SkM* have similar symmetry energy coefficient S_0, slopes of symmetry energy L and isoscalar effective mass m^*, i.e., $S_0 = 32 \pm 2$MeV, $L = 46$MeV and $m^*/m_N = 0.7 \pm 0.1$. However, the effective mass splitting is different with $m_n^* < m_p^*$ for SLy4 and $m_n^* > m_p^*$ for SkM*. In figure 1.3, $DR(n/p)$ is roughly flat or decrease slightly with nucleon kinetic energy for SkM* while they increase for SLy4. The sensitivity of the $DR(n/p)$ to effective mass splitting decrease with greater incident beam energies due to increase in nucleon-nucleon scattering [4]. These calculations suggest incident energy less than 200 MeV is best for the effective mass splitting study.

1.4 Neutron Detection

Neutron detection is very difficult and this is why the discovery of neutron was relatively late in 1932 by Chadwick. Unlike protons and other charged-particles, neutron has no electric charge and does not interact with other particles through electromagnetic force.

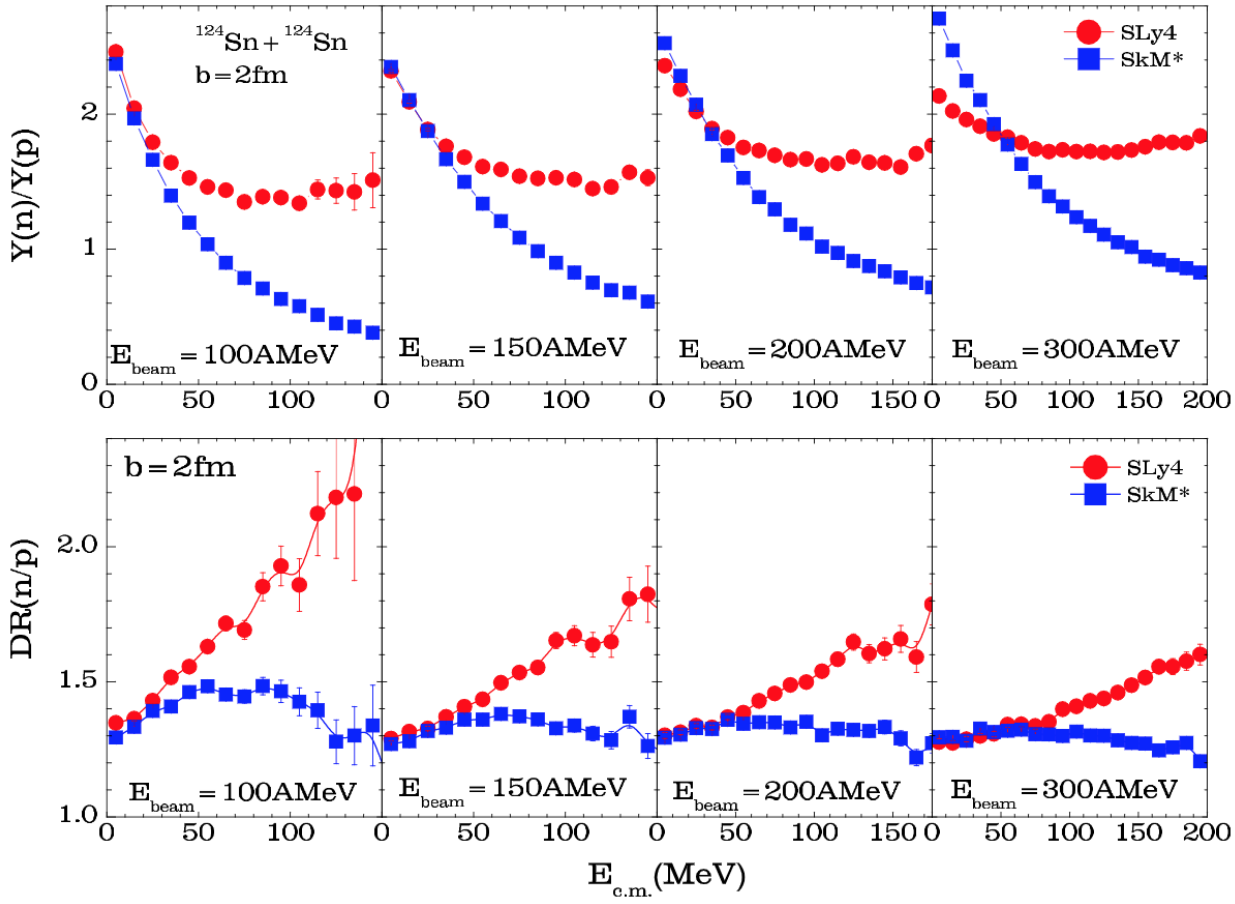

Figure 1.3: (top panels) Y(n)/Y(p) ratios as a function of kinetic energy for ^{124}Sn+^{124}Sn at b=2fm. (bottom panels) DR(n/p) ratios as a function of kinetic energy. From left to right, the beam energies are 100 MeV, 150 MeV, 200 MeV, 300 MeV per nucleon. Figure is adopted from Ref. [4].

Neutrons are stable when bounded in nuclei. However, as a free particle, neutron beta decays with a half-life of about 880 s. It primarily interacts with other particles by strong force (hadronic interaction), which is much stronger than electromagnetic interaction but with very limited range of a few fermi. As neutral particles, neutrons do not ionize directly and their paths are weakly affected by electric and magnetic fields. They are usually detected by nuclear interactions that produce secondary charged-particles with relatively low interaction probability. Because the nuclear force has extremely short range, neutrons need to be very close within around 10^{-15} m of another nucleus in order for scattering to take place. Given

the radius of a nucleus is at least 10,000 times smaller than the radius of an atom, the probability of neutrons interact with normal material is relatively low. Thus, the detection of neutrons represents a considerable technical challenge.

The energy of neutrons to be detected can vary from below meV (milli-electron volt) called ultracold neutrons up to more than TeV (Tera-electron volt) which are mainly created in large accelerators or in certain astrophysical activities. Neutrons are commonly classified according to their energies as listed in the following table [1]:

Designation	Neutron Energy
Ultracold neutrons	< 0.2 meV
Cold neutrons	0.2 meV - 2 meV
Thermal neutrons	2 meV - 100 meV
Epithermal neutrons	100 meV - 1 eV
Intermediate neutrons	1 eV - 10 keV
Fast neutrons	10 keV - 20 MeV
High-energy neutrons	> 20 MeV

Table 1.1: Neutron designation table for different energy ranges. This table is adopted from Ref. [1]

Neutrons at different energy range require different detection techniques. The energy range of neutrons we measured in our experiment is from tens of MeV to a couple hundred MeV; the fast and high energy neutrons. The principles of detection of fast neutrons are based on ionizing radiation. Because neutrons do not directly ionize in material, charged-particles need to be induced by neutrons first, and then the energy of charged-particles are converted into different types of signal through ionization processes. The main interactions of neutrons with nuclei are the following three processes: elastic scattering, inelastic scattering and radiative neutron capture [1]. The most important process for such neutrons is elastic scattering on light target nuclei, especially elastic n-p scattering due to the higher cross-sections compared to other reaction channels, as shown in figure 1.4.

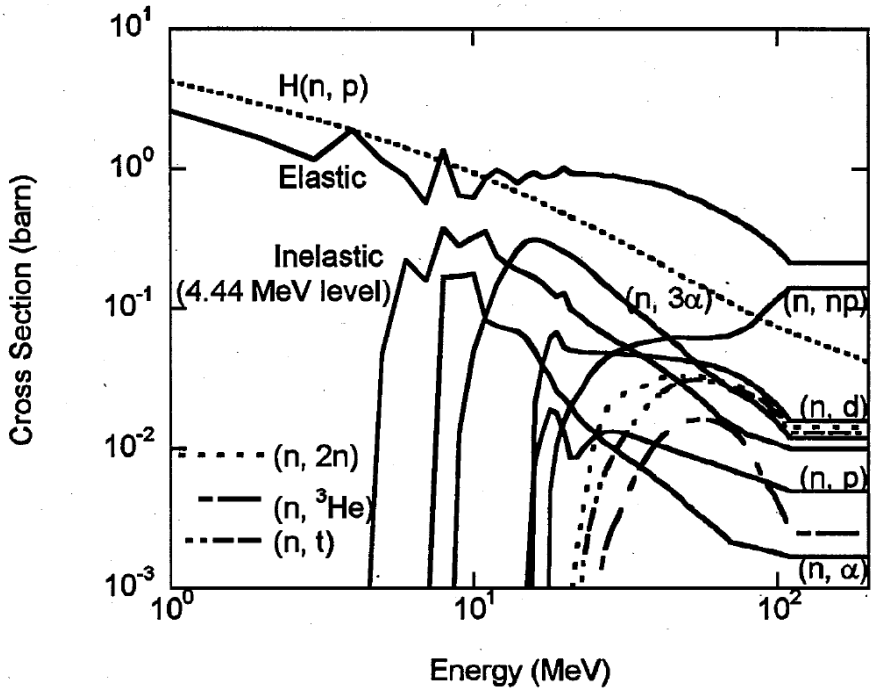

Figure 1.4: Neutron reaction cross sections adopted in SCINFUL-QMD model. Picture is adopted from Ref. [5].

Popular types of neutron detectors include gas-filled detectors, semiconductor and scintillators [76]. Organic plastic and liquid scintillators composed of large percentage of hydrogen are widely used in neutron measurement. Not only are they fast detectors, a requirement for Time of Flight (ToF) measurement to determine the energy of the detected neutrons, but they are robust and relatively cost effective to build a large detector like LANA. Since recoiling protons is the dominant neutron interaction in scintillators, neutrons and charged-particles emitted from nuclear reaction cannot be distinguished from the light they produced in the scintillator. This is why we designed and built a thin plastic scintillator wall which has 1% neutron detection efficiency and 100% charged-particle detection efficiency. It will be placed in front of existing Large Neutron Area Array (LANA) at NSCL to provide extra information in order to distinguish and veto charged-particle events from neutrons detected in LANA. This wall is called Charged Particle Veto Wall (VW) and its detail will be presented

in Chapter 2.

1.5 Improvements from Previous Experiment

Due to difficulties in measuring neutrons, few experimental data on neutron and protons yield or spectra ratios exist. In 2009, the HiRA group measured the neutron and protons spectra emitted from Sn+Sn reactions [6, 7]. Conclusions from that study regarding the effective mass are ambiguous both due to quality of the data. In the current experiment, We studied smaller, near symmetric reaction systems such as Ca+Ni and Ca+Sn to allow extensive calculations with CPU intensive transport models such as the AMD models which have sophisticated treatment of cluster production. We also study very asymmetric systems such as Ca+Sn to study the in-medium NN cross sections. Based on experience with previous experiments, we have also made major improvement in the experimental setup regarding detection of charged particles and the neutrons. The work of this thesis mainly focuses on the improvement made in neutron detection while the thesis of Sean Sweany focuses on the improvement in detecting charged particles in this experiment.

Fig. 1.5 shows the $DR(n/p)$ spectral double ratios measured in previous experiment on central collisions of 124Sn+124Sn and 112Sn+112Sn systems at E/A=120 MeV. The red and blue shaded bands correspond to the predictions from ImQMD using SLy4 and SkM* interactions. As expected the results split starting at center of mass energy of the nucleons around 50 MeV/u. Unfortunately due to limitation of the charged particle detector, the data does not extend beyond 80 MeV/u in the center of mass energy. The large statistical uncertainties mainly arise from contamination of charged particles in the neutron spectra due to deficiencies of the old veto arrays. Because of the difficulties for most transport models

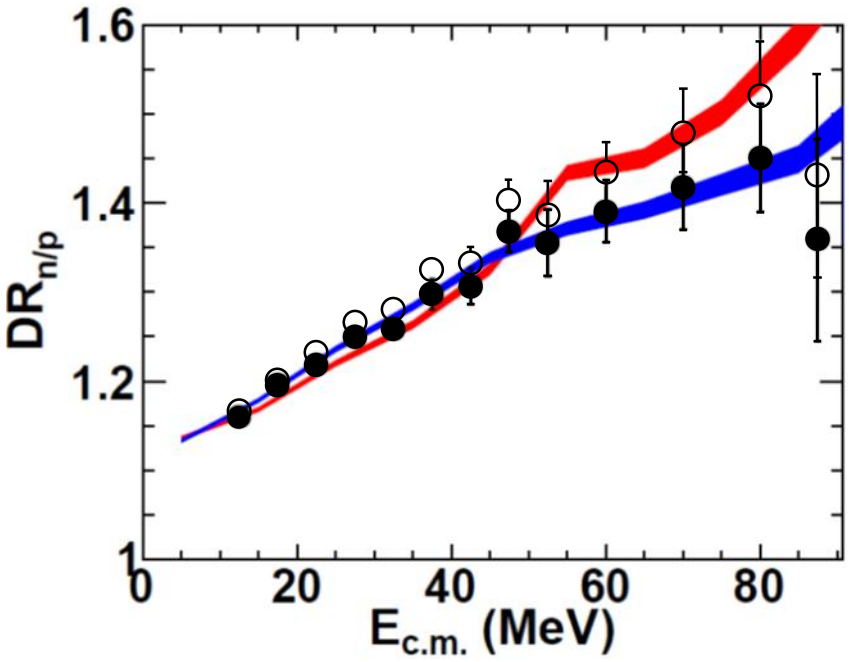

Figure 1.5: neutron/proton double ratio for $^{124}Sn + ^{124}Sn / ^{112}Sn + ^{112}Sn$ reaction systems at 120 MeV/u for central collisions. The symbols are experimental data. Red line shows calculation using SLy4 which has $m_n^* < m_p^*$ while blue line comes from calculation using SkM* which has $m_n^* > m_p^*$. The picture is adopted from Ref. [6]. Open circles are the original version and the close circles are data of the most updated version. The original data points did not take into account the efficiency corrections for charged-particles [7, 8].

in producing the relative abundances of light isotopes in HIC, instead of comparing free neutrons and protons spectra, we use the observable the coalescence invariant (CI) neutron and proton spectra by combining the free nucleons with those bound in light isotopes with $1<A<5$ are calculated according to Ref. [6]. The open and closed symbol correspond to data before and after correction to the charged particles due to reaction loss in the detector. Before the corrections were applied, the data (open points) seem to be more consistent with the SLy4. After the corrections, the data appear to be more consistent with the SkM* even though both sets of double ratio data are within experimental uncertainties. The observable double ratios work as designed that most of the systematic errors are cancelled out. The residual errors are associated with the construction of coalescence invariant of the neutron and proton yields that involve clusters. Subsequent efforts to use Bayesian analysis [7] failed to extract a definitive conclusion on the sign and magnitude of the effective mass splitting. However, the previous experiment paved a path forward to measure the neutron to proton ratios using the HiRA and LANA arrays.

To improve the design of the previous experiment, we need to:

1. Improve the quality of the neutron spectra and the statistical errors so that we can construct the free neutron/proton ratios rather than relying completely on the coalescence invariant of the n and proton yields. At high nuclear energy, contribution of the clusters on the n/p ratios are minimal since the production cross-sections of clusters drop off much faster than neutron and protons. Thus at high energy, the free n/p ratios can be compared to the n/p ratios from models. This is the subject of this section.

2. Extend the energy spectra of the charged particles to the high energy region where the effective mass splitting effects becomes larger. The improvements of charged-particle measurements including extending the length of crystal to allow the detection of higher

energy charged-particles and correction of reaction losses in the detector will be detailed in Sean Sweany's thesis.

To improve neutron detection from previous experiment, we must understand the problems. The top panel of Fig. **??** shows the layout of full setup in previous experiment and the bottom panel is the image of veto arrays (left) and veto paddles (right) used to veto charged-particles in the forward angle LANA wall and backward angle LANA wall respectively. The forward angle veto arrays are made of 13 BC-408 scintillator bars of 3/8 inch thickness. Each bar is a 2.35×27.4 cm^2 rectangular. The backward angle veto array consists of four 16×16 cm^2 square BC-408 scintillator paddles. The forward LANA covers angles from 7° to 29° while the backward LANA covers angles from 34° to 59°.

The forward veto array covers the angle from 8° to 30° in lab frame so the edges of forward LANA are not well covered. There were also several gaps between veto paddles shadowing the backward LANA. These problems can be partly rectified by excluding the exposed edges and gaps in the offline analysis. The major problem is the long distances (more than 5 meters) between the veto arrays/paddles and the neutron walls. Because of the coarse granularity of veto position resolutions, the one-to-one charged-particle hit correlation constructed for the hits on veto arrays/paddles and the LANA is ambiguous. This means for events with both neutrons and charged-particles hitting the LANA, we were not able to identify charged-particles based on their hit positions on veto arrays/paddles. Therefore, for high multiplicity events, we needed to either abandon the whole events or tolerated the charged-particle contamination (this is especially true for the forward veto array because every event is accompanied by at least one charged-particles hitting it). Considering LANA detecting charged-particle at 100% efficiency and neutron at less than 10%,even a 90% vetoing accuracy is not acceptable. Figure 1.6 shows the charged-particle contamination over a wide

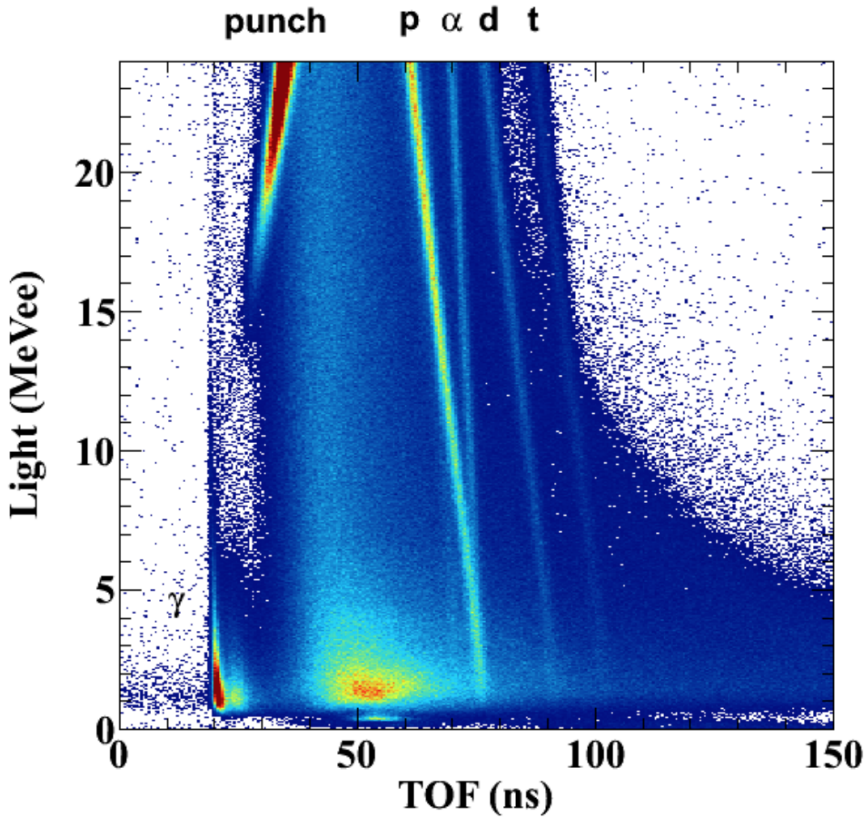

Figure 1.6: Neutron Wall light vs TOF, where TOF is the time of flight for the observed particle to travel to the neutron walls. The prompt γ ray peak, charged-particle punch-through, and charged particle stopping PID lines are marked. Picture is adopted from Ref. [9].

region of the neutron spectrum in that experiment.

To completely veto the charged particles from the neutron detectors, we designed and constructed a large Charged-Particle Veto Wall to be placed about 0.5 m in front of LANA, the closest distance that is mechanically feasible. This new veto wall was designed to fully cover LANA without gaps. Moreover, instead of the forward-backward wall configuration (Figure **??**) we used in previous experiment, we focus on detecting neutrons in one angle, around 90 deg in the center of mass. The nesting of both walls increase our efficiencies by nearly a factor of two.

1.6 Organization of Dissertation

The rest of this thesis is organized as follows. Chapter 2 provides the details of experimental setup used in experimental campaign during February and March of 2018 at NSCL. The experimental setup consists of Microball, HiRA10, LANA, Forward Array and Charged-Particle Veto Wall, the last of which was designed and constructed specially for the experiments. This thesis mainly focuses on the neutron wall detector with the veto wall and the forward array. Analysis of charged particles from microball and HiRA10 is the thesis topic for another student, Sean Sweany. Chapter 3 details the analysis with LANA and the energy calibration of the Charged-Particle Veto Wall. A calibration method using high-energy muons produced in cosmic ray showers to calibrate the position, time and light output of LANA is described. Chapter 4 presents the results of the analysis. Finally, Chapter 5 contains the summaries and conclusions.

Chapter 2

Experimental Details

The experimental campaign took place from the beginning of February to the end of March in 2019 at NSCL S2 vault. K1200 cyclotron produced ^{40}Ca and ^{48}Ca beams at E/A = 56 MeV and 140 MeV which were incident on ^{58}Ni, ^{64}Ni, ^{112}Sn and ^{124}Sn targets. The thicknesses of these four targets are: 5.0 mg/cm^2 for ^{58}Ni, 5.3 mg/cm^2 for ^{64}Ni, 6.1mg/cm^2 for ^{64}Ni and 6.47mg/cm^2 for ^{124}Sn. There are 2 (beam isotopes) $\times$ 2 (beam energies) $\times$ 4 (targets) = 16 reactions in the experiment. Targets are located at the center of a thin-wall aluminum chamber. The experimental setup consists of the the following five main detector systems: (1) Microball, for impact parameter determination (2) HiRA10 (High Resolution Array with 10 cm long CsI crystals), for measuring charged-particles (3) Forward Array, for reaction start time determination in Time of Flight (ToF) technique to measure the energy of neutrons (4) LANA (Large Area Neutron Array), for neutron detection, providing stop time in ToF method. (5) a large Charged-Particle Veto Wall placed in front of LANA to veto charged-particles in offline analysis.

Figure 2.1 shows a picture of experimental setup taken right after the experiment campaign finished and with the lid of the vacuum chamber removed. Each detector system is labelled. Figure 2.2 shows the top view of the relative positioning of every detector systems. The remainder of this chapter details the design of each detector system.

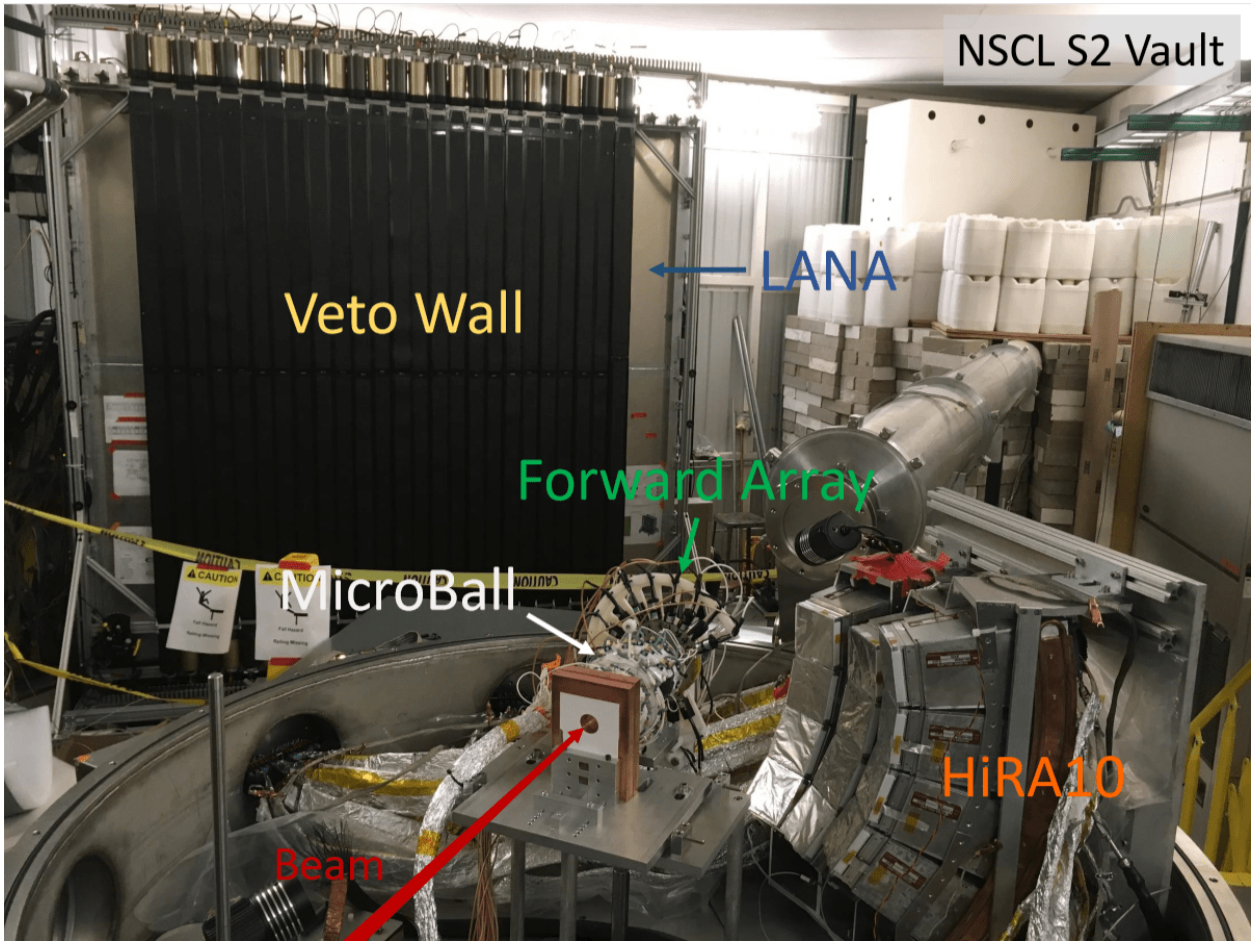

Figure 2.1: Experimental setup overview. Microball, Forward Array and HiRA10 are placed inside a vacuum chamber. The target is inside the Microball at the center of the chamber. The lid of the vacuum chamber is removed for this picture.

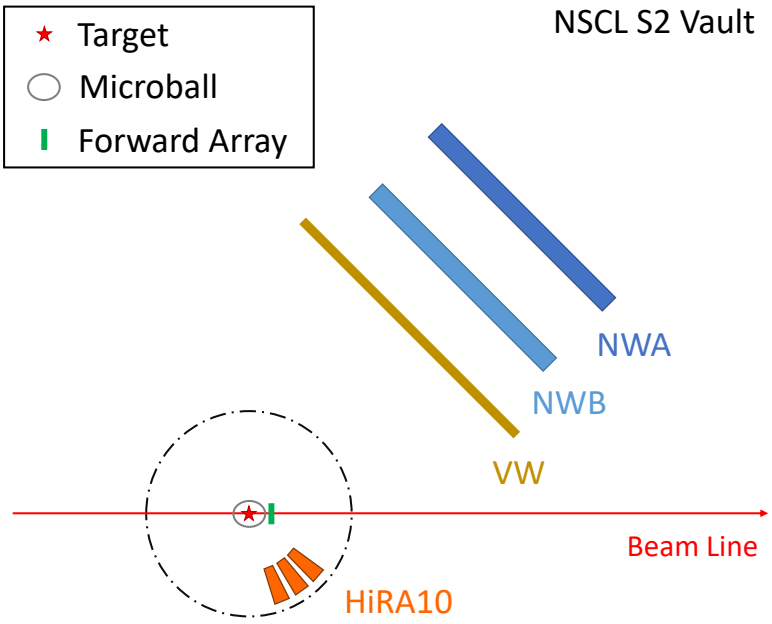

Figure 2.2: A schematic showing the experiment setup. It is a not-to-scale version of Figure 2.25.

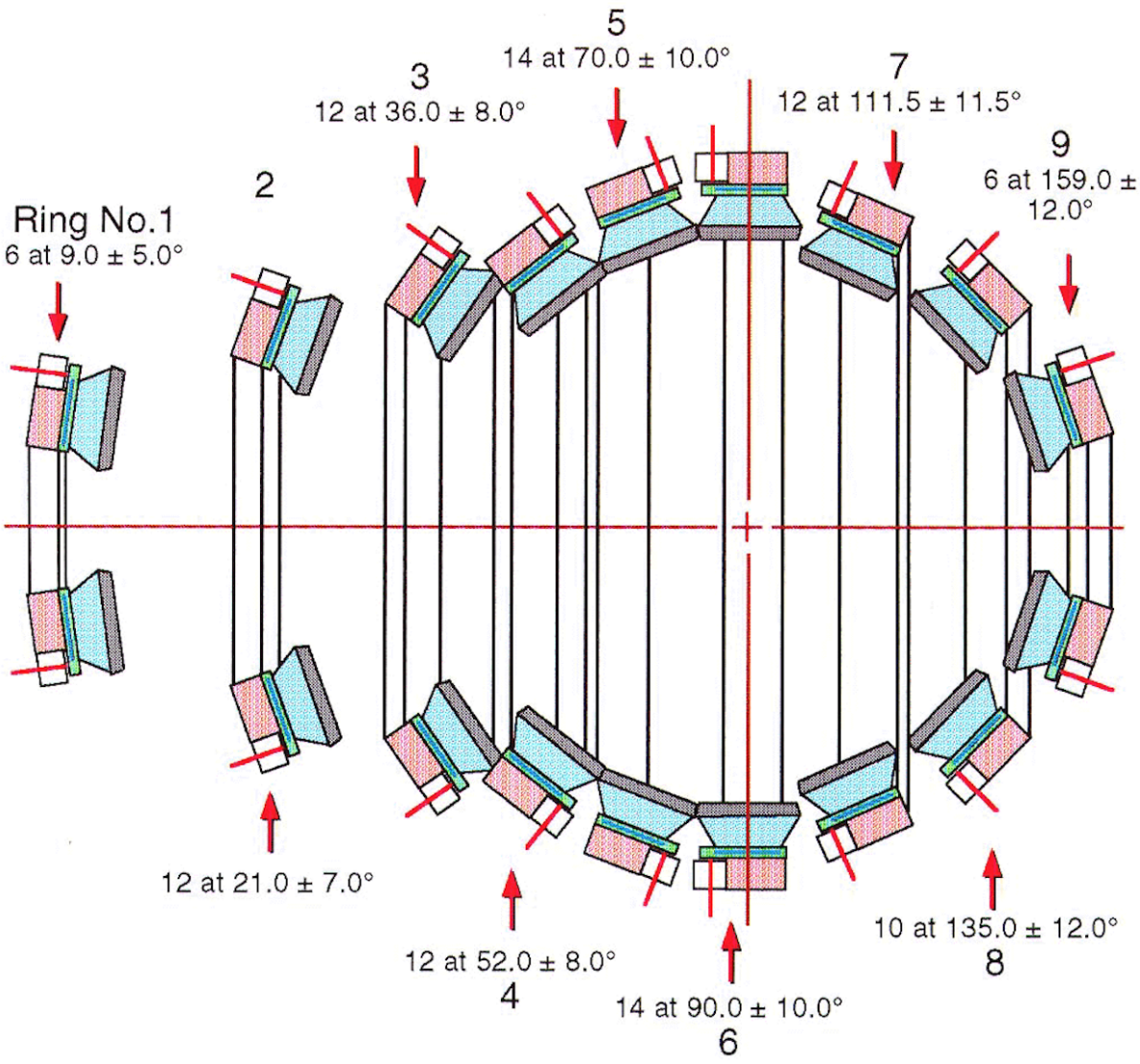

Figure 2.3: Schematic diagram showing a vertical section of the Microball. The CsI(T1) crystals are shown in grey. The blue trapezoids behind crystals are light guides. The beam enters from the left. The numbers 1,2,3,to 9 are the ring numbers. The polar angular coverage for each ring are also shown together with the number of crystals contained in each ring. This picture is adopted from Ref. [10].

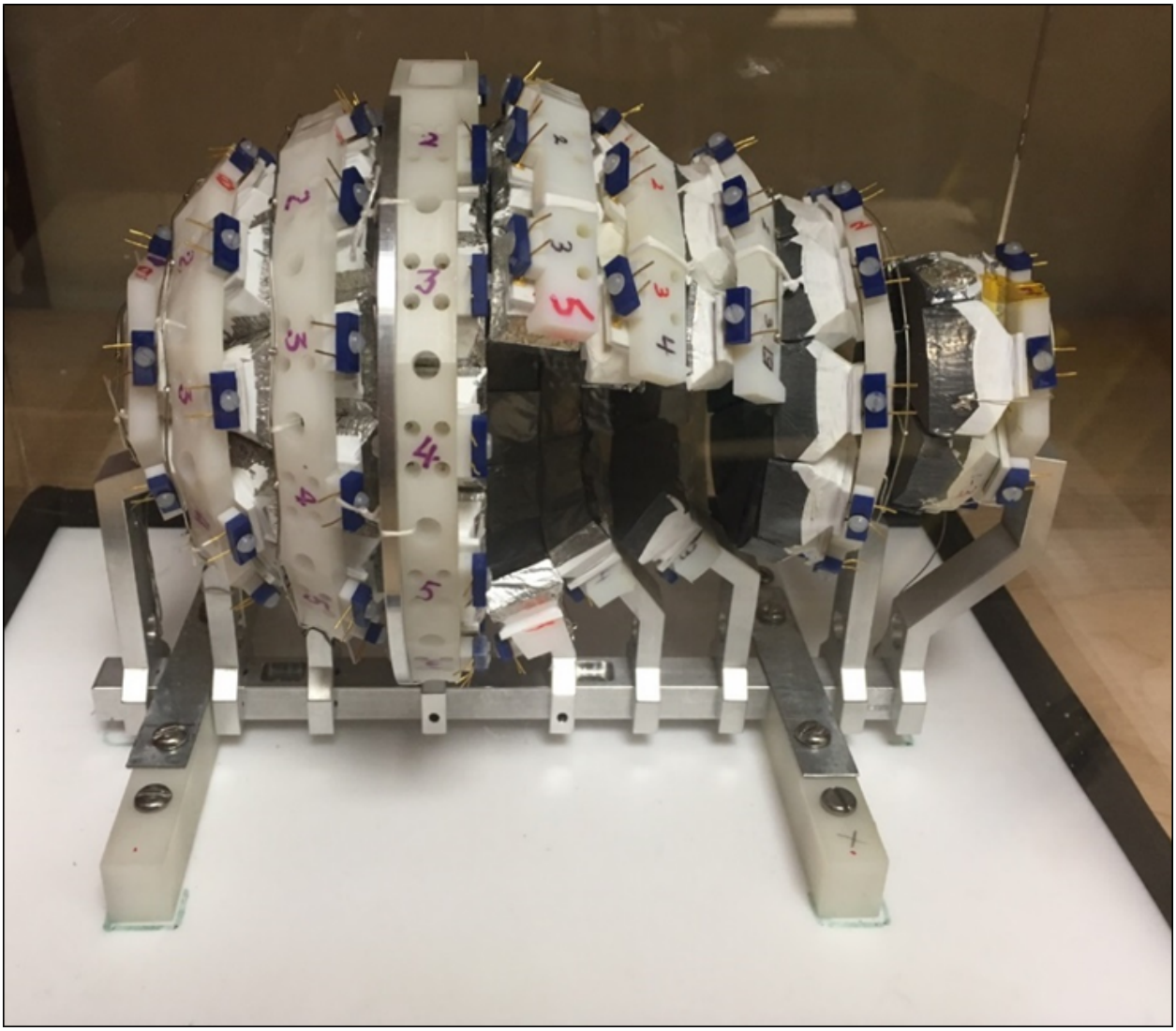

Figure 2.4: Ten microball detectors removed to allow charged particles emitted in reactions to be detected by HiRA10 without materials without going through blocking materials. The beam enters from left.

2.1 Microball

The original Microball, on loan from Washington University at St. Louis, is made of 95 CsI(T1) crystals arranged in nine rings with increasing forward segmentation [10]. These crystals are closely packed to cover the angular range 4.0°-172.0° as shown in figure 2.3 and figure 2.5. Crystals on rings are made of CsI with high thallium concentration (1200ppm). The thickness of each CsI varies from 3.66 mm (Ring #9) to 9.85 mm (Ring #1). To protect the crystals from light, their front surface are covered by a thin 0.9 mg/cm^2 Al foil. Since a lot of delta electrons are emitted in heavy ion collisions, the front of each crystals are also covered with high Z materials: Sn/Pb foils. The thickness of Sn/Pb foils vary from 73.5 mg/cm^2 for the most forward Ring #1 to 9.8 mg/cm^2 for the most backward ring #9.

At the Coupled-Cyclotron Facility (CCF), beams (even for stable beams such as 40Ca and 48Ca) are produced as secondary beams. Secondary beams from cyclotrons have large emittance resulting in large beam spot. For this experiment, typical beam spot size is 10 mm accompanied with a large beam halos. To protect the crystals in Ring #1 and Ring #9 from being hit by the beam particles especially those in the beam halo, we removed these rings in the experiment. Ring #6 at polar angle 90 ° is removed to accommodate the target structure. The targets are mounted on a target ladder as shown in figure **??**. The bottom of the target ladder is attached on a vertical stainless steel rod which is half inside the chamber and half outside the chamber. By pushing or pulling this stainless steel rod from outside the bottom of the chamber, the height of target ladder can be adjusted so that different targets can be aligned with beam. Removal of ten crystals, four from ring #3, three from ring #4 and three from ring #5 allows particles to be detected directly by HiRA10 as shown in Figure 2.6. Each HiRA10 telescope is represented by the red "squares" in the figures. To

Figure 2.5: The target ladder used in the experiment.

create the opening for HiRA10, new mounts in the shape of a "C" than full circles must be designed to hold the remaining crystals in each "ring". The designs of these rings are very complicated and expensive to machine. Instead, we 3D-printed using VeroWhite, a very dense polyjet 3D printing materials. The choice of the materials is very important as these 3D parts are placed in the chamber so they must not outgas into the vacuum. In addition, the quality of printing is also critical to prevent mciro-bubbles that may trap gas during the printing process. The 3D printing precision we used is better than 0.05 mm (600 DPI) which ensures the accuracy of the prototyping.

Unlike protons, the cross sections for neutron interacting with Microball crystals is estimated to be less than 5% based on the density and thickness of crystals. Thus, no crystals are removed on the opposite side of HiRA to allow neutrons to be detected by LANA unblocked by the Microball crystals. In any case, it would be very difficult to fabricate a strong structure consisting of only two arcs to support the top and bottom detectors.

2.2 HiRA10

HiRA10 is an updated version of HiRA (High Resolution Array) [77]. While the original HiRA with 4 cm CsI crystals is well suited for experiments with low energy charged-particles, it is not able to measure the energy of high energy charged-particles produced in our experiment. For high energy light charged-particles such as protons, deuterons and tritons, limited to the 4 cm length of CsI(Tl), they will punch through HiRA crystal and deposit only a small portion of their kinetic energies. With longer crystal length, HiRA10 can measure protons with kinetic energy up to 200 MeV, compared to 116 MeV for the original HiRA. The design of HiRA10 is based on modular strip Si-CsI telescopes which have been widely

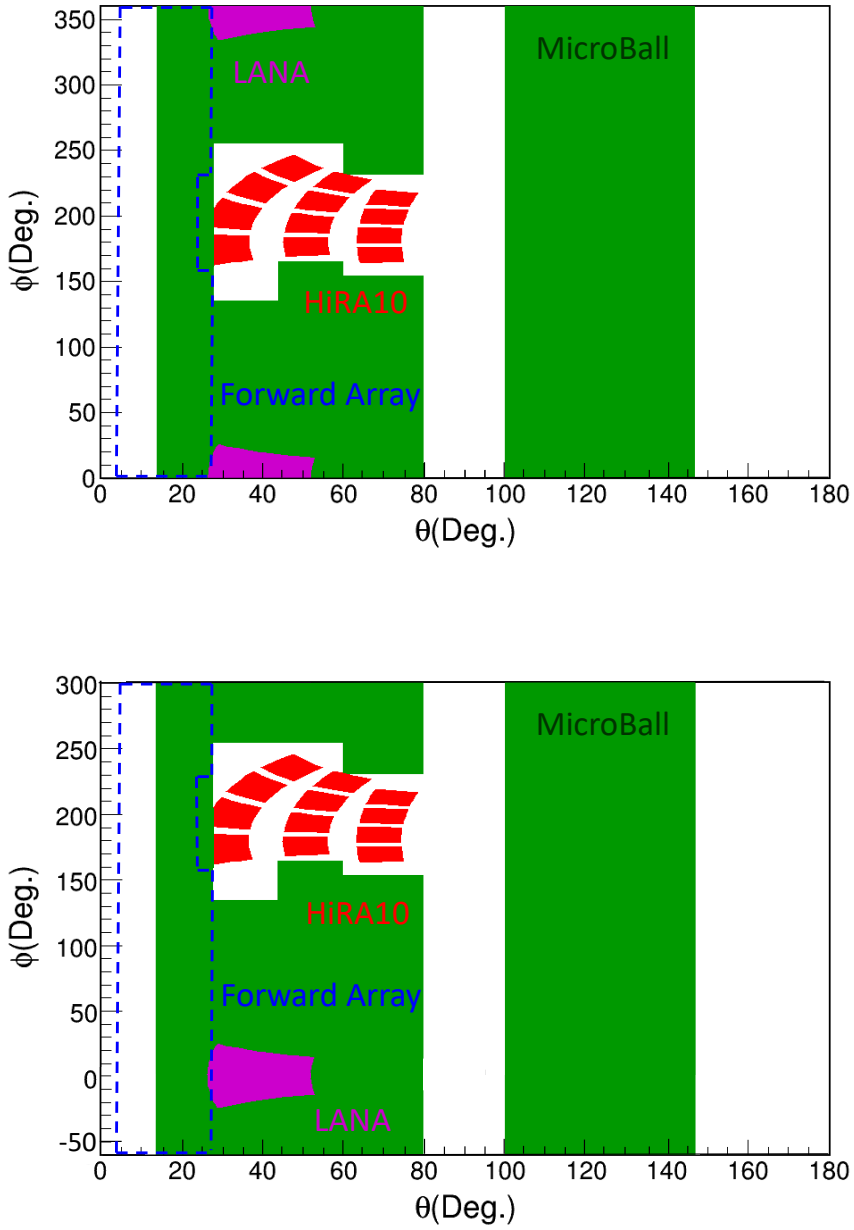

Figure 2.6: Angular coverage for Forward Array, Microball, HiRA10 and LANA in lab Φ-Θ coordinates. The dashed blue rectangle represents the coverage of the Forward Array, green regions represent Microball, red regions represent twelve HiRA10 telescopes arranged in 4 towers, and the purple region represents LANA coverage. Ten crystals in total are removed on Microball ring #3, #4 and #5 leaving a direct path for the fragments to be detected by HiRA10. There is no such accommodation for LANA. Microball ring #6 is removed for target structure. The Microball covers part of the forward array from $\Theta = 13^{\circ}$ to $\Theta = 28^{\circ}$. In the adopted co-ordinate from 0 and 360 deg, the coverage of LANA is split at 0 and 360 degree (top panel). The bottom panel shows LANA in continuous angular coverage by plotting the ϕ range from -60° to 300°.

adopted by the physics community in the past two decades to detect charged particles in nuclear structure and nuclear reaction experiments. The Si-CsI telescopes utilize the energy loss technique [12, 77] includes LASSA [78], MUST2 [79] and FARCOS [80].

The upgrade design and testing of HiRA10 was mainly done by Sean Sweany, who will describe HiRA10 in details in his thesis. In this thesis, only a brief description of HiRA10 is given to allow a self-contained description of the experiments. HiRA10 consists of twelve identical telescopes grouped into three towers with four telescopes in each tower as shown in figure 2.8. Each HiRA10 telescope is composed of a 1.5 mm double sided Si strip detector (DSSSD) backed by four 10 cm CsI scintillator crystals as shown in figure 2.7. The increase from 4 cm to 10 cm CsI crystals to allow detection of protons up to 200 MeV is the main upgrade designed specifically for this experiments. Both the front and back side of each DSSSD have 32 strips. Every strip is 1.95 mm wide and the strips on the front and back are perpendicular to each other, allowing for high resolution position measurements of events. Given the width of every strip, the angular resolution for HiRA10 at 35 cm is 0.32°. Taking the uncertainties from beam spot into account, the angular resolution is better than 0.5° [12]. For a particle that is fully stopped in the CsI crystal, the correlation between the energy deposited in DSSSD and the residual energy deposited in corresponding crystal can be used to identify the mass and charge of this detected particle. This particle identification method is called energy loss technique. Figure 2.9 is an example showing the result of energy loss technique, which is produced by 16 strips, front and back, in one quadrant of one HiRA10 telescope and their corresponding CsI crystal. The energy calibration for DSSSD was carefully done with ^{232}U α source which has 4 peaks with energies spanning from 5.41 MeV to 8.58 MeV. The energy calibration for CsI crystal is based on proton-recoil scattering data with punch-throughs of p,d,t and low energy elastic scattering of protons on ^{40,48}Ca targets

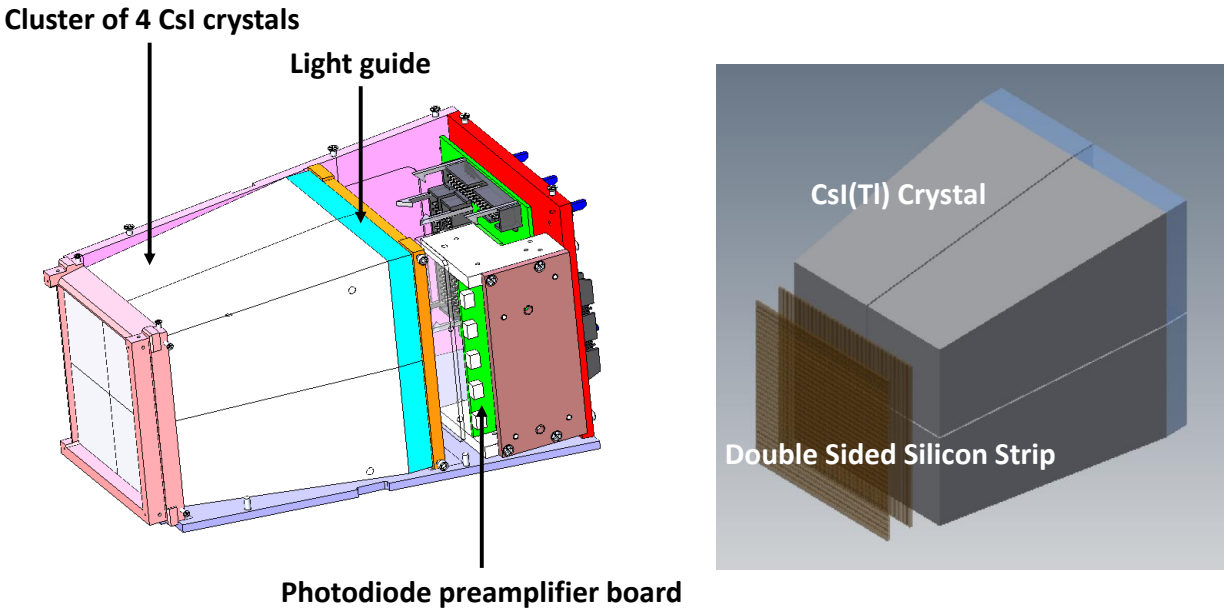

Figure 2.7: (Left panel) A mechanical drawing of a HiRA10 telescope with its aluminum container and associated electronics. The DSSSD (not shown) is placed in front of CsI crystals. (Right panel) A schematic drawing of a HiRA10 telescope showing the front and back sides of the DSSSD placed in front of the 4 CsI crystals.

at incident energies of 28 MeV/u, 56.6 MeV/u, 39 MeV/u and CH_2 target at incident energy of 139.8 MeV/u. The relevant details can be found in Ref. [12].

2.3 The Large Area Neutron Array (LANA)

Despite recent advance in new scintillation materials, liquid scintillator is still the most cost effective way to build large area neutron detectors. The Large Area Neutron Array (LANA) is composed of two large neutron walls. Each wall consists of 25 independent neutron detection bars that cover a total area of 2×2 m^2. The scintillator bars are horizontally stacked as schematically shown in Figure 2.10. Taking into account the thickness of the Pyrex glass (3 mm) and a gap of 3 mm between bars, the total active geometrical area of the 2×2 m^2 wall is reduced by about 12% [13]. To maximize detection efficiency, the LANA features small dead space between scintillators and minimum inactive mass through which the neutrons must pass [13].

Each detector cell is a 2m-long Pyrex glass container, with a rectangular cross section of NE-213 with height $h = 7.62$ cm on the vertical direction and depth $w = 6.35$ cm as indicated in the upper corner of Figure 2.10. Both ends of each Pyrex bar are coupled with 7.5 cm diameter Philips Photonics XP4312B/04 photomultipliers (PMTs), to detect the scintillating light produced in the bar by an incident radiation. Typical high voltage employed on PMTs is 2200 volt. Each cell is filled with liquid organic scintillator NE-213 [81]. NE-213 was chosen for its excellent efficiency for detecting fast neutrons and its pulse shape discrimination (PSD) properties that enable the discrimination between neutrons and gamma-rays [82, 16]. Liquid scintillator that has PSD characteristic is especially desirable for heavy-ion collision experiments where copious photons and neutrons are produced and must be identified in

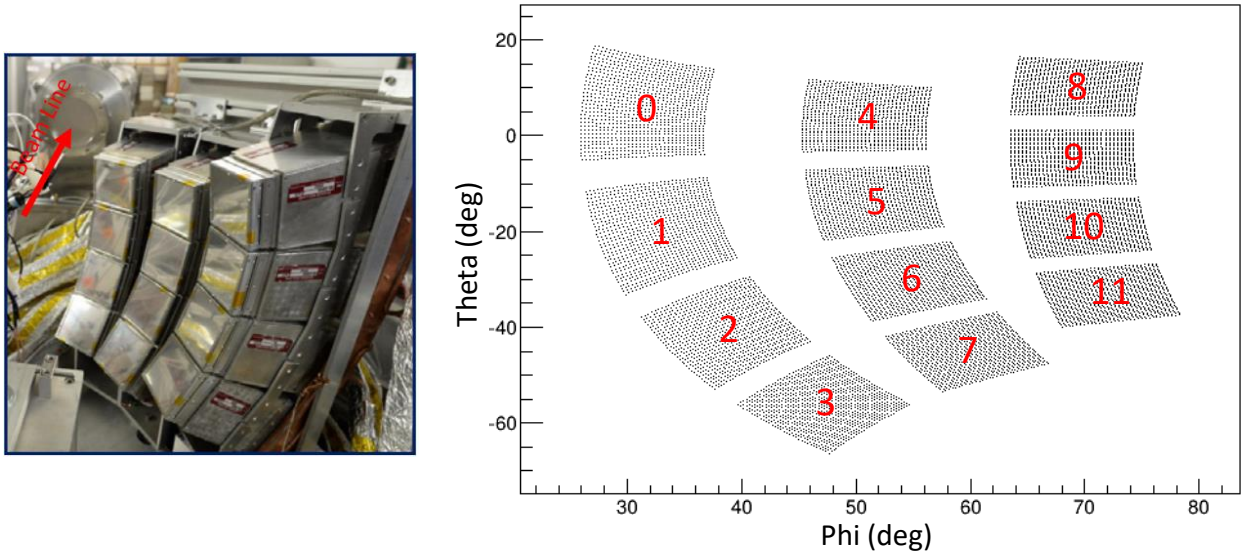

Figure 2.8: (Left panel) 12 HiRA10 telescopes arranged in 3 towers used in the present experiments. The mounts are designed in approximately in an arc so that the center of each telescope is located at 35 cm from the target. (Right panel) Angular coverage of 12 telescopes in HiRA10 on a (θ, ϕ) plane measured by Romer arm technology [11]. Each point represents a DSSSD (1.95mm $\times$ 1.95mm) pixel.

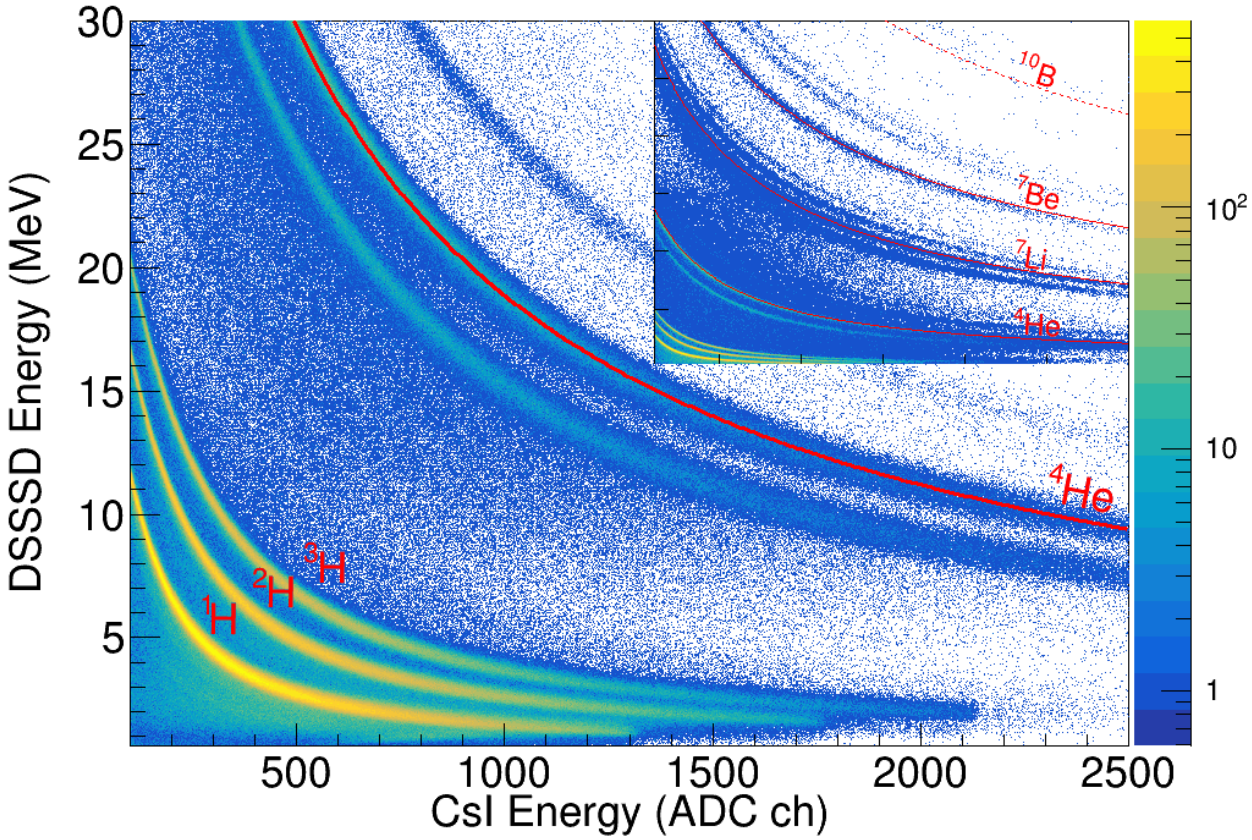

Figure 2.9: Particle identification of a HiRA10 telescope. The Y axis is the calibrated DSSSD energy loss (ΔE) versus the ADC channels of the residual energy (E) in the CsI 2D plot. The top right inset shows an extended plot up to 120 MeV of energy loss in DSSSD. Red lines are PID lines from simulation for various isotopes. This figure is adopted from Ref. [12].

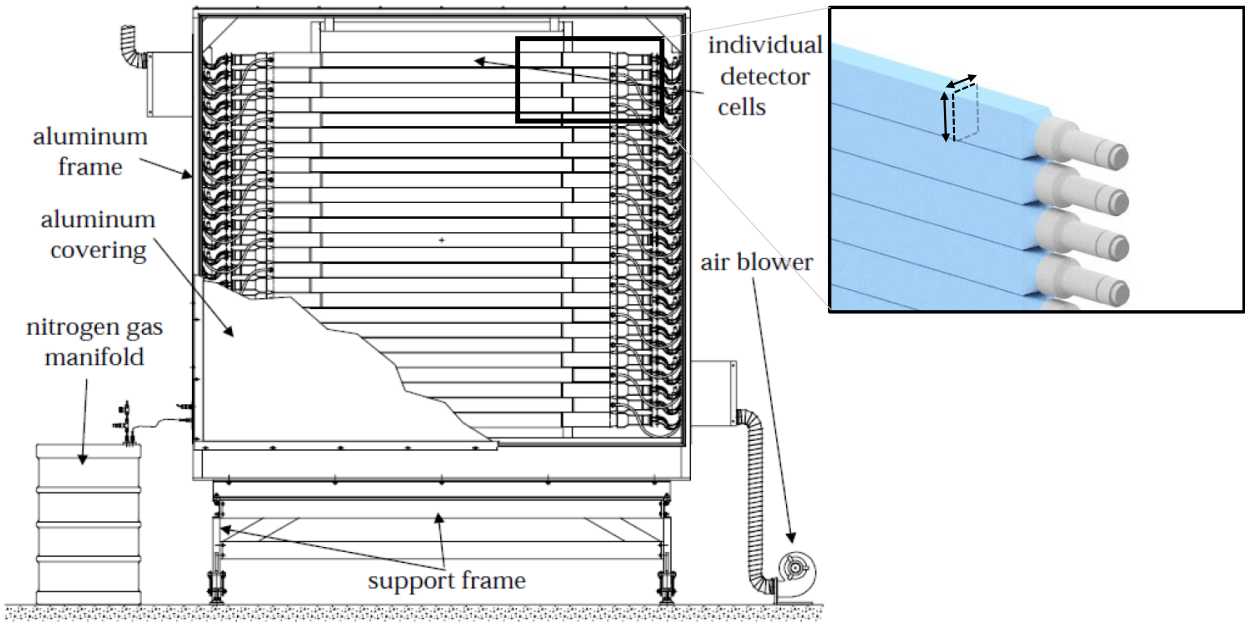

Figure 2.10: Mechanical cutaway drawing of one wall of the Large Area Neutron Array. [13]

data analysis. The LANA is designed to detect neutron from about a couple MeVs to about 300 MeV when it is placed at 4.5 meters from the target.

The physical location of each bar is determined by laser measurements made on the surface of the wall with respect to a global reference frame in the Facility for Rare Isotope Beams (FRIB) Laboratory [14]. Such measurements allow one to determine not only the absolute position of each bar with respect to the target during an experiment, but also the relative positions between bars of each wall, which is relevant for the time calibrations described below. The distance from the target to the front LANA (NWB) and back LANA(NWA) is 441.6 cm and 517.5 cm, respectively. Two walls are placed at 39.37° with respect to beam direction. Please note that the most bottom bars of two walls are not used due to shadowing and lack of electronics channels so only 24 bars are used in each wall. Figure 2.13 show their angular coverage.

The LANA was constructed in 1997. The frames were designed to allow nesting of the two walls so that one wall is located in front of the other. This configuration increases the efficiency of neutron detection at the expense of covering a wide angular range. The NE-213 liquid scintillator is flammable and hazardous. Furthermore, with the size and weight of the two walls in addition to the large number of cables which have to be first disconnected from the electronics, moving and nesting the two walls required a lot of advanced planning and safety precautions. Figure 2.11 shows the inner structure and liquid scintillator bars of one LANA wall after the front aluminum cover is removed under ultra-violet light. For clarity, after nesting, the front wall is labelled as NWB while the back wall is labelled as NWA. LANA refers to both walls in this thesis.

To study particles emitted in the overlapped compressed zone in central collisions, the LANA should be placed at polar angle around 90° in the center of mass frame in order

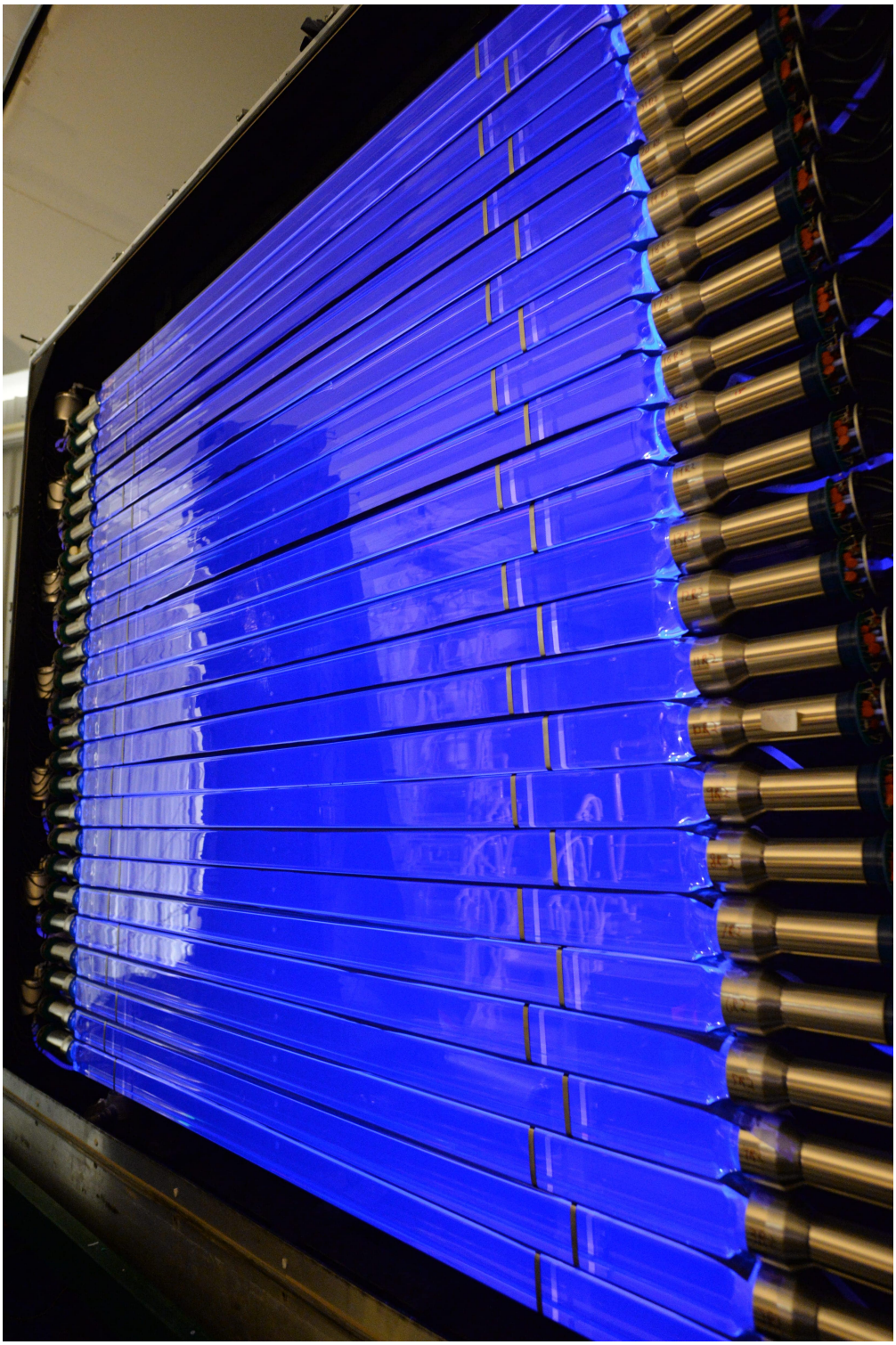

Figure 2.11: One of LANA walls is illuminated with ultra-violet light after the front aluminum cover is removed.

to minimize contributions from projectile-like and target-like fragments. For symmetric projectile and target systems, this corresponds to around 45° in lab frame. Unfortunately, we are limited by the walls in the vault as shown in Fig. 2.12. LANA was eventually placed at 39.37° with respect to beam in lab frame (the accurate measured angles come from the laser measurements).

In order to implement the detector capabilities described above, we used the electronics setup schematically shown in Figure 2.14 for one PMT. An analogous electronics chain is replicated for each of the 100 PMTs in the two neutron walls. Each PMT has an embedded passive voltage divider circuit as described in Ref. [13]. Such a circuit, omitted in the drawing of Figure 2.14 for the sake of clarity, allows one to use both the anode and the last dynode signals, labelled respectively as "anode" and "dynode" in the figure. The anode signal is a negative-voltage pulse that contains the charge from the multiplier chain and is used to produce the integrated charge signals. To enable the PSD analysis, the anode signal is initially split into two equal signals by means of an NSCL passive splitter module. One split signal, named "total" in Figure 2.14, is sent to a channel of a common gate CAEN V792 charge-to-digital converter (QDC) [83] for the integration of the total charge. The other split signal is integrated for its fast component ($\approx$ 30 ns). To successfully implement the detection of more than a single particle in an event, which is required for high-multiplicity heavy-ion collision experiments, the gate for the fast component integration is generated independently for each hit within an event. The gate is generated from the dynode signals by using a Lecroy 1806 16-channel constant-fraction discriminator (CFD) [84] and a CAEN C469 16-channel gate and delay generator [83]. These gates are used to digitize the fast component of the anode signals using a CAEN V862 individual gated QDC [83]. This allows the PSD technique to be applied exclusively to single-particle events. The logic chain, which

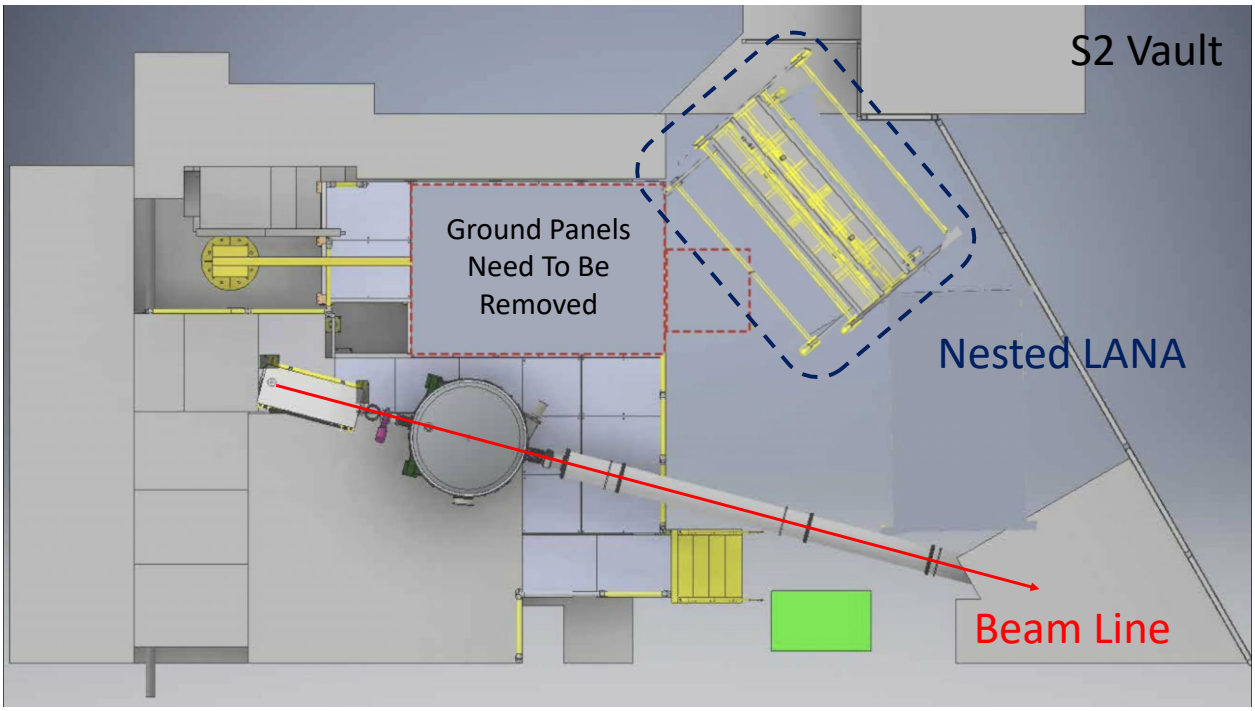

Figure 2.12: 3D mechanical overview drawing showing the position of LANA being limited by the vault wall. During the move, some floor panels had to be removed. These panels were installed back again after the moving of LANA was done.

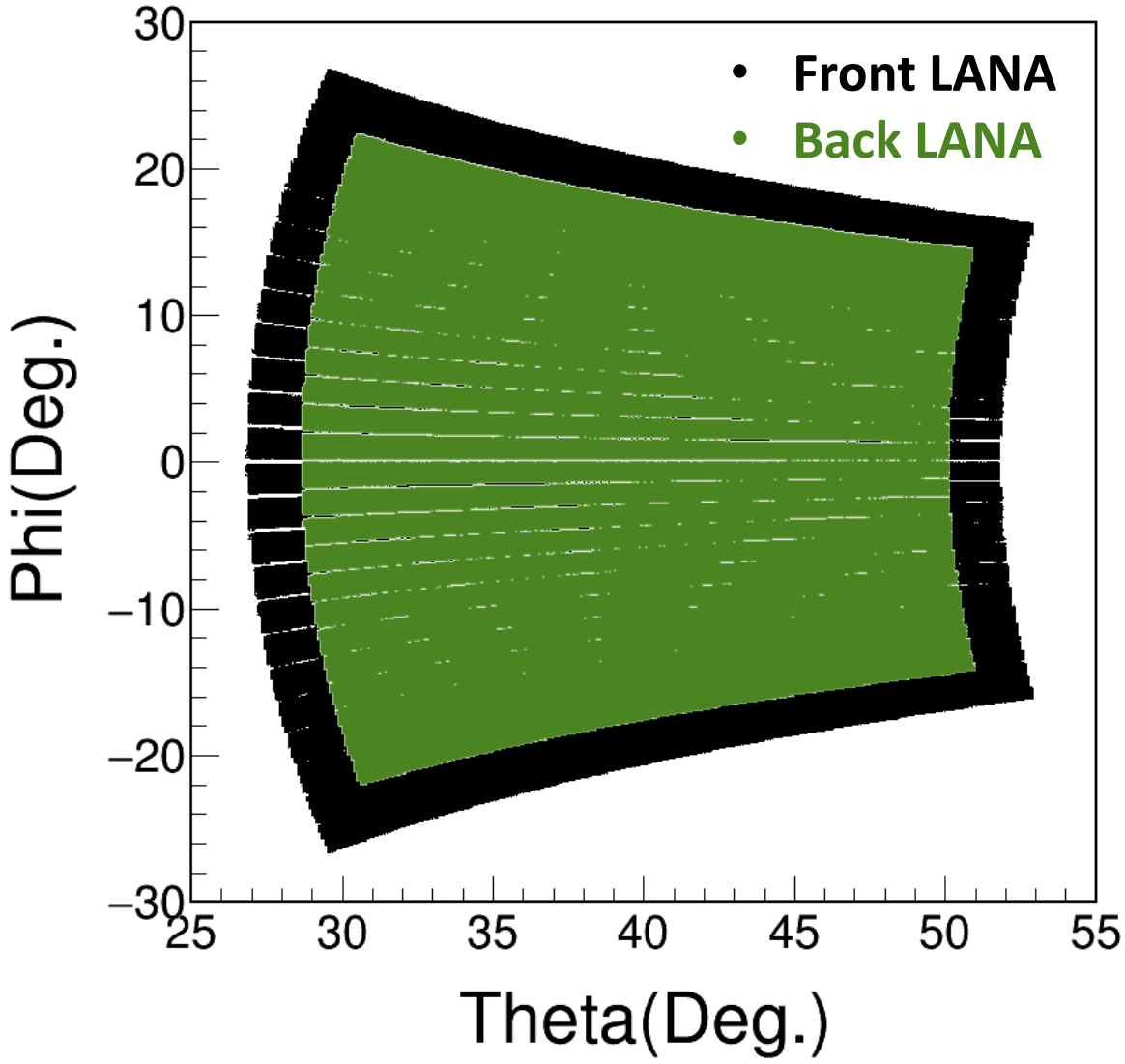

Figure 2.13: Angular coverage of the front LANA (NWB) and back LANA (NWA) in the lab frame based on laser position measurement.

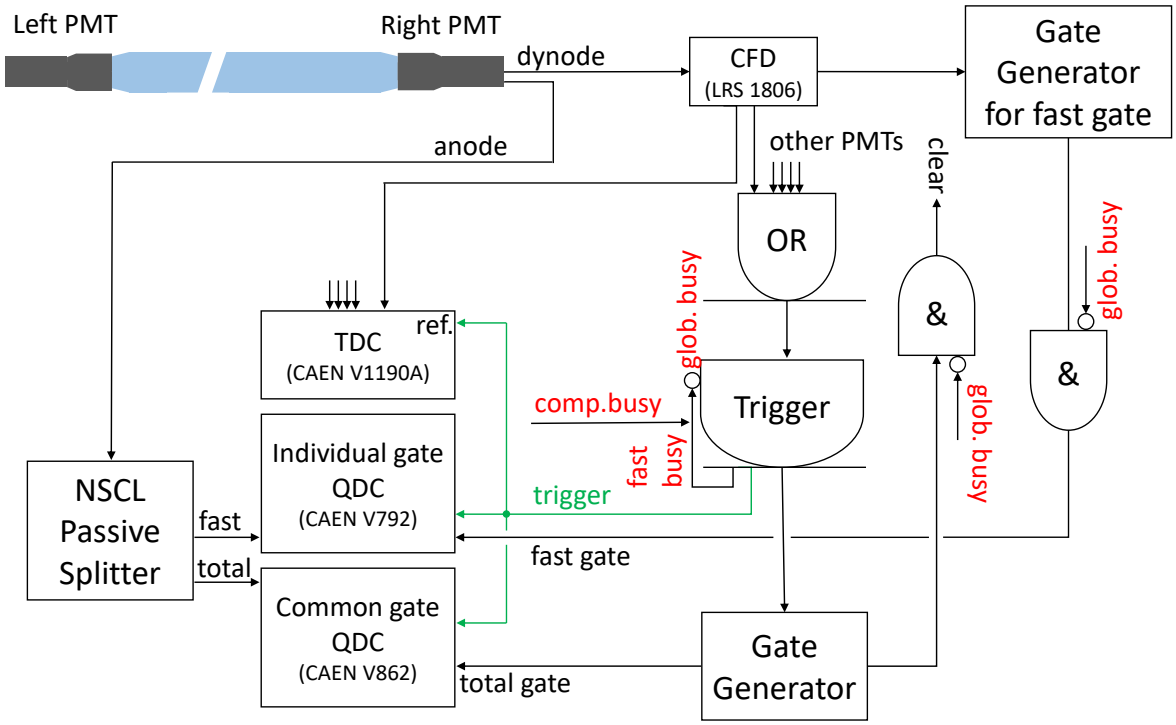

Figure 2.14: Schematic of the electronics setup (for one PMT) used to process signals from the LANA when the walls are used in standalone mode. An exact reproduction of these circuits is used to process signals obtained with each of the 100 individual PMTs. "Fast" and "total" are two copies of the original anode signal but integrated respectively by using a fast gate (containing only the fast component of the signal) and total gate (containing the whole signal) for PSD analysis. PMT dynode signals are used for the timing.

includes trigger, gates, and timing, is implemented by using the dynode signal from the PMT voltage divider fed into the CFDs. The trigger to the acquisition system is produced by a logical "OR" of all the CFD signals for each PMT in the walls in anti-coincidence with a global busy signal, generated as the "OR" of the computer busy and a fast busy signal, obtained by stretching a copy of the trigger itself. The latter prevents multiple triggers at a time interval shorter than the time required by the circuit to generate the gates and to process the event. The trigger signal is used to produce the total gate for the commonly gated QDCs, which is a logic signal of about 3 μs in length, as well as the time reference and trigger signals for the CAEN V1190A time-to-digital converter (TDC) [83]. This TDC records the time difference between the individual dynode CFD signal and this reference signal, which are used for the position and time calibrations of the wall. Finally the trigger is sent to the data acquisition to enable the readout of each module. In the latest experiment using LANA, digital electronics was set up in parallel to the analog electronics for 8 bars. Analysis using digitized waveforms to devise software algorithm to improve neutron/gamma pulse shape discrimination (PSD) is discussed in Ref. [16].

2.4 Forward Array

Time of Flight (ToF) technique is a method for measuring the energy of particles based on the time they travel between a start-time and a stop-time detectors. Given the distance between start-time and stop-time detectors known as D and the time of flight measured as Δt, the speed v of a particle can be calculated by $v = \frac{D}{\Delta t}$. The Forward Array is used as the start-time detector for the neutron ToF measurement while the LANA is the stop-time detector.

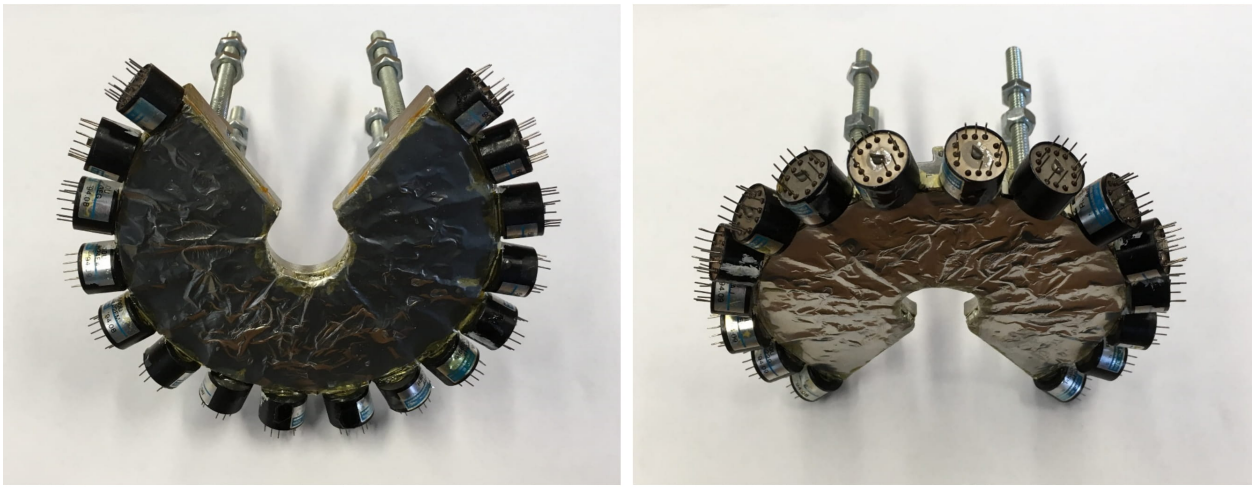

Figure 2.15: The front and back views of the original Forward Array without PMT bases. The front side of Forward Array is covered by a thin layer of Sn/Pb foil to protect itself from δ electrons emitted in reactions.

The Forward Array was originally constructed for experiment in Ref. [85]. It was upgraded to increase its forward angle coverage. The original forward array is composed of 16 wedges of NE-110 plastic scintillator, all of which are placed on a partial annulus whose inner diameter is 1 inch and outer diameter is 4.5 inches. The annulus has a 72° cutout to allow charged particles to be detected by the Large Area Silicon Strip Array (LASSA) which is a prototype of HiRA) in Ref. [9]. Each scintillator wedge is first painted with Bicron BC-620 reflective paint to enhance light internal reflection before it is detected by the PMTs. The wedge is then wrapped in aluminized mylar foil to prevent cross talks between adjacent detectors. Hamamatsu R5600U PMT is attached on the back of each scintillator wedge as shown in Figure 2.15 and an E5780 base is coupled with each PMT during experiments.

In our experiments, we are able to eliminate the 72° cutout angles by adding two more wider but shorter scintillator wedges. Each new wedge covers angular range of 36° with the outer radius of new wedges to 3 inches. The shorter scintillator wedges as indicated by the indentation of the blue dashed rectangle representing the FA in Fig. 2.6 ensure that HiRA10 is not shadowed. The original 16 PMTs are not suitable for PMTs of new wedges. If similar PMTs are installed at the side surface of new wedges, their shadowing can go up to around 45° in polar angle which will surely shadow HiRA10. The two PMTs for the new shorter scintillator wedges were attached perpendicular to the wedge plane at the back. The photos in Fig. 2.16 show the two holes for the PMT's.

A new mount supports the Forward Array in place. It also provides the platform where two additional scintillator wedges are attached. To accomplish this, we 3D-printed the support using Connex350 3D-printing facility at MSU electrical and computer engineering department [86]. Figures 2.16 show how the original Forward Array is assembled with new components. We used the VeroWhite materials for its excellent properties in vacuum.

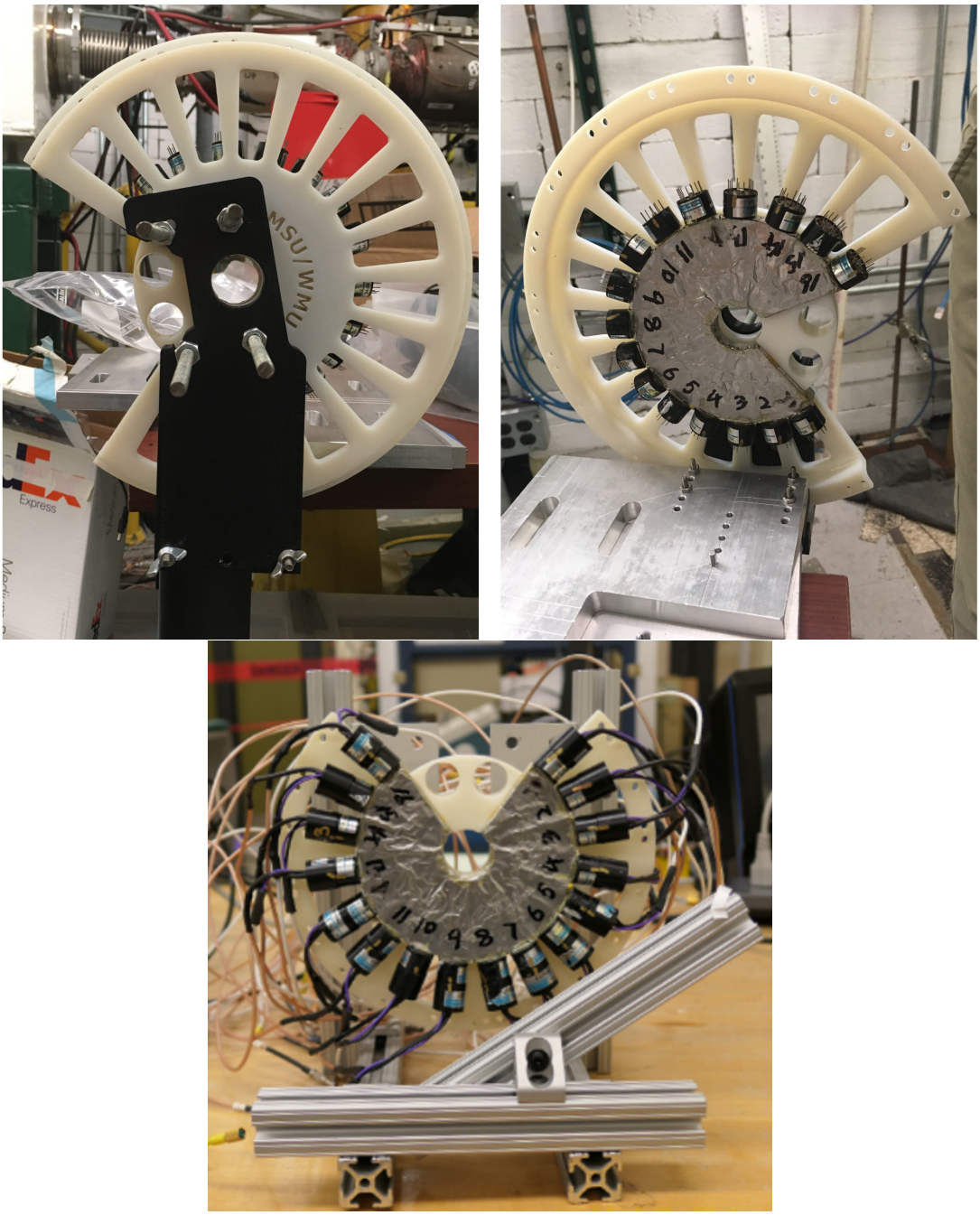

Figure 2.16: The front and back views of the original Forward Array assembled with its backing.

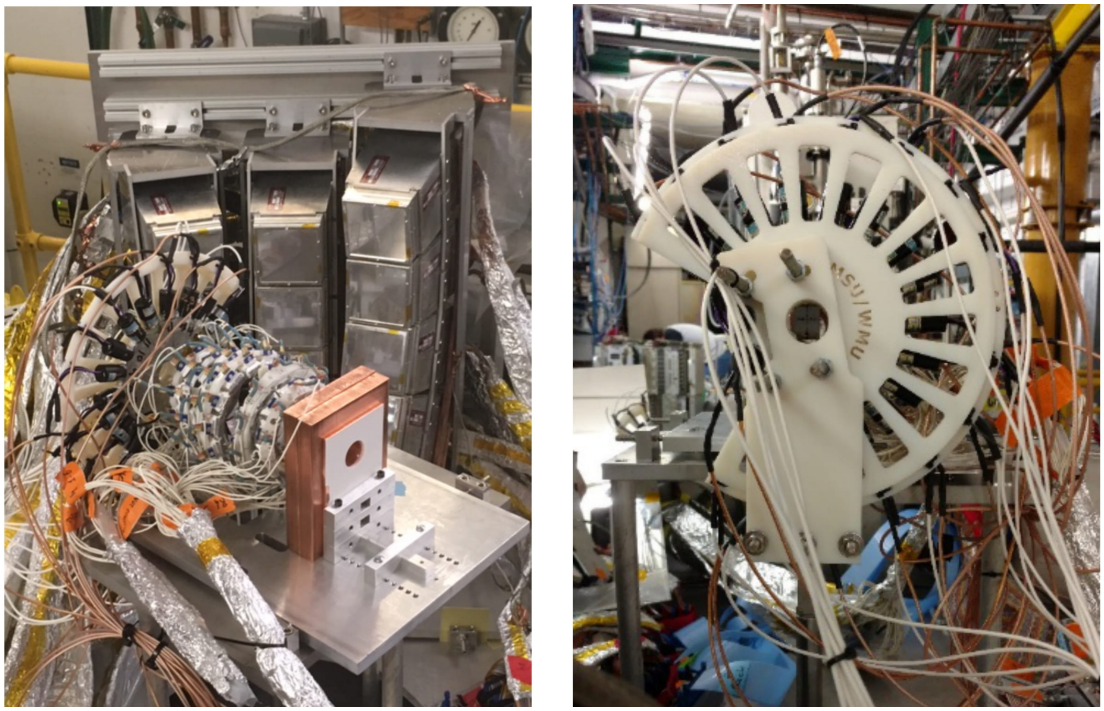

Figure 2.17: The side and back views of the upgrade Forward Array placed in position during experiments.

The upgraded Forward Array is placed about 12 cm from the target downstream with the beam axis passing through the center hole as showed in Figure 2.17. To measure the neutron ToF, we use the Forward Array triggering time as the start time and the LANA triggering time as the stop time. The Forward Array is triggered mainly by the abundant charged particles emitted in the forward angles. Being placed only 12 cm from the target while LANA is placed 4.5 m away, the differences in the time arrivals of the particles to the forward array is negligible. Details about neutron ToF analysis will be discussed in Section 3.2.2.

2.5 Charged-Particle Veto Wall

In general, neutrons are difficult to measure. When neutron interacts with the protons in the scintillator, the recoil proton is usually detected. Similarly, if a proton (or charged particles) is detected by a neutron detector, it cannot distinguish proton from neutrons. Although NE-213 attains excellent discrimination of γ rays and neutrons utilizing Pulse Shape Discrimination (PSD) technique, it cannot by itself discriminate charged particles produced in the target from these recoil protons that are produced by the neutrons we want to measure.

To ensure near 100% rejection of charged particles from the target, we designed and built a large Charged-Particle Veto wall (VW). The project is a collaboration between the HiRA group and Professor Zbigniew Chajecki at Western Michigan University (WMU). Professor Zbigniew Chajecki is also the spokesperson for one of the experiments.

2.5.1 Design and Prototype

The Charged-Particle Veto Wall consists of 25 vertically-placed 1 cm thick plastic scintillator bars in front of the LANA. Only 20 bars are needed to cover LANA. Nonetheless, 5 extra bars are mounted to provide spares in the event that one of the bars failed in the middle of the experiment so that the failed bars can be replaced quickly. We choose 1-cm-thickness of plastic scintillator to ensure sufficient strength of the bar which is 2.5m long while minimizing interaction of neutrons with the veto bars. The density of EJ-200 (1.02 g/cm^2) is about 17% higher than the density of NE-213 (0.874 g/cm^2) but NE-213 used in LANA is 5.65 times thicker. The loss of about 20% neutrons in the veto wall will need to be corrected in determining the neutron cross-sections. With the current design, we are assured that a signal from a charged particle hitting LANA will be detected 100% while less than 2% of the neutrons will be detected assuming the neutron detection efficiency is 10%.

To ensure that 100% charged-particle will be vetoed, firstly, these scintillator bars are required to fully cover the LANA with no gap when looking from the target. Secondly, because the scintillator bars are placed vertically, the horizontal hit position resolution i.e. the width of the veto bar should be similar to the resolution of the neutron bar which is about 8 cm. 3 mm overlap is designed to ensure that there are no gaps between neighboring veto bars taking into account possible inaccuracy in the veto wall installation. Thirdly, the Charged-Particle Veto Wall should be placed as close as possible in front of the LANA to better correlate the hits in Veto Wall and the LANA. The bars are made of EJ-200 [87] scintillator material coupled with PHOTONIS XP3462 PMTs. The PMTs were harvested from the MSU 4π array [88]. The outer diameter of each PMT's shielding tube is 8.74 cm which impose the main limitations on the width of the veto bars.

The final design consists of the scintillator bars with dimension of 9.4 cm wide x 250 cm tall and 1 cm thick. The ends of each bar are tapered to 5.65 cm in order to couple with a 7.62 diameter light guides which are first glued onto the PMT's as shown in Fig. 2.18. Precision grooves are machined on the side of the light guides coupled to the veto bars. The tapering at veto bar ends is necessary in order to insert and secure the veto bars into the grooves in light guides as shown in Fig. 2.20. SYLGARD^{TM} 182 Silicon Elastomer [89] is used as the gluing material between veto bars and light guides. As shown in right bottom panel of figure 2.18, the extra spaces at two ends of grooves on light guide allow extra silicone between the bar and the light guide contact to be squeezed out. Skill is needed to ensure no tiny air bubbles exist between in the silicon at the junction of the veto bar and the light guide contact. Scintillator bars are staggered back and forth to ensure 3 mm overlap between neighboring bars.

To test the design and to develop the complicated procedure in coupling the veto bar to the PMTs, we first built a prototype 30 cm veto bar. The prototype is identical to a full-sized bar including bar width, light guides and PMTs. Figure 2.19 shows the testing of the Veto Wall bar prototype in Chajecki lab at Western Michigan University. Similarly, 3D printed parts are used extensively in the design and testing of most of the parts in the construction of the Veto Wall.

2.5.2 Construction

After the prototype veto bar was tested successfully. Two full size bars were ordered from Eljen and tested at Western Michigan University before 24 more were ordered. At the end, 25 veto bars were selected to be used in our experiment. Each bar was constructed and tested at WMU. Finally, all 25 veto bars are assembled into a veto wall as designed. Before the VW

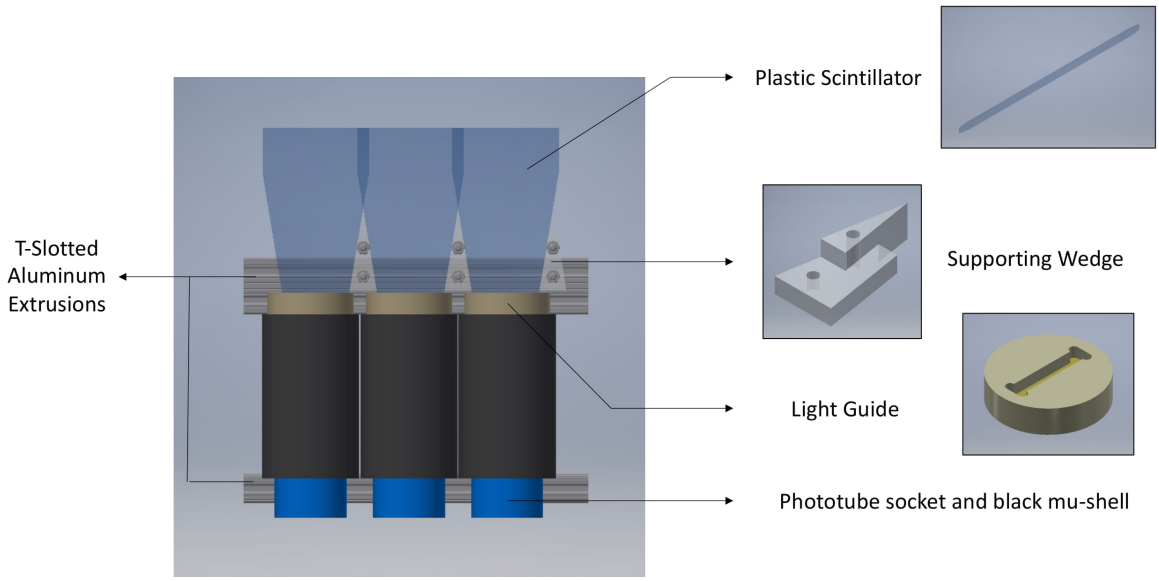

Figure 2.18: 3D sketch showing how 3 Charged-Particle Veto Wall scintillator bars are assembled at the bottom end with T-Slotted aluminum frame.

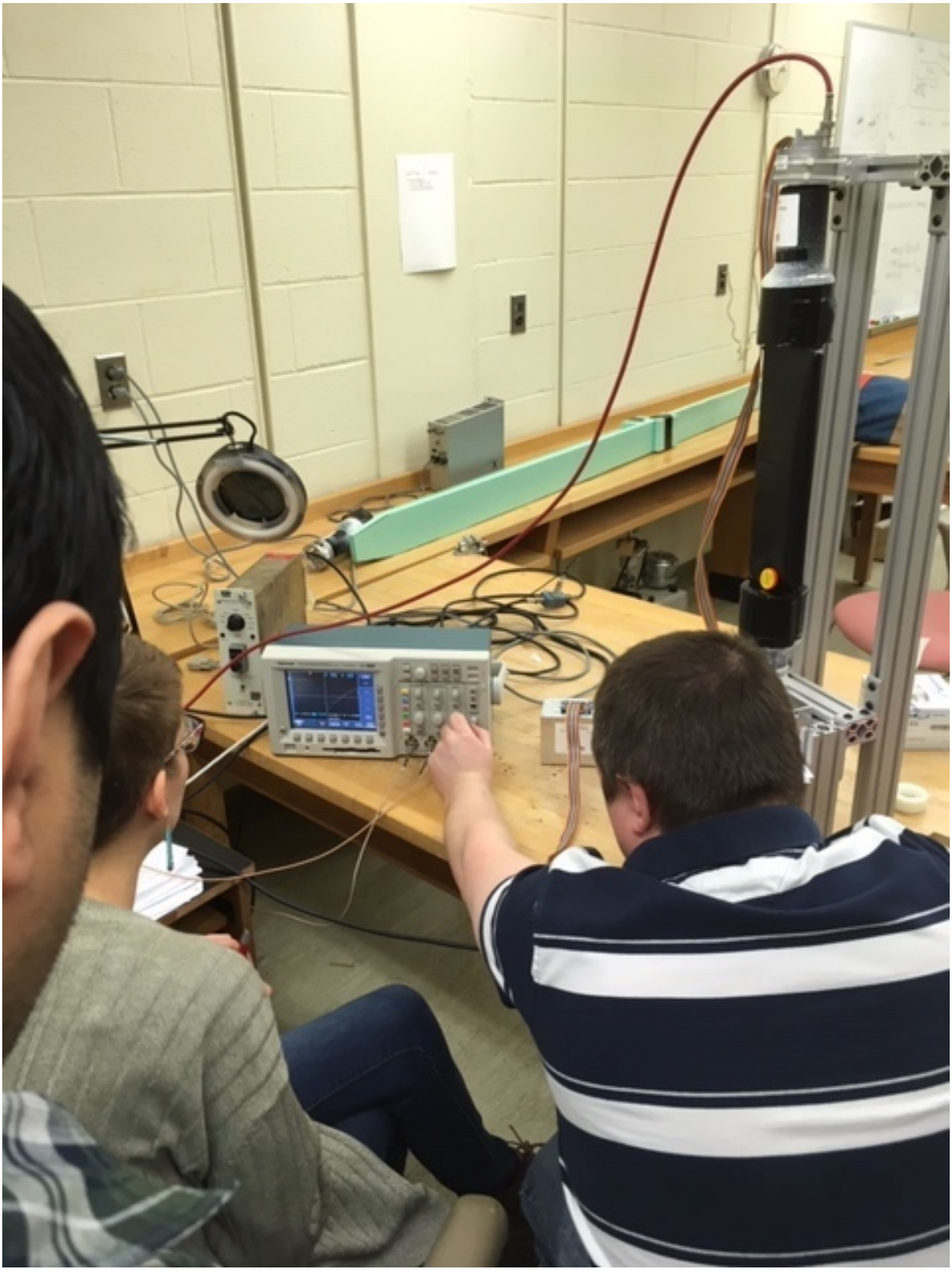

Figure 2.19: Professor Chajecki is studying the signal characteristic of Charged-Particle Veto Wall bar prototype (at the right of the figure) with his students at Western Michigan University.

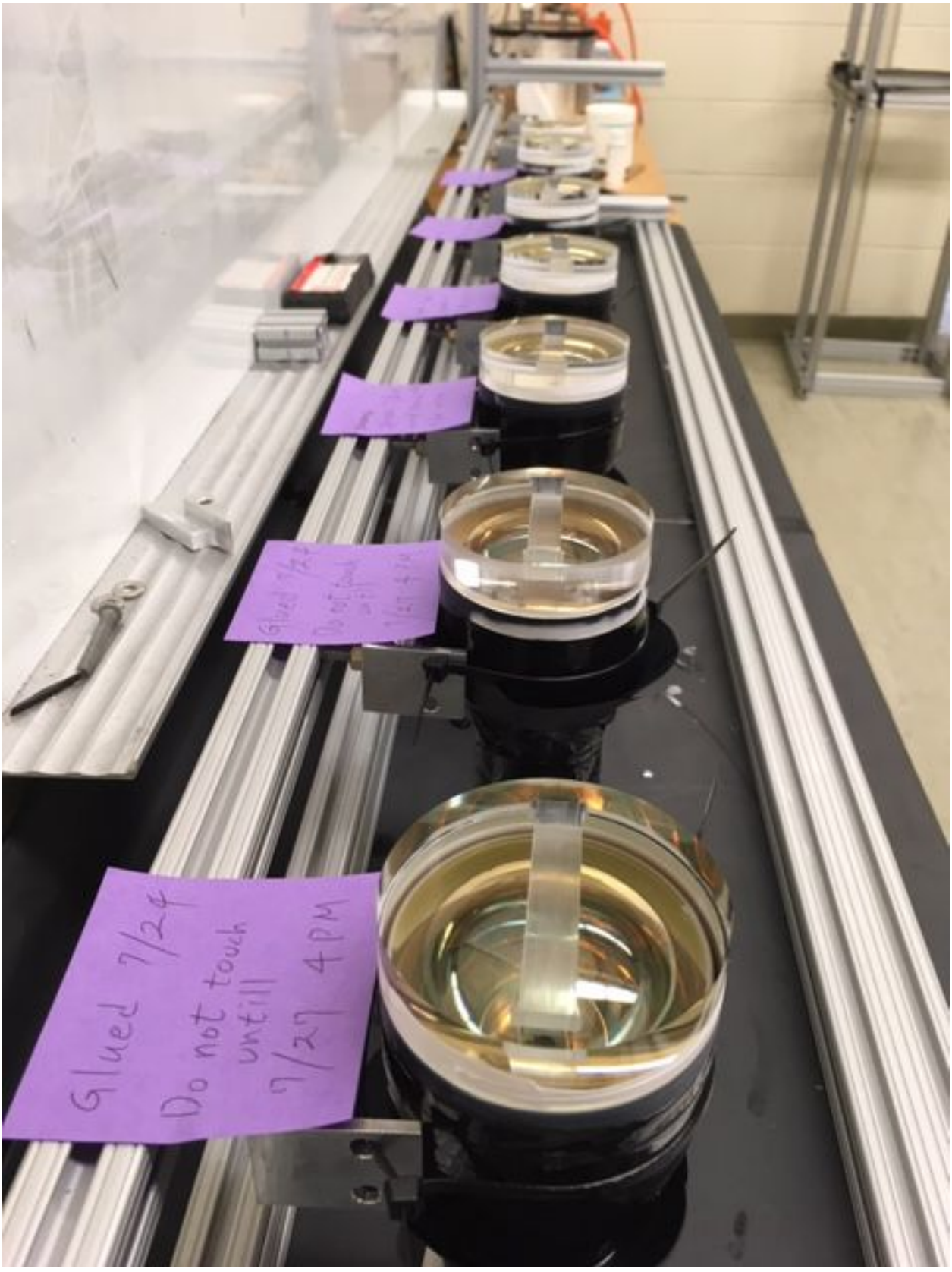

Figure 2.20: Light guides are being glued on PMTs at Western Michigan Universty.

Figure 2.21: (top left panel) Professor Chajecki is testing the Charged-Particle Veto Wall frame. (top right panel) Undergraduate students from Western Michigan University and Michigan State University are moving Veto Wall bar. (bottom left panel) Veto Wall bars are being taken out from shipment packages. (bottom middle and right panel) NSCL and WMU researchers are installing the Charged-Particle Veto Wall in front of LANA.

Figure 2.22: Charged-particle Veto Wall construction in progress. 22 bars have been installed in place.

commissioning experiment at NSCL in December of 2017. The wall was disassembled and reassembled in the S2 vault and coupled to LANA. The veto bars were packaged into wooden transportation boxes padded by foam. Special liquid foam packages that can conform to the shape of the cargo, were used to protect the fragile end of veto wall bars where PMTs are attached. Due to its length (2.5 m) and thinness (1 cm), customized aluminum structure was designed for support in taking veto bars on and off veto wall frame safely as shown in the upper two panels of Figure 2.21. The special aluminum structure prevents the veto bar from bending or even breaking during short distance transportation from veto wall frame to storage container and vice versa. Figure 2.22 and 2.23 show the scene while the Charged-Particle Veto Wall was being built.

The veto wall is placed at 393.3 cm away from the target. The distance between the VW and NWB and NWA was 48.3 cm and 124.2 cm respectively. Figure 2.24 shows how the Charged-Particle Veto Wall was nested with NWA and NWB. Figure 2.25 is a top view of experimental setup schematic. The beam direction is labelled. The dashed circle on the left upper corner represents the aluminum vacuum chamber used in experiments. The sizes and relative relationships between VW, LANA and target are drawn in scale. VW, NWB and NWA are parallel (< 1 °) with each other. The gold line pointing to VW is perpendicular to VW front surface in figure 2.25. This line is 39.37 ° with respect to the beam line. VW bars are labelled from from right to left as 0 to 24 as shown in Figure 2.25. Using this numbering, VW bar #12 is the middle bar. LANA is fully protected by VW bar #3 to #22.

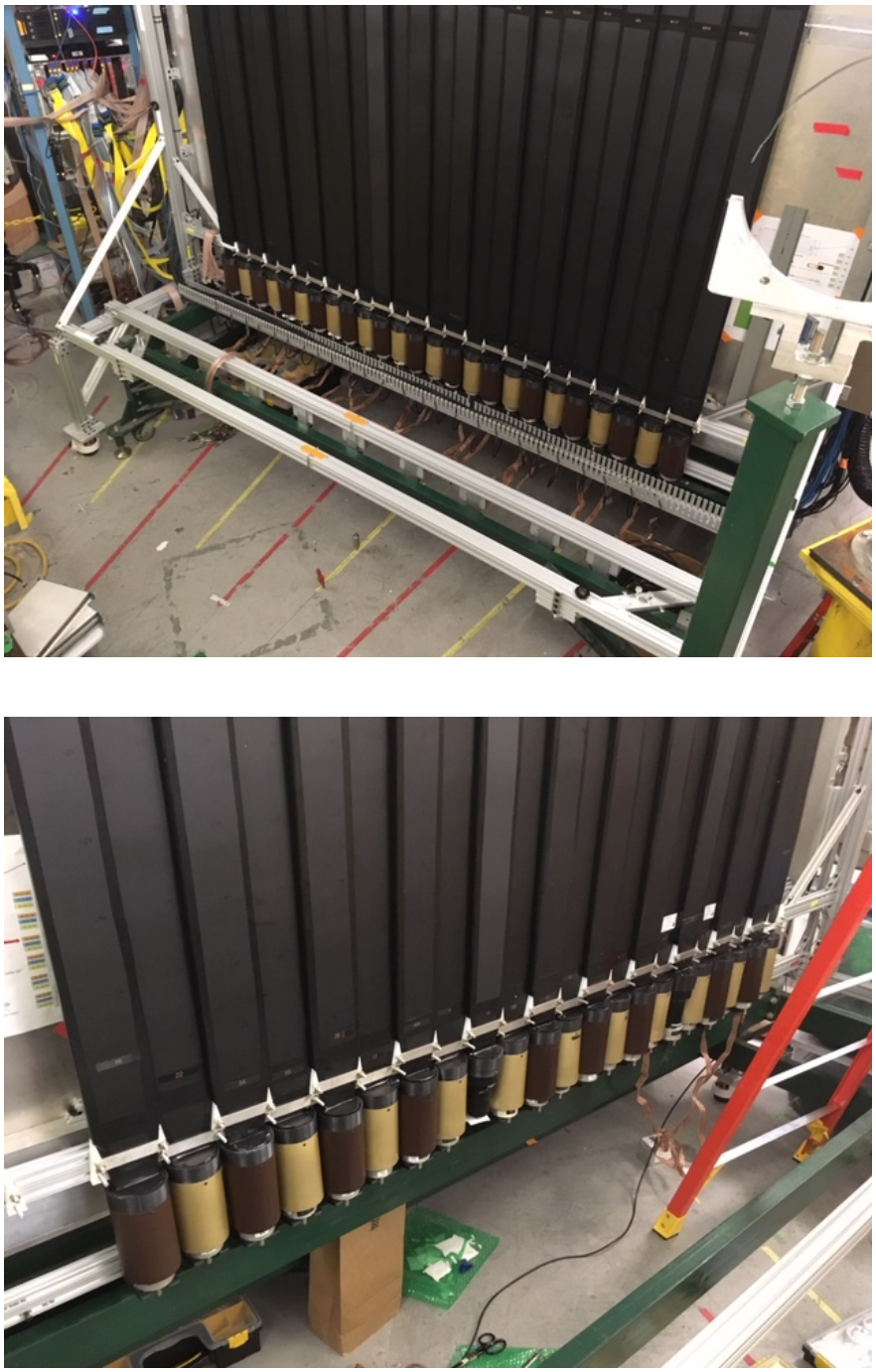

Figure 2.23: The Charged-Particle Veto Wall installed in front of the LANA. In the top panel, the red and yellow tape marks on the ground indicate the polar angle with respect to the beam direction in lab frame.

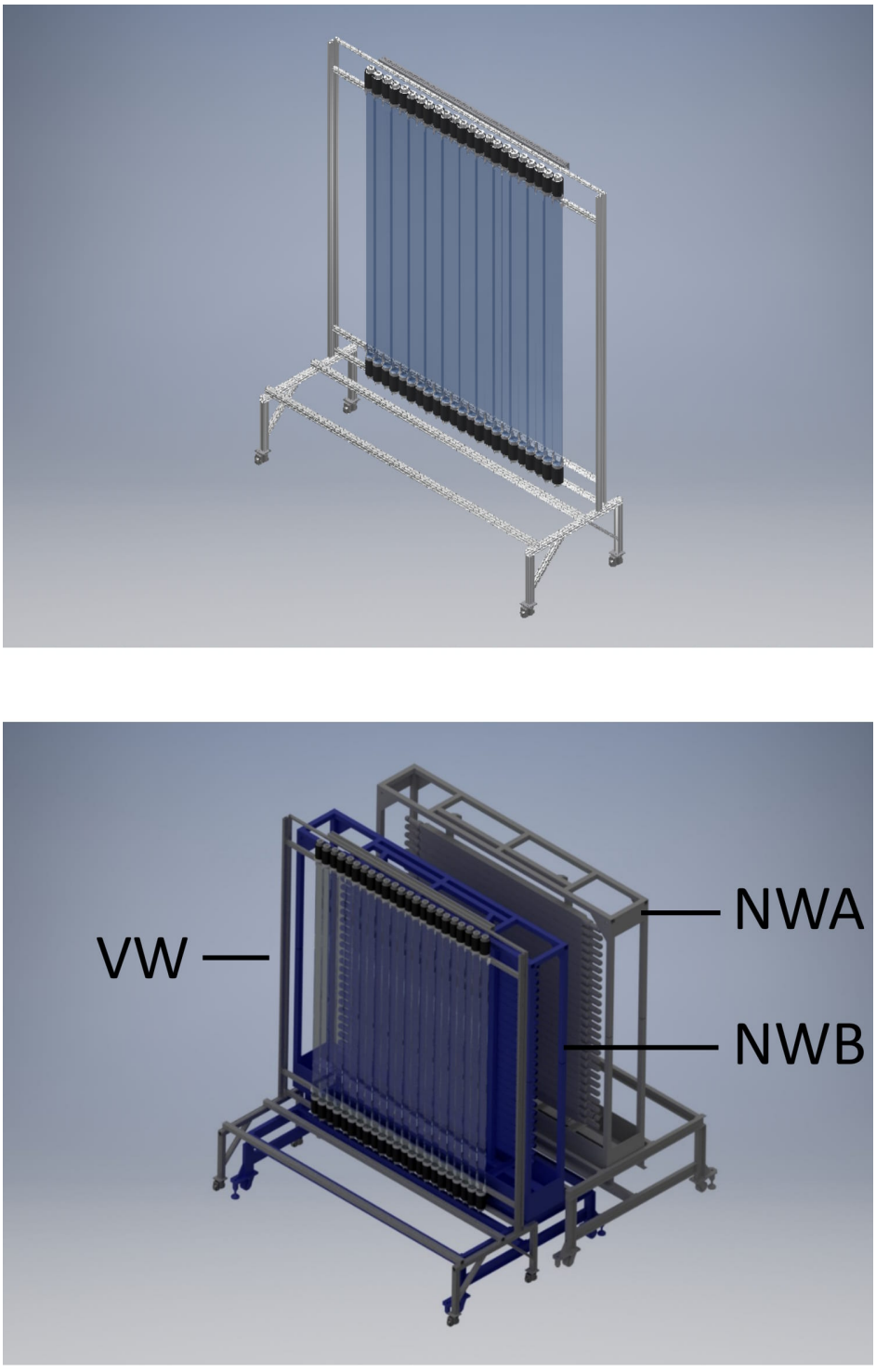

Figure 2.24: (Top panel) 3D sketch of the Charged-Particle Veto Wall. (Bottom panel) 3D sketch of the Charged-Particle Veto Wall and the LANAs nested together.

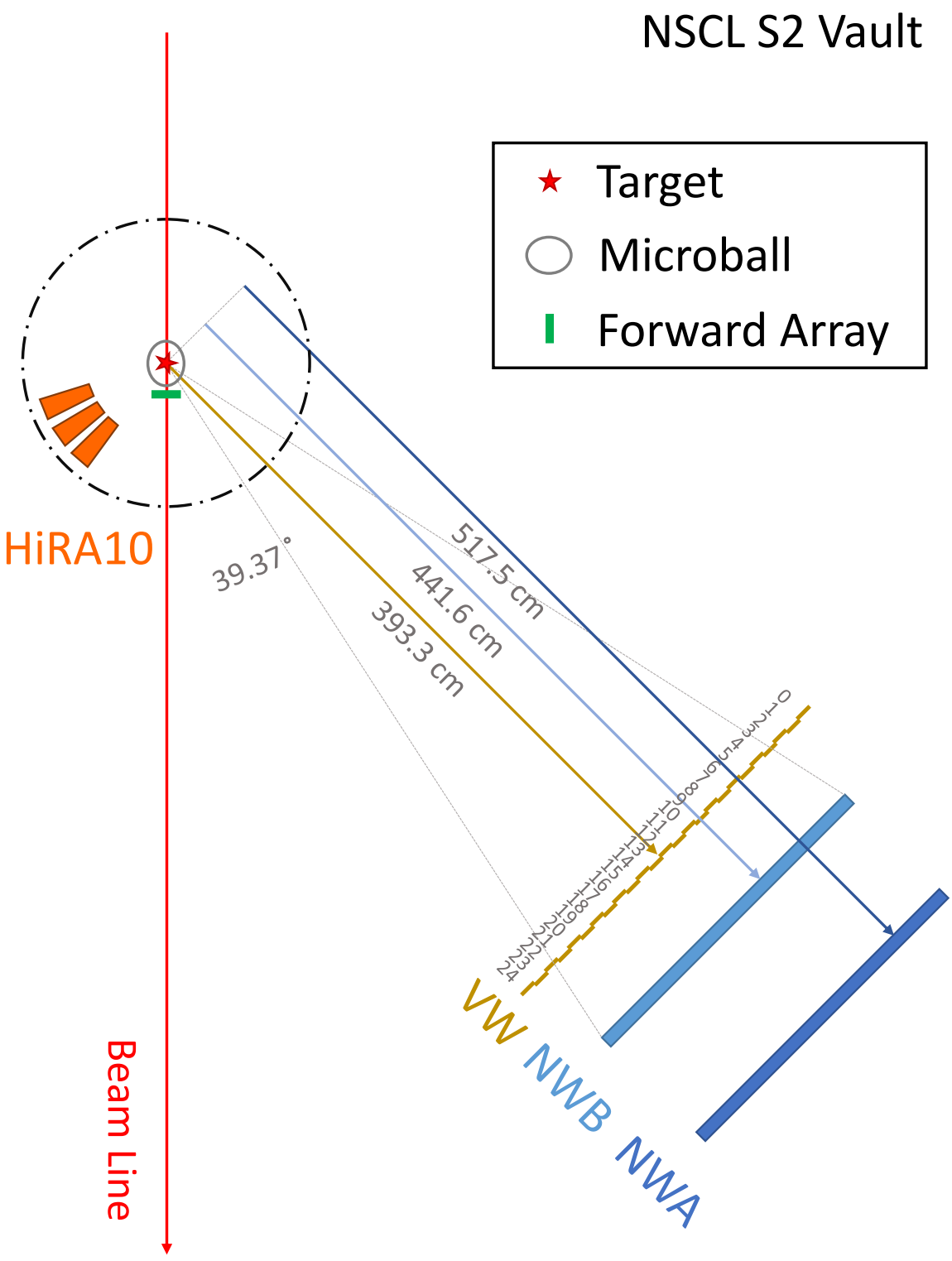

Figure 2.25: Top view of experimental setup schematic. The schematic reflects the sizes and distances to the target of the Charged-Particle Veto Wall (VW) and LANA (NWA and NWB) in scale. The VW+LANA assemble is moved to 39.37 ° . All distances are drawn to scale and determined from laser measurements.

Chapter 3

Data Analysis

3.1 Microball Impact Parameter Determination

In beam-target collision experiments, collisions are often characterized according to their impact parameter b. Typically, collisions with smaller impact parameter have more nucleons participating in compress-expand process, resulting in more particles emitted and larger multiplicity (number of particles detected in a given detector).

The Microball is used to measure the charged-particle multiplicity, which is assumed to decrease monotonically with impact parameter b. The probability of producing particles with multiplicity $\leq N_c$ is proportional to the geometrical area of a disk with radius $b(N_c)$, we can calculate the deduced impact parameter, $\hat{b} = b/b_{max}$, which is a dimensionless variable associated with the centrality of the collision, using the following formula [90, 91, 92, 93, 94]:

$$\hat{b}(N_c) = \frac{b(N_c)}{b_{max}} = \frac{\sqrt{\sum_{N_c}^{\infty} P(N_c)}}{\sqrt{\sum_{N_c=1}^{\infty} P(N_c)}} \tag{3.1}$$

where N_c is the number of charged-particle detected in Microball, $P(N_c)$ is the probability of events with multiplicity equal to N_c. The probability of event having N_c multiplicity is

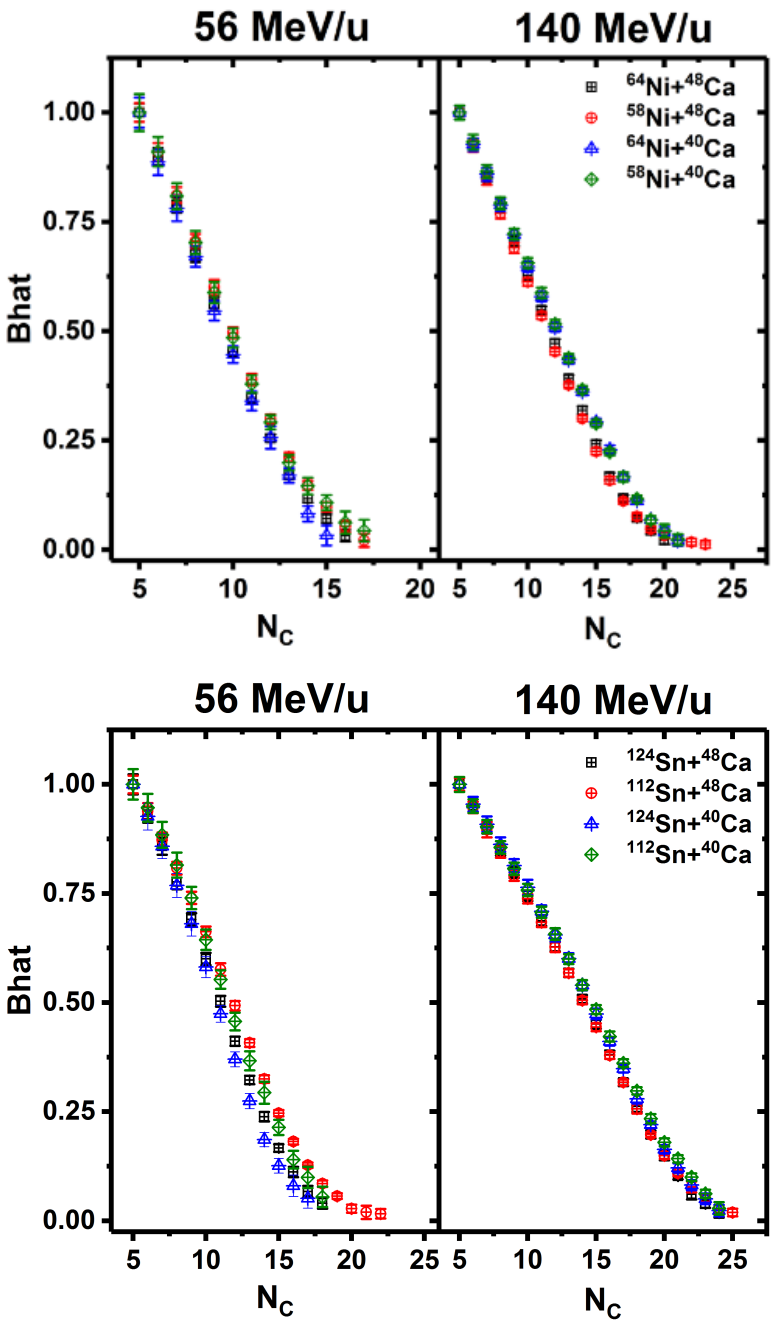

Figure 3.1: Correlations between the induced impact parameter $\hat{b}$ and Microball multiplicity N_c for 16 reaction systems. On the upper right corners of two panels, the reaction systems are labeled as target+beam. The top panels are for Ni target reaction systems and the bottom panels are for Sn target reaction systems. The left panels have lower beam energy of 56 AMeV and the right panels have higher beam energy of 140 AMeV.

calculated using:

$$P(N_c) = \frac{C(N_c)}{\sum_{N_c=1}^{\infty} C(N_c)} \tag{3.2}$$

where $C(N_c)$ is the counts of events with Microball multiplicity N_c.

The relationships for all 16 reaction systems between the induced impact parameter $\hat{b}$ and Microball multiplicity N_c are shown in figure 3.1. The top panels of figure 3.1 summarize the $\hat{b}$-N_c correlations for Ni target while the bottom panels are for Sn target. With the b_{max} given in table 3.1, we can calculate the impact parameter of any event using equation 3.1. The majority of the work mentioned in this section was done by Sean Sweany.

systems	^{58}Ni	^{64}Ni	^{112}Sn	^{124}Sn
^{40}Ca, 56 MeV/u	5.78	5.64	7.91	7.38
^{40}Ca, 140 MeV/u	5.85	5.92	7.61	7.47
^{48}Ca, 56 MeV/u	5.63	5.65	7.61	7.17
^{48}Ca, 140 MeV/u	5.05	5.95	7.45	7.25

Table 3.1: b_{max} table for all 16 beam-target-energy combinations in our experiment. The unit is barn, 100 fm^2.

3.2 LANA Analysis

3.2.1 LANA Calibration using cosmic rays

Typically, calibration of a neutron detector requires the use of radioactive sources that produce gamma rays with well-known energies [13, 95]. Nearly all of these sources have low energy gamma < 5 MeV. For large detector array, calibration has to be done at various po-

sitions along individual detector to determine the position dependence of the light collection of the photo-multipliers incorporated in the neutron detectors. Such procedures are tedious and time-consuming especially when the area of the arrays is large. Alternatively one can use nuclear reactions that produce neutrons at fixed energies for calibrations. The latter method requires accelerated ion beams which may not be readily available [96, 97].

The section below describes a method that uses high-energy muons produced in cosmic-ray showers to calibrate the light response of a large neutron array [98, 99, 100, 101]. The mean muon energy is ≈ 2 GeV [102]. This section will also show how the time and position resolutions of the array can be obtained and how to match the time difference of each neutron detector without an external timing detector. The method can be applied to other neutron detectors.

3.2.1.1 Impact position calibration

When an ionizing radiation strikes one of the bars of the neutron wall, scintillation light is isotropically produced in the NE-213 liquid scintillator along the ionization path. The X-position of the hit on the horizontal axis is extracted by comparing the time signals recorded by the PMTs at the two ends of the bar, while the vertical Y-position is constrained by the physical dimension of the scintillation fluid inside the bar.

Given t_{left} and t_{right} as the absolute times which correspond ideally to the arrival times of the scintillation light at the left and right PMT photocathodes, the horizontal position of the particle hit along the bar, with respect to the bar center, is given by:

$$X = \frac{t_{\text{left}} - t_{\text{right}} - \tau}{2}\bar{v} \tag{3.3}$$

where $\bar{v}$ is the average horizontal speed of the light propagating through the bar and τ is the residual delay since the timing for the left and right PMT and electronics channels are not exactly the same due to different cable length, different delays in electronic channels or modules etc. Because the cosmic rays hit the neutron wall bars with no preference, the hit distribution along one bar should be uniform. By using data collected with cosmic rays, we produced the time difference, $\Delta t = t_{\text{left}} - t_{\text{right}}$ distribution shown in the top panel of figure 3.2 for bar #8 of the LANA walls. As expected, the distribution is almost flat with two sharp edges, corresponding to the geometrical left and right ends of the bar. To determine the left and right edge consistently for all the bars, we perform a numerical differentiation of the time difference distribution spectrum. The result exhibits two sharp peaks, where the time difference differential diverges negatively at Δt_{max} or positively at Δt_{min} as shown in the bottom panel of Figure 3.2. A numerical peak finding method can then be used to infer the positions of the two edges. An analogous procedure is applied to all the bars. The following equations can be used to obtain the position calibration parameter of a bar:

$$\begin{aligned} \tau &= \frac{\Delta t_{\text{max}} + \Delta t_{\text{min}}}{2} \\ \bar{v} &= \frac{2L}{\Delta t_{\text{max}} - \Delta t_{\text{min}}} \end{aligned} \tag{3.4}$$

where L is the bar length.

After the position is calibrated, we define a cosmic track by fitting the impact positions measured in at least ten consecutive bars as schematically shown in figure 3.3. (Except in Section 5, no other conditions are imposed on the cosmic tracks.) From the fitted track (blue diagonal line passing through the bars in Figure 3.3) we can calculate the deviation (ΔX) between the impact position and that extracted from track reconstruction. Figure 3.4 shows

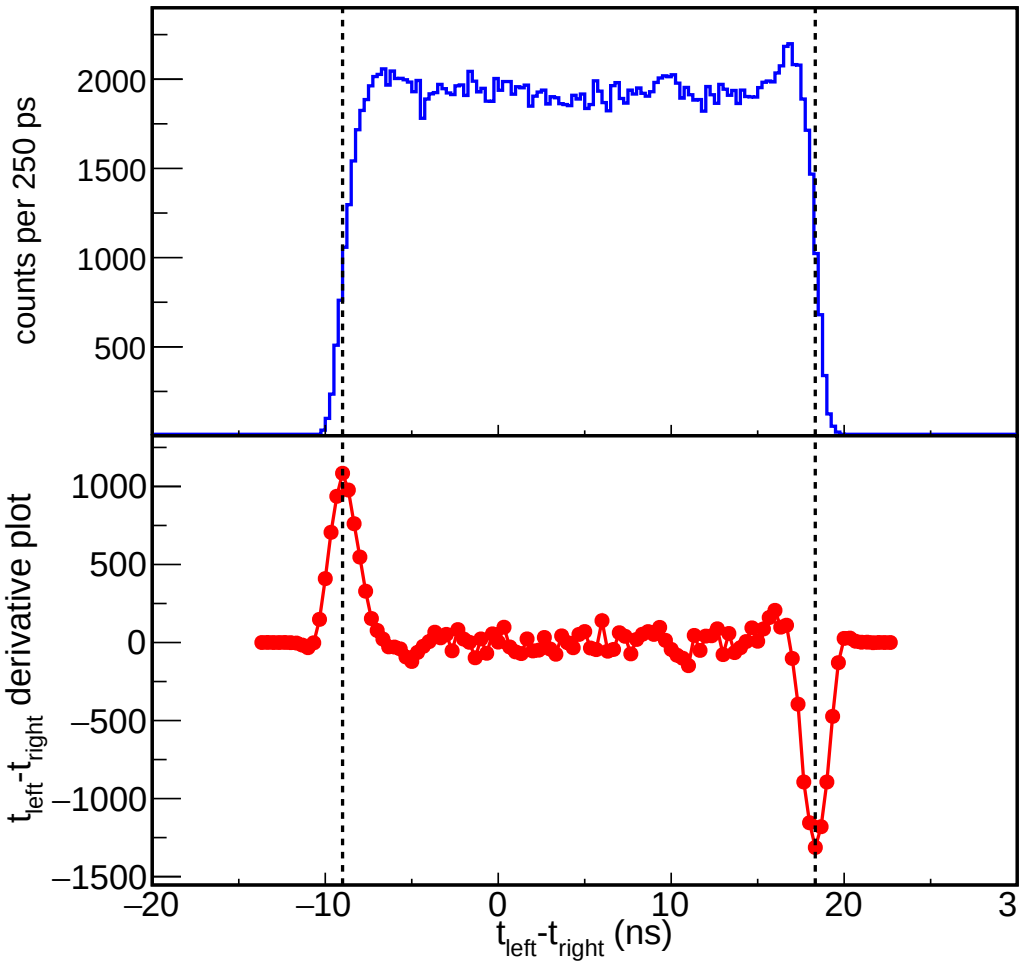

Figure 3.2: (top panel) Time difference, t_{left}-t_{right} distribution for cosmic muons obtained with bar #8 of the LANA. A numerical differentiation of this spectrum (bottom panel) is used to determine the position of right and left edges of the t_{left}-t_{right} distribution consistently as indicated by the dashed lines, which correspond to $-\frac{L}{2}$ and $\frac{L}{2}$ respectively.

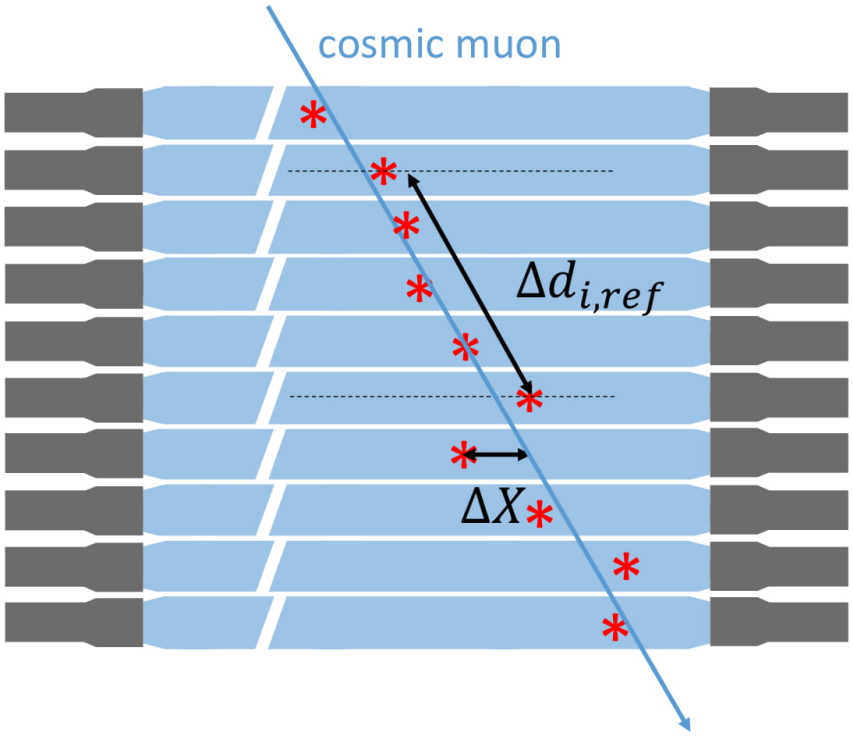

Figure 3.3: A schematic drawing of a cosmic muon track penetrating 10 consecutive bars in the wall. Red stars represent the hit positions. The reconstructed muon track (blue slanted line) is obtained by fitting the measured hit positions on the bars with a straight line. ΔX indicates the position deviation between the expected and the actual hit position. $\Delta d_{i,\mathrm{ref}}$ is the theoretical distance between two hits on a certain bar and reference bar respectively.

the ΔX distributions for Bar #8 with a FWHM of 6.92 cm, comparable to the position resolution obtained in Ref. [13]. The obtained position resolution is averaged over a LANA bar. It is worse towards the end of the bar due to attenuation of the light signal from the PMT located at the opposite end. It is worth noting that the above resolutions include the uncertainty in the track reconstruction. The X position resolution is similar to the height of the NE-213 liquid inside the Pyrex cell which determines the Y position resolution. The mean position resolution for all 25 bars is 8 $\pm$ 1.5 cm which is consistent with the position resolution obtained in Ref. [13] suggesting that the PMTs in LANA wall have not deteriorated even after 25 years.

Bar #8 of NWB is used as example in the analysis of Chapter 3.2.1. Table 3.2 and 3.3 list the ΔX and v of 48 LANA bars. Please note that we have in total 50 LANA bars. The bottom bars of the two LANAs are not used in our experiments because of the shadowing by the stainless steel stand that holds the shadow bars.

NWA Bar#	1	2	3	4	5	6	7	8	9	10	11	12
ΔX FWHM (cm)	7.60	7.15	11.4	9.18	9.34	8.95	11.6	6.02	6.88	6.09	6.87	8.20
v (cm/ns)	14.5	14.3	14.7	14.6	13.8	14.9	14.6	14.7	15.0	14.4	14.9	14.2
NWA Bar#	13	14	15	16	17	18	19	20	21	22	23	24
ΔX FWHM (cm)	6.17	6.29	6.89	6.44	7.05	8.32	6.78	6.82	6.99	6.76	7.96	10.1
v (cm/ns)	14.3	14.6	14.2	14.4	14.7	14.5	14.5	14.8	14.7	14.4	15.1	14.5

Table 3.2: The ΔX and v of each back LANA (NWA) bar.

NWB Bar#	1	2	3	4	5	6	7	8	9	10	11	12
ΔX FWHM (cm)	6.02	6.97	12.9	6.35	5.77	6.01	6.48	6.92	6.17	5.84	5.91	6.18
v (cm/ns)	15.5	14.9	15.4	14.9	16.0	14.7	15.5	14.5	15.4	15.0	15.4	14.8
NWB Bar#	13	14	15	16	17	18	19	20	21	22	23	24
ΔX FWHM (cm)	7.27	7.34	8.90	6.72	8.03	6.42	9.50	6.29	5.71	7.12	7.35	6.57
v (cm/ns)	15.5	14.9	15.4	14.9	16.0	14.7	15.5	14.5	15.4	15.0	15.4	14.8

Table 3.3: The ΔX and v of each front LANA (NWB) bar.

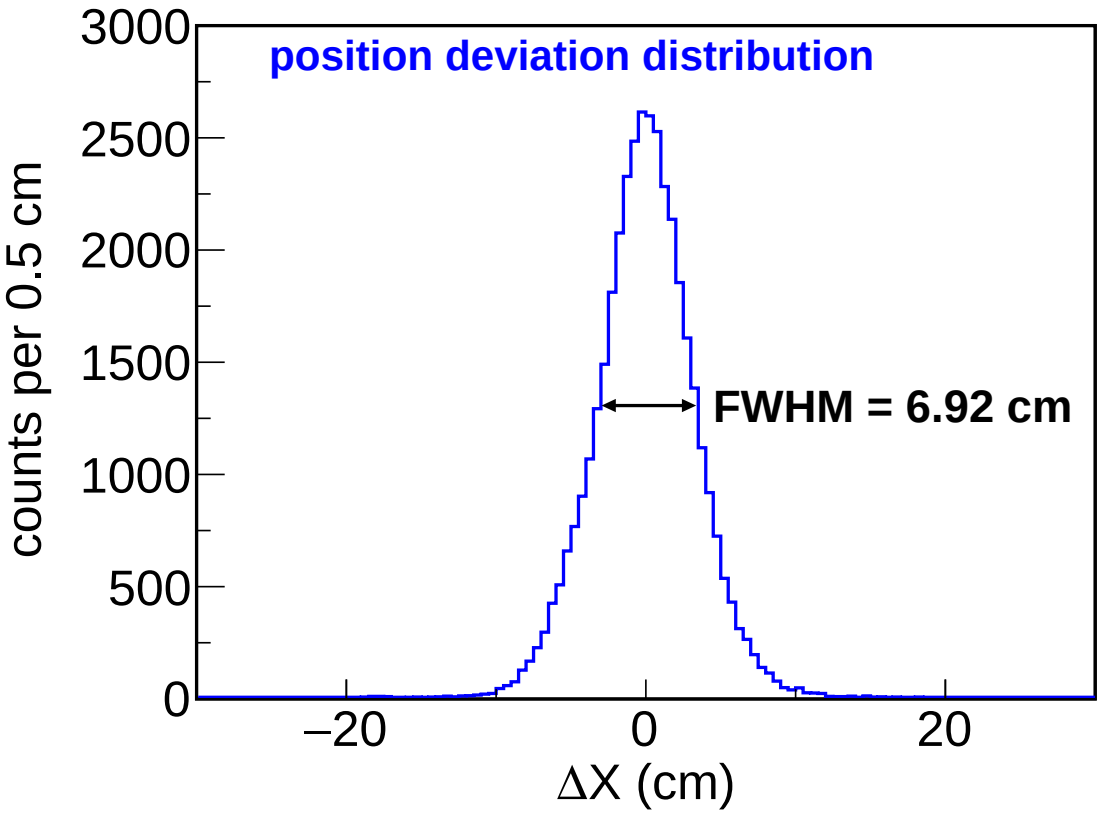

Figure 3.4: Position deviation distribution for bar #8.

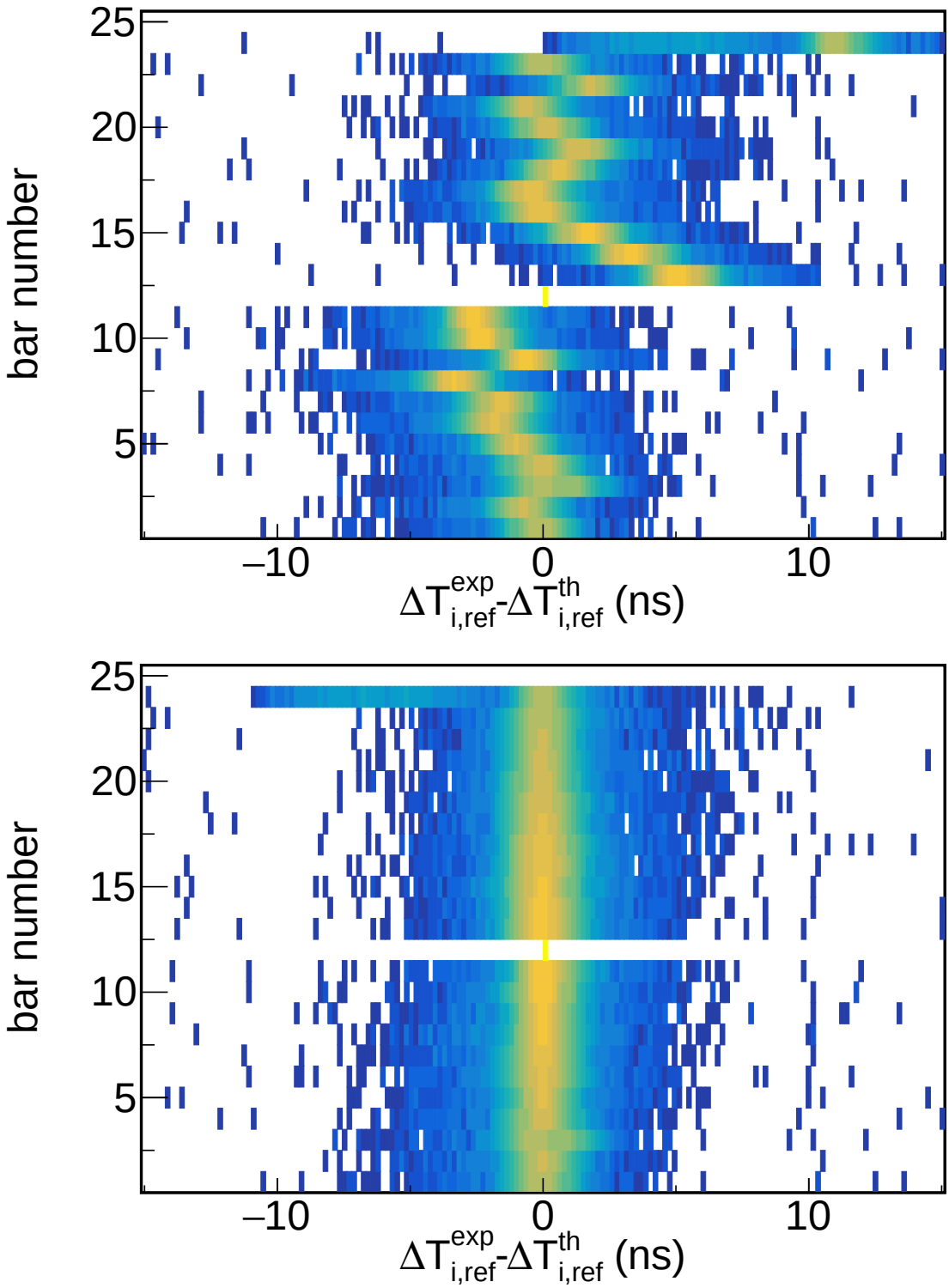

Figure 3.5: $\delta_{i,\mathrm{ref}}$ distributions for each of the bar in the array before (top panel) and after (bottom panel) the peaks are aligned. Y-axis is the bar number while X-axis shows the corresponding $\Delta T^{\mathrm{exp}}_{i,\mathrm{ref}} - \Delta T^{\mathrm{th}}_{i,\mathrm{ref}}$ distributions. Bar #12 is used as the reference bar; therefore $\delta_{12,\mathrm{ref}}$=0.

3.2.1.2 Time resolution and time offset calibration

Cosmic muons travel at nearly the speed of light. As illustrated in Figure 3.3, theoretically, one can calculate the expected arrival time difference of a cosmic muon track between two bars since we know the position of the bars accurately. The expected time difference of the signal recorded in a bar used as the reference and the i-th bar of a wall is given by:

$$\Delta T^{\text{th}}_{i,\text{ref}} = \frac{\Delta d_{i,\text{ref}}}{v} \tag{3.5}$$

where $\Delta d_{i,\text{ref}}$ is the theoretical length of the cosmic muon path from the i-th bar to the reference bar determined by the track fit, and $v \approx c$ is the speed of the cosmic muon. The time difference measured experimentally with TDC is given by:

$$\Delta T^{\text{exp}}_{i,\text{ref}} = \frac{(t_{\text{left}} + t_{\text{right}})_{\text{ref}}}{2} - \frac{(t_{\text{left}} + t_{\text{right}})_i}{2} + \delta_{i,\text{ref}} \tag{3.6}$$

where $\delta_{i,\text{ref}}$ is the time difference between bars arising from differing cable and electronic delays. Figure 3.5 shows the distribution of $\delta_{i,\text{ref}} = \Delta T^{\text{exp}}_{i,\text{ref}} - \Delta T^{\text{th}}_{i,\text{ref}}$ for each of the bars in a LANA wall. The Y-axis is the bar number, i. Bar #12 is chosen as the reference bar with the obvious result $\delta_{12,12} = 0$. Deviation of $\delta_{i,\text{ref}}$ from zero suggests that time delays arising from the differences in cable and electronic delays, etc are different for each bar. While we cannot determine the absolute time offset or delays for each bar, we can align the peaks of $\delta_{i,\text{ref}}$ to zero as shown in the lower panel of Figure 3.5. Figure 3.6 shows a Gaussian shape distribution of $\delta_{i,\text{ref}}$ for bar #8 with FWHM of 751 ps. The time resolution, FWHM, for bar #8 involving two PMTs can be deduced as: $\frac{751 \text{ ps}}{\sqrt{2}} = 531$ ps. The average time resolution for all 24 bars is 504 ± 106 ps. However, this time resolution cannot be compared directly to the time resolution of 1 ns obtained in Ref. [13] which involves the use of an external time

zero Si detector. Our time resolution reflects the time response of the PMTs which are quite similar as reflected by the standard deviation of the mean.

3.2.1.3 Light attenuation length and photomultiplier gain-matching

When an incident particle interacts with the NE-213 liquid, only a small fraction of the produced optical photons directly reach the PMTs, while some photons are lost completely and the rest of the photons experience multiple reflections on the surface of the Pyrex glass cell before being collected by the PMTs. The photons that reach the photocathodes are detected by the left and right PMTs attached at the end of the Pyrex tubes and converted to charge by the QDC in Figure 2.14. The measured charge is a function not only of the number of photons produced by the incident particle (and therefore of the energy deposited by the particle in the material) but also of the hit position X as described below:

$$\begin{aligned} Q_{\text{right}}(N, X) &= g_{\text{right}} \frac{N}{2} e^{-\frac{L/2-X}{\lambda}} \\ Q_{\text{left}}(N, X) &= g_{\text{left}} \frac{N}{2} e^{-\frac{L/2+X}{\lambda}} \end{aligned} \tag{3.7}$$

where g_{right} and g_{left} are the gain of the corresponding PMT, L is the bar length, N is the total number of photons emitted and λ is the technical attenuation length of the scintillator material in our detector to optical photons. The attenuation length describes the self-absorption in the material and also includes the effect of geometry. λ is therefore, normally smaller than the material bulk light attenuation length, which is ∼270 cm [81]. The logarithm of the ratio of Equation (3.7) gives a linear expression:

$$\ln(\frac{Q_{\text{right}}}{Q_{\text{left}}})(x) = \frac{2}{\lambda} X + \ln(\frac{g_{\text{right}}}{g_{\text{left}}}) \tag{3.8}$$

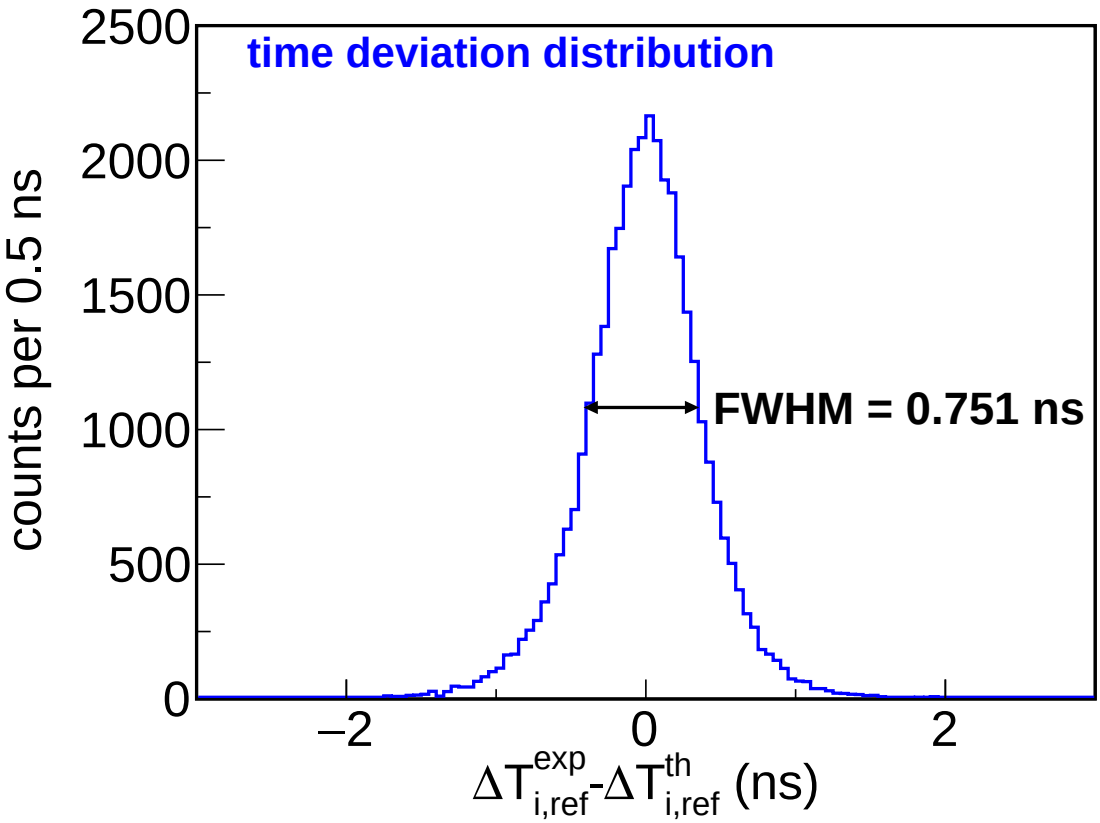

Figure 3.6: Time deviation distribution for bar #8.

with a slope equal to $\frac{2}{\lambda}$ and an intercept $\ln(\frac{g_{\text{right}}}{g_{\text{left}}})$. Figure 3.7 plots the gain ratio of the two PMTs $\ln(\frac{Q_{\text{right}}}{Q_{\text{left}}})(X)$ as a function of X for bar #8. The distribution is mostly linear with some curvature at large absolute X values due to the light collection efficiency near the end of the bar. The red dashed line is the result of a linear fit of data from -90 cm to 90 cm to avoid any possible effect from the end of the bar. We have varied the range of fit from (−80 cm, 80 cm) to (−90 cm, 90 cm) and find that the fitting results are stable to within 1%. The mean λ value for all the bars in the array is 94 ± 8 cm. Thus the light attenuation effects are significant in the LANA bars, due to their size and geometry.

Table 3.4 and 3.5 below list the λ of 48 LANA bars. We can see that in general NWA bars have shorter attenuation length, this is probably because the liquid scintillator leaking problem is more severe for NWA so that an air gap was created between liquid scintillator and the pyrex container walls, resulting in less efficient photon reflection.

NWA Bar#	1	2	3	4	5	6	7	8	9	10	11	12
λ (cm)	66	59	60	80	66	92	62	89	85	78	81	68
NWA Bar#	13	14	15	16	17	18	19	20	21	22	23	24
λ (cm)	79	79	69	79	83	74	79	80	88	81	80	59

Table 3.4: The light attenuation length λ of each back LANA (NWA) bar.

NWB Bar#	1	2	3	4	5	6	7	8	9	10	11	12
λ (cm)	90	102	82	102	107	101	95	88	85	109	87	102
NWB Bar#	13	14	15	16	17	18	19	20	21	22	23	24
λ (cm)	108	84	84	101	84	88	90	87	92	96	102	99

Table 3.5: The light attenuation length λ of each front LANA (NWB) bar.

Equation (3.8) also facilitates matching the gain of left and right PMTs of each bar to allow for uniform performance along the bar using the following procedure. A cosmic ray run is performed to produce a plot similar to Figure 3.7. The intercept extracted with a

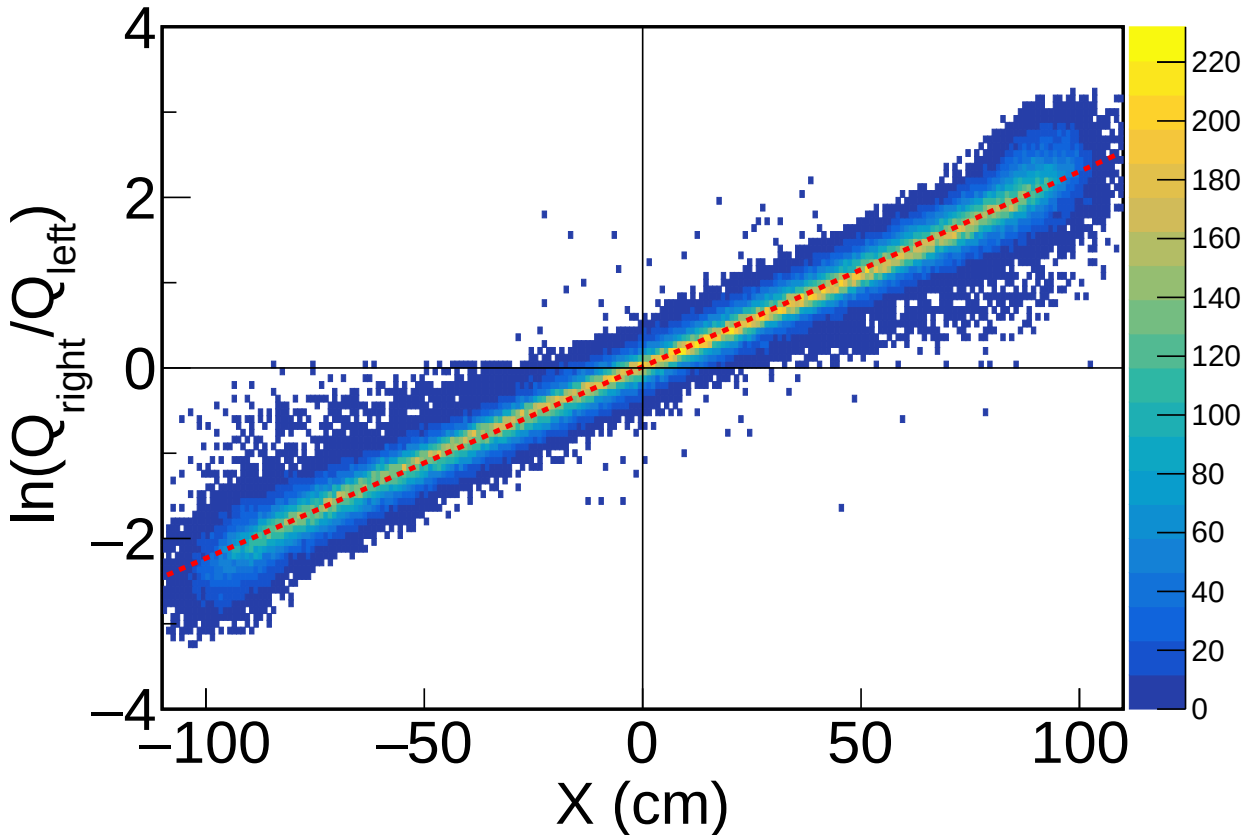

Figure 3.7: Equation (3.8) as a function of the position X along the bar #8 for cosmic ray data. The red dashed line is a linear fit of the distribution. The intercept of the best fit line is compatible with (0,0), indicating a good left-right matching of the PMT gains. The slope allows to extract the attenuation length of the bar.

linear fit is the left-right gain ratio. Using the power-law of the high voltage (HV), gain $\sim (HV)^N$, (e.g. $N \sim 8$ for LANA) a new gain setting is chosen to minimize the intercept. It takes about 3 iterations to adjust and match all HV for 100 PMTs in LANA in order to consistently equalize the PMT gains for all the bars with $(\frac{g_{\text{right}}}{g_{\text{left}}})$, close to one. One can also use the vanishing intercept in Equation (3.8) to judge the quality of the gain matching in offline analysis. In our case, the statistics from an overnight cosmic run is sufficient for one iteration. The same method can also be used between experimental runs to monitor the gain of the neutron detection array.

3.2.1.4 Light output calibration and position corrections

To determine the light output threshold and to calculate neutron detection efficiency from simulation, we need to calibrate neutron signal's light output to MeV electron equivalent (MeVee). Cosmic muons reaching the sea level have a mean energy of 2 GeV [102, 99, 101]. The most probable energy deposited in the scintillator material by such muons depends on the length of their path in the material. We simulate the interaction of 2 GeV muons with the NE-213 material by using the GEANT4 toolkit and the standard electromagnetic physics list. Our simulation indicates that, if muons punch through the bar vertically, the expected deposited energy has a Landau distribution whose most possible value (MPV) is 11.96 MeV.

To calibrate the neutron detectors, we require the incident angles of the cosmic muon track to the axis to be within 10 degree perpendicular to the horizontal central axis of the bar. This is to ensure the shortest track path in the scintillating liquid in the neutron bar to be consistent with the simulations, in order to achieve accurate determination of the energy loss by the cosmic muons. The 10 degree condition is chosen so that the uncertainties of transverse length of the track in a bar is consistent with the position resolution of the bars.

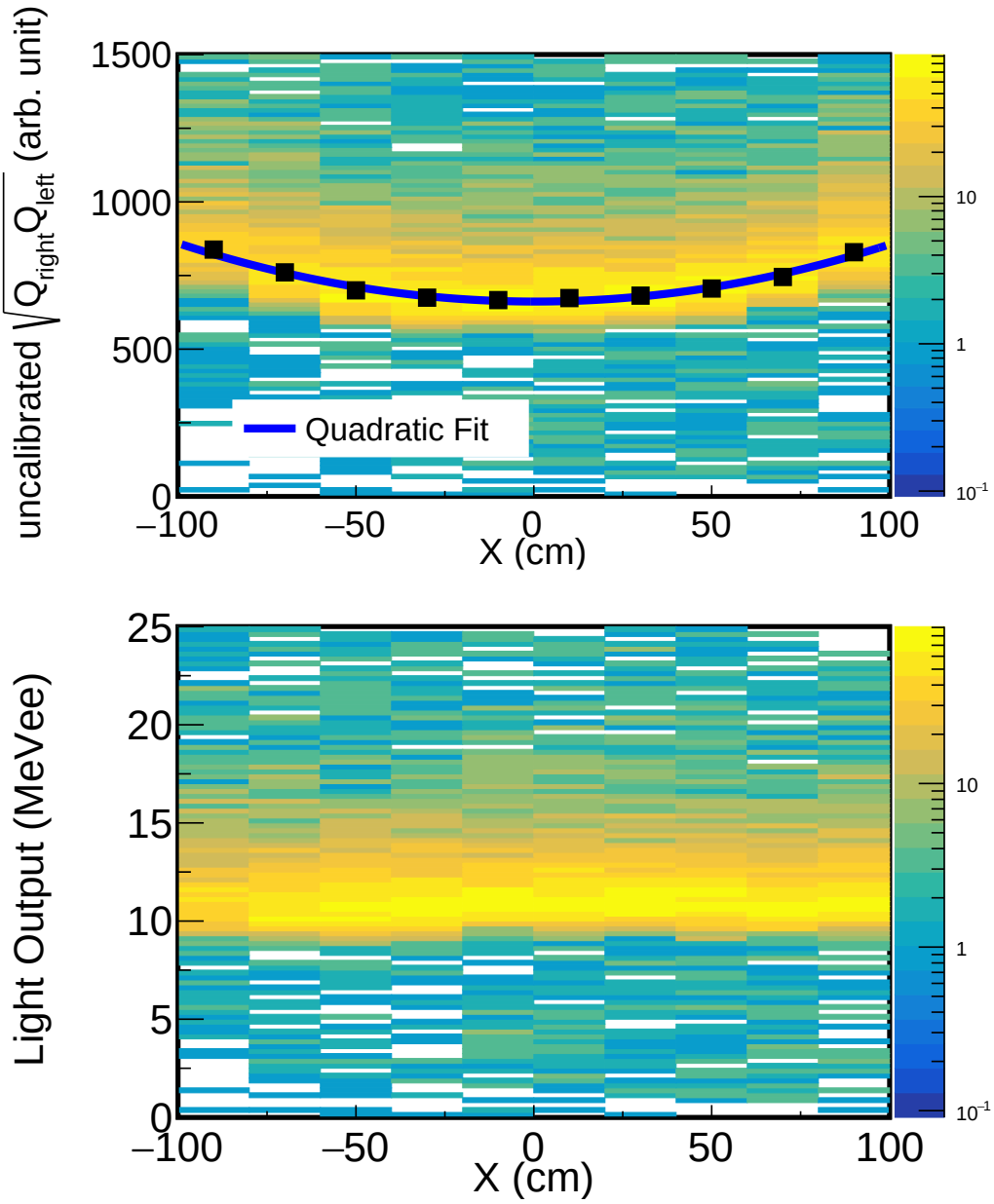

Figure 3.8: (Top panel) Uncalibrated left-right GM as a function of the position along bar #8. Vertical cosmic rays are selected by restricting data to impinging angles $-10^{\circ} \leq \theta \leq 10^{\circ}$ with respect to the axis perpendicular to the bar length. Black points are the position of the cosmic ray MPV deduced with a Landau fit of data for each position bin. The blue line is the result of a quadratic fit of the cosmic MPV position dependence. (Bottom panel) Same as top panel after light calibration and position dependency correction.

To minimize the position dependence, the geometric means (GM) of the charges in the left and right PMTs defined below is typically used for the energy-light calibrations of neutron detectors:

$$\sqrt{Q_{\text{left}}(N,X)Q_{\text{right}}(N,X)} = f(N) = \frac{N}{2}\sqrt{g_{\text{left}}g_{\text{right}}e^{-L/\lambda}} \tag{3.9}$$

Figure 3.8 shows the GM distributions of bar #8 with a bin width of 20 cm. Consistent with the GEANT4 simulations, the GM distribution shown in Figure 3.9 has a Landau shape. The black squares in Figure 3.8 (top panel) show the MPV of the Landau GM distributions of vertically-penetrating cosmic rays as a function of X position. The statistical uncertainties of the black squares are smaller than the size of the marker. Despite using the GM of Equation (3.9), there is still some position dependence, most likely coming from the position dependence of the light collection due to scattering and reflections along the bar. This residual position dependence can be corrected empirically by flattening the experimental GM distribution for each X position using a parabolic fit of MPV (blue line in Figure 3.8 (top panel)). The flattened or corrected GM vs X-position spectrum is shown in Figure 3.8 (bottom panel), where the MPV of the GM has been calibrated to 11.96 MeVee.

To validate the cosmic ray energy-light calibration procedure, we placed an intense Americium-Beryllium (AmBe) neutron source at a distance of about 60 cm from the front of the LANA walls. Such source emits a mono-energetic 4.44 MeV gamma-ray from the reaction of $\alpha + {}^{9}\text{Be} \rightarrow n + {}^{12}\text{C}^{*}$. A typical AmBe gamma spectrum obtained with bar #8 is shown in Figure 3.10. The sharp Compton edge expected to lie at 4.2 MeV, can be easily defined. We calibrate the Compton edge of the gamma spectra by fitting it with the sum of a Fermi function and a linear background. The Fermi function is of the form $f(x) = \frac{a_0}{\exp\frac{x-a_1}{a_2}+1}$, where a_0,a_1,a_2 are free parameters. The position of the Compton edge is determined from the a_1 parameter by using the method proposed in Reference [103]. The open star in Figure 3.11

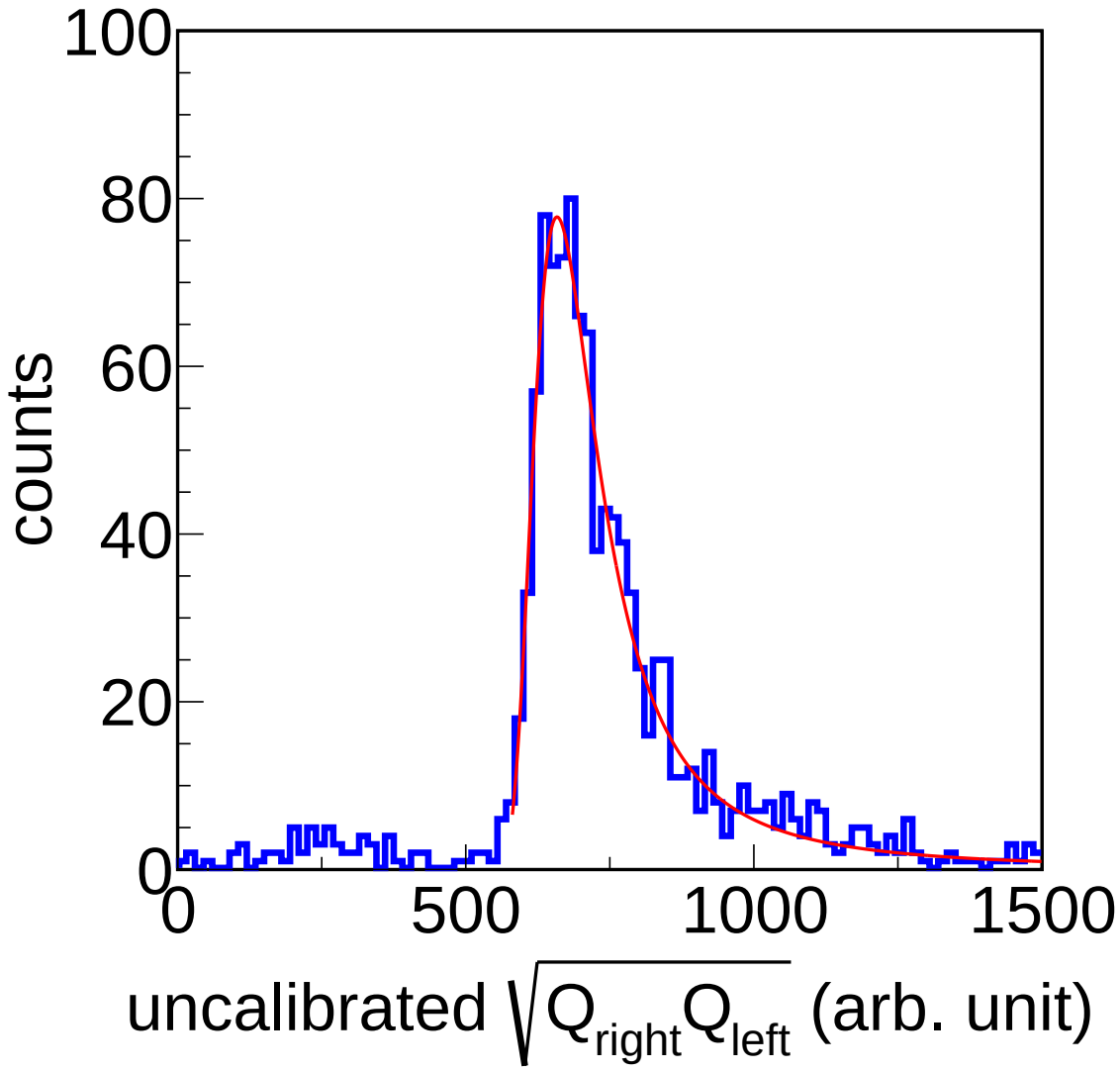

Figure 3.9: An example of a Landau fit of the GM distribution for the position bin -20 cm $\leq$ X $\leq$ 0 cm.

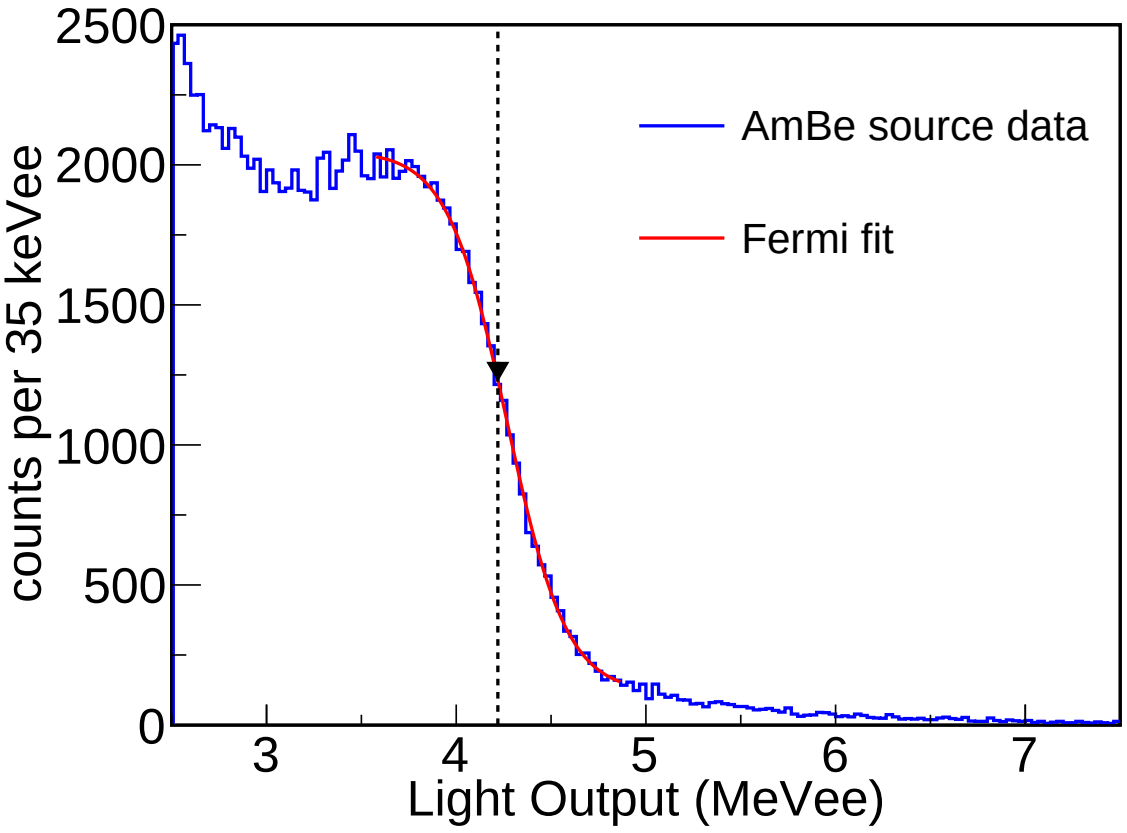

Figure 3.10: Position corrected light output spectrum obtained with an AmBe source for bar #8. The Compton edge is fitted with a Fermi function and the deduced position associated to the 4.44 MeV transition in ^{12}C is indicated by an arrow and a dashed line. The theoretical value of the Compton edge is 4.2 MeV.

shows that the 4.2 MeV from the Compton edge calibration lies along the red line obtained from the cosmic calibration at 11.96 MeVee and the zero offset of the electronics confirming the validity of our calibration procedure. The statistical uncertainties of the blue square, open star and blue circle points are smaller than the size of the marker in Figure 3.11.

By selecting cosmic tracks at large incidence angle, the calibration can be extended to higher energy depositions. We select cosmic muons that punch through the detector at 44.4 $\pm$ 5 and 56.3 $\pm$ 5 degrees with respect to the axis perpendicular (0 deg) to the bar length. According to the GEANT4 simulations, such muons should deposit 15.4 and 19.8 MeVee. These points are added to Figure 3.11 as the blue open circles. It appears that the light response remains linear out to 20 MeV.

3.2.2 Time calibration with the Forward Array

We use Time of Flight (ToF) technique to measure the velocity and therefore energy of neutron. In ToF measurement, the upgraded forward array is used as start-time detector and the LANA is used as stop-time detector. The distances between the target and LANA are 4.42m for the front wall and 5.18m for the back wall. After a nucleon-nucleon collision, because of the large angular coverage of forward array at forward angle, it is almost certain that several emitted charged-particles will hit the forward array. To accommodate multi-hits, forward array has 18 scintillation segments which greatly reduce the chance of having two particles hitting on one segments and thus improves time resolution. The earliest time recorded by a forward array element is assumed to be t_{start} and t_{stop} is the time triggered by a particle detected at LANA. Assuming this is a neutron, it takes $t_{stop} - t_{start}$ to fly from the target to LANA neglecting the short time for the detected particle to reach the forward array which is located at around 10 cm from the target. and therefore its velocity is

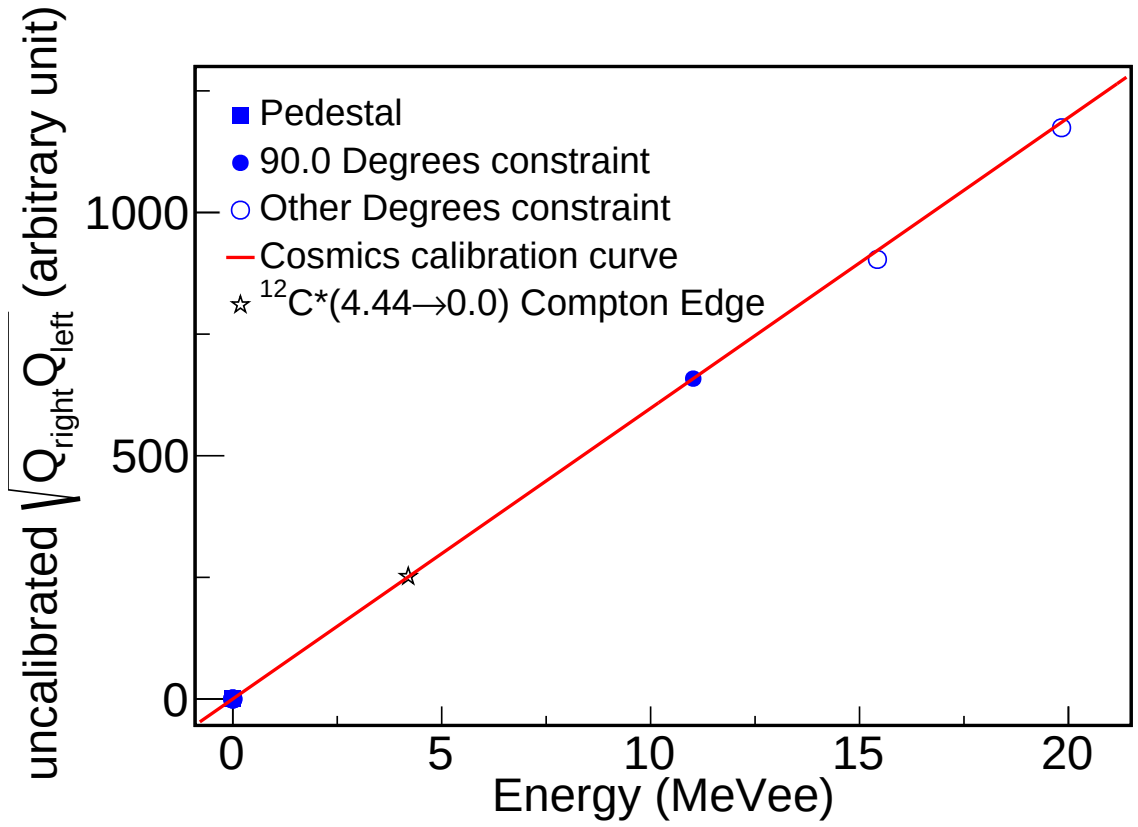

Figure 3.11: The cosmic-ray energy-light calibration curve (red line) obtained by using the 11.96 MeVee constraint of the cosmic muons and the zero-offset (blue solid circle and blue square, respectively). The open star corresponds to the Compton edge discussed in Figure 3.10. The open blue circles are two additional light-energy calibration points obtained by select cosmic muons that punch through the detector at 44.4 $\pm$ 5 and 56.3 $\pm$ 5 degrees with respect to the axis perpendicular to the bar length.

$v_{neutron} = D/(t_{stop} - t_{start})$ where D is the distance between target and where this neutron hits the LANA. In principle, the subtraction between two timings t_{FA} and t_{LANA} directly recorded by two detectors will be $t_{stop} - t_{start} + C_{random}$. C_{random} is a random time offset caused by different cable lengths and electronic module channels.

We use prompt gamma to do ToF time calibration. Prompt gamma rays are emitted immediately after or during the nuclear reaction. Because photons always travel at the speed of light, we can utilize them to calibrate time. Figure 3.12 is a time of flight spectrum from the LANA and forward array. The narrow peak at the left of the spectrum comes from prompt gamma rays.

By checking the signal of prompt gamma rays using 2D plot as shown in the top panel of figure 3.13, we can correct ToF for forward array time walk and synchronize all 18 forward array segments to compensate for time delays from different cable lengths or electronic module channels. The y-axis in figure 3.13 is raw QDC channel for a certain forward array segment and the x-axis is the average timing for the left and right PMTs on NWB minus forward array timing before (top) and after (bottom) time walk correction. The light blue region in the center of the plot corresponds to the events of prompt gamma rays. Ideally, the time of flight of prompt gammas should be independent of the magnitude of the gamma signal, which means the red line in top panel of figure 3.13 should be vertical independent of the energy of the particle. Instead, in the top panel of figure 3.13 we can see that the light blue region is tilted towards right which results from the fact that a stronger FA signal would cause an earlier triggering time. This dependence of the trigger time on the signal's magnitude is called *time walk* effect. To correct for this effect, first we fit the light blue

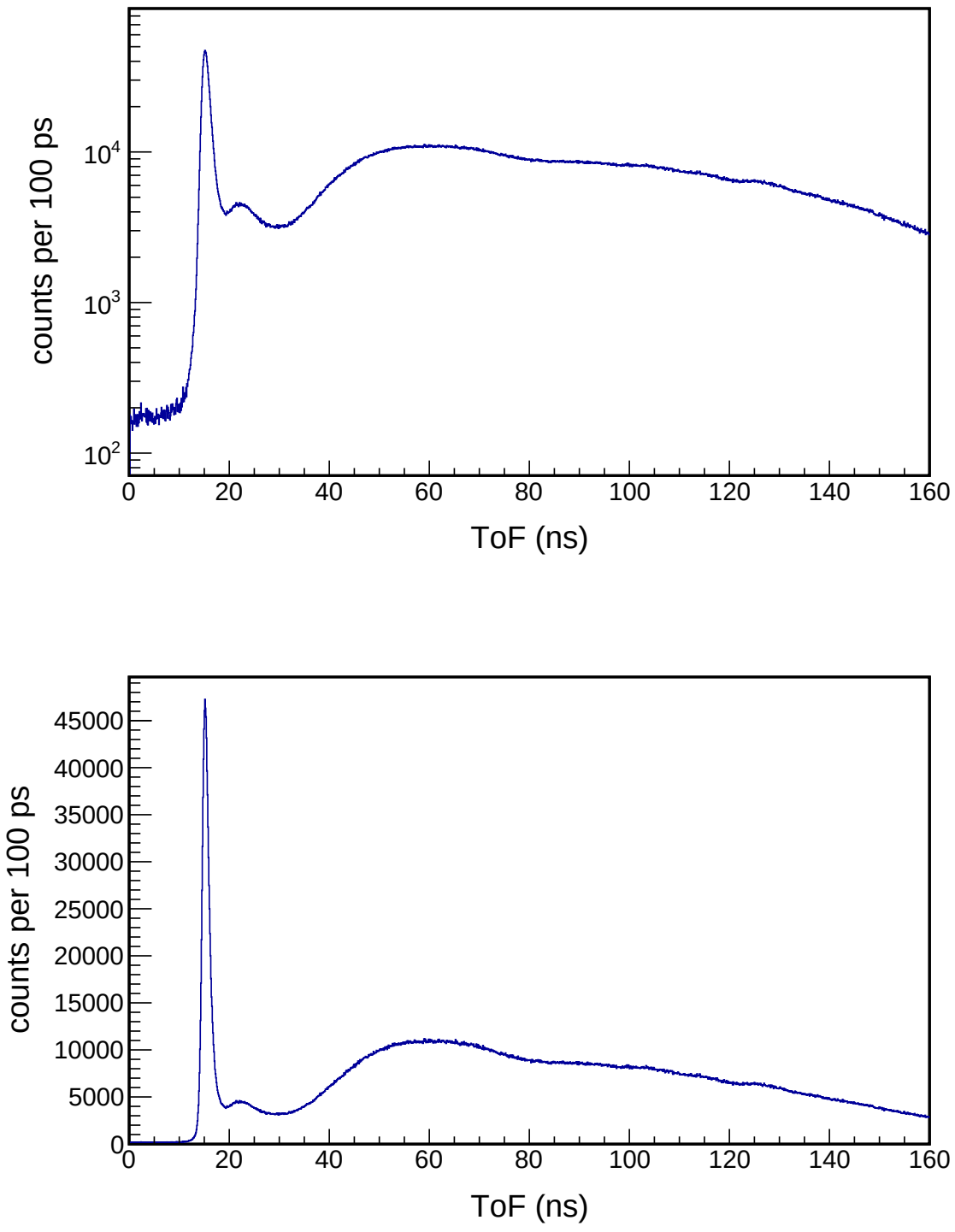

Figure 3.12: A time of flight spectrum from NWB with log (top panel) and linear (bottom panel) scale. The narrow peak at the left of the spectrum comes from prompt gamma rays, which arrives the LANA all together and earlier than any other particles. This plot is from $^{48}Ca +^{124} Sn$ at $E/A = 56\, MeV$ reaction.

region using a function in form of:

$$Channel = (\ln \frac{\Delta t - a}{b})/c \tag{3.10}$$

or we can write this relationship:

$$\Delta t = a + b * e^{c*Channel} \tag{3.11}$$

where a, b, c are three free fitting parameters. Please note that other forms of function that can reproduce the time walk effect are also acceptable. Then we can calculate corrected FA trigger time using:

$$t_{corrected} = t - (a + b * e^{c*Channel}) \tag{3.12}$$

Equation 3.12 also synchronizes 18 forward array segments at the same time. Figure 3.13 shows the difference before and after time walk effect is corrected. After correction, the arrival time of prompt gamma rays is independent of signal amplitude.

After the time walk effect is corrected for each FA segment, we need to choose the start time from eighteen FA segments' time signals. We can either choose the earliest time among eighteen FA segments' signals (FA Time Min) or calculate the average time among them (FA Time Mean). To decide which value to choose, we compare the resolution of the prompt gamma ray' peak. A better choice of FA start time should result in a smaller FWHM of the peak thus better time resolution. Because different positions on NWB have different distances to the target (4.42 meters to 4.53 meters), in order to accurately reflect the time resolution, we normalize the ToF spectrum which is a histogram of $ToF * \frac{D_{shortest}}{D}$. $D_{shortest}$ here takes the minimum distance between the target and LANA but other values such as the average

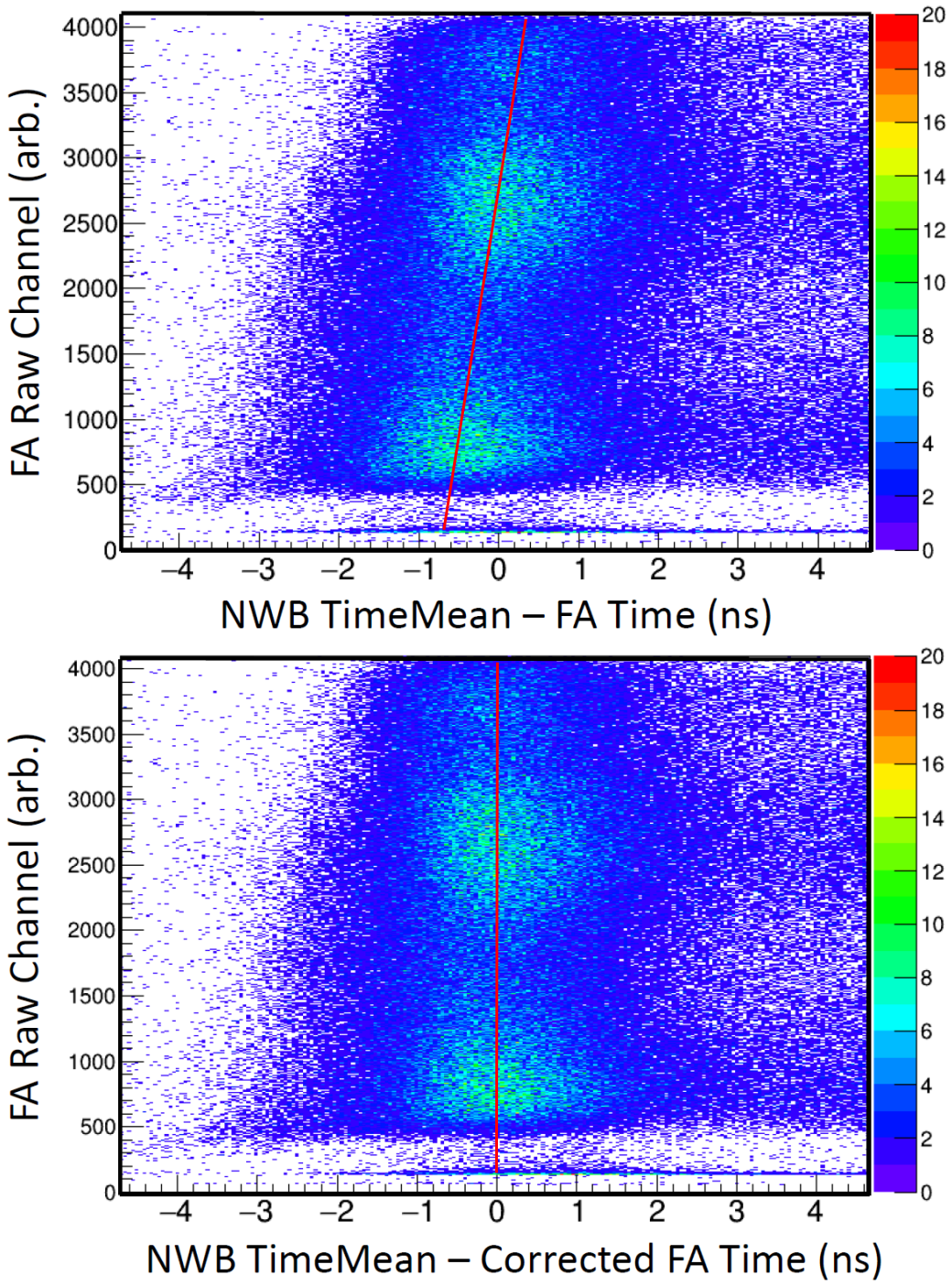

Figure 3.13: 2D plot of FA segment QDC raw channel versus the timing subtraction between NWB and a FA segment. Top panel is before walk in effect correction and bottom panel is after correction. The red curve in top panel is a fitted function in form of Eq. 3.11.

distance also work. The idea behind normalized ToF is to cancel out the time differences brought by different flight distances. Figure 3.14 shows the FWHMs of normalized ToF using minimum (top panel) and mean (bottom panel) value from FA segments time signal. The time resolution is found to be 1.53 ns and the time resolution difference between these two choices is negligible.

3.2.3 Geometry Efficiency

Figure 3.15 displays the hit distribution pattern Φ-Θ plane for the front LANA (NWB) using Geant4 simulation. Geant4 generates 1 million test particles and emits them from the position of target uniformly in Φ-Θ plane. For test particles that hit LANA scintillation material in simulation, we record the spherical coordinates (Φ, Θ) of the hits. In simulation, the LANA is placed in the same position according to laser measurements [14] done in experiments. In laser measurements, the positions of 4 fiducial marks were measured in each LANA wall. From the 3D mechanical drawings of LANA, we know the accurate positioning of all LANA bars. For different Θ, LANA's coverage in azimuthal direction is different. To correct for this, we calculate the fractional azimuthal coverage f_Φ as a function of polar angle Θ which represents LANA's coverage fraction of 2π in azimuthal direction at a certain Θ. By using the simulation done within Figure 3.15, we can calculate f_Φ in this way: at certain Θ, we choose a small bin of Θ (for example, 0.2 °) and then $f_\Phi(\Theta)$ =(number of particles detected at this bin)/(number of particles emitted at this bin). Figure 3.16 shows the f_Φ as a function of polar angle Θ for LANA. With f_Φ, we can calculate the observable we are interested at, such as $\frac{dM}{dE_k}$ using

$$\frac{dM}{dE_k} = \frac{dM_{measured}}{dE_k * f_\Phi(\Theta)} \tag{3.13}$$

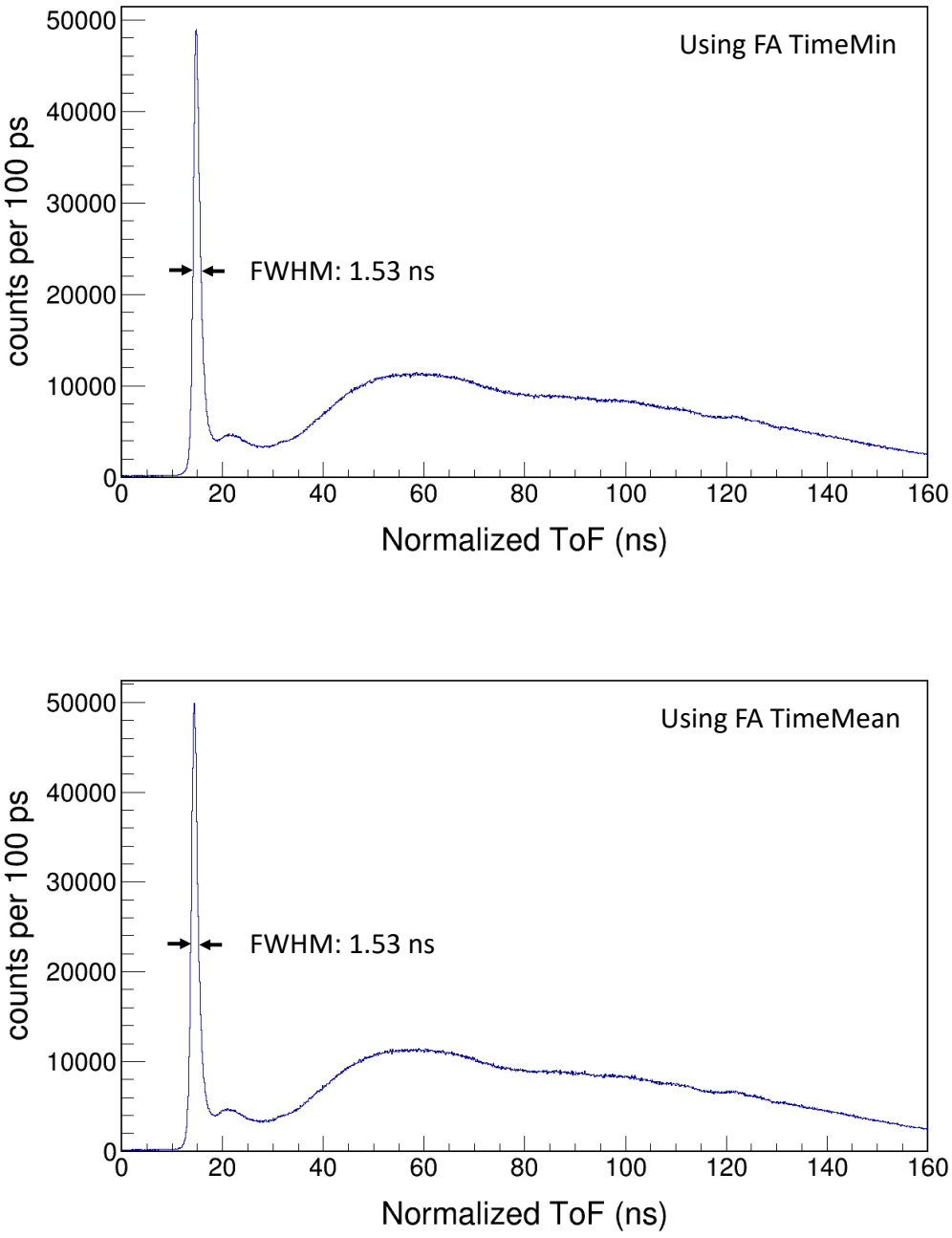

Figure 3.14: Normalized ToF spectrum from NWB with FA Time Min (top panel) and FA Time Mean (bottom panel).

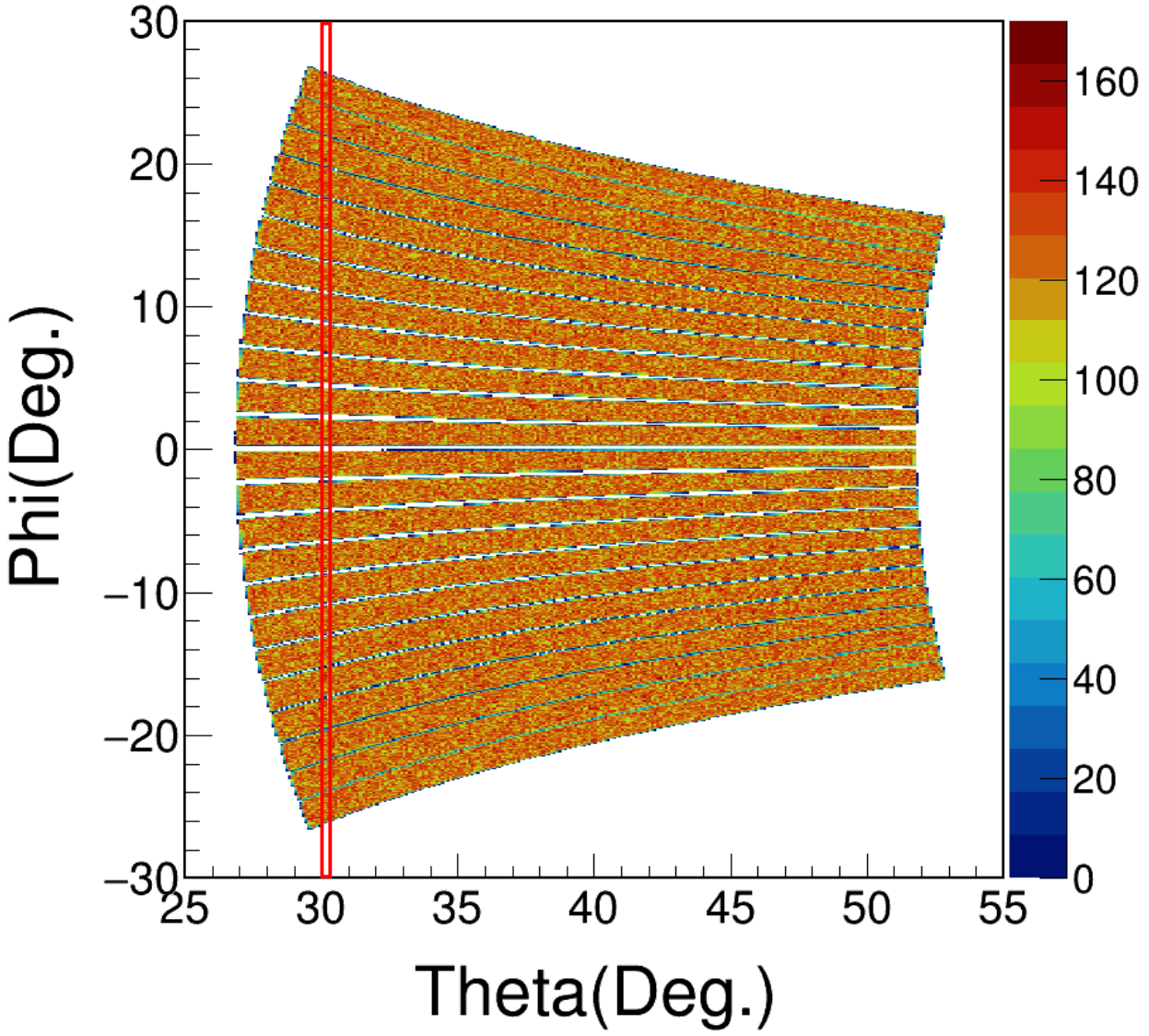

Figure 3.15: Hit distribution pattern in Φ-Θ plane for NWB using Geant4 simulation. In simulation, the LANA is placed in the same position as measured by laser measurements [14] in experiments. Then particles are simulated to emit from target uniformly in Φ-Θ plane. We can see that for different Θ, LANA's coverage in azimuthal direction is different resulting in a geometric efficiency difference. The red window is 0.2 ° wide binned at $\Theta = 30°$.

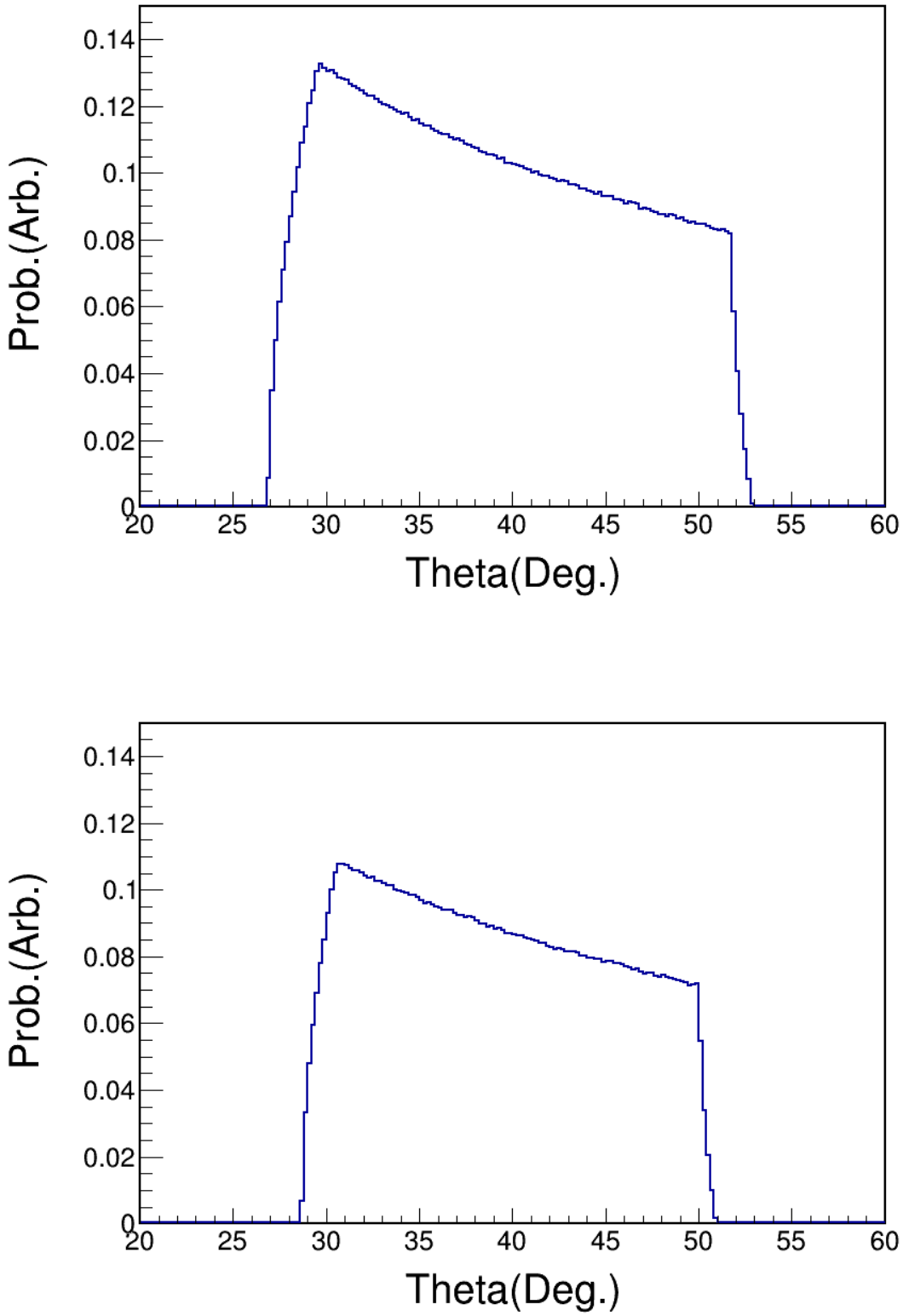

Figure 3.16: LANA fractional azimuthal coverage f_Φ for front (NWB, top panel) and back (NWA, bottom panel) wall.

Figure 3.17: A shadow bar used in experiments for background neutron scattering efficiency correction. Picture is adopted from Ref. [15].

If we want to use $\frac{dM}{dE_k d\Omega}$, then it is $\frac{dM}{dE_k d\Omega} = \frac{dM_{measured}}{dE_k d\Theta d\Phi sin(\Theta) f_\Phi(\Theta)}$.

3.2.4 Background Scattering Efficiency

Inevitably, there are much materials around the target including the floor and the LANA which can potentially scatter neutrons and protons emitted from target. Figure 3.18 shows the structure of aluminum floor under vacuum chamber. For neutrons that have experienced scattering before hitting LANA (indirect neutron), the determination of their ToF is invalid, resulting in incorrect kinetic energy and position information. Those indirect neutrons contribute a certain portion in the neutron spectrum we measure with LANA. We need to determine the fraction of background scattering neutrons in the neutron spectrum and has to be corrected accordingly.

To determine the neutron background i.e. neutrons that do not come directly from beam induced reactions in the target, we block some areas of LANA and then compare the number of neutrons detected in blocked and unblocked areas of LANA. Four 30-cm-long brass shadow bars are used to block about 2% of NWB detection area. They are placed at about 1.7 m

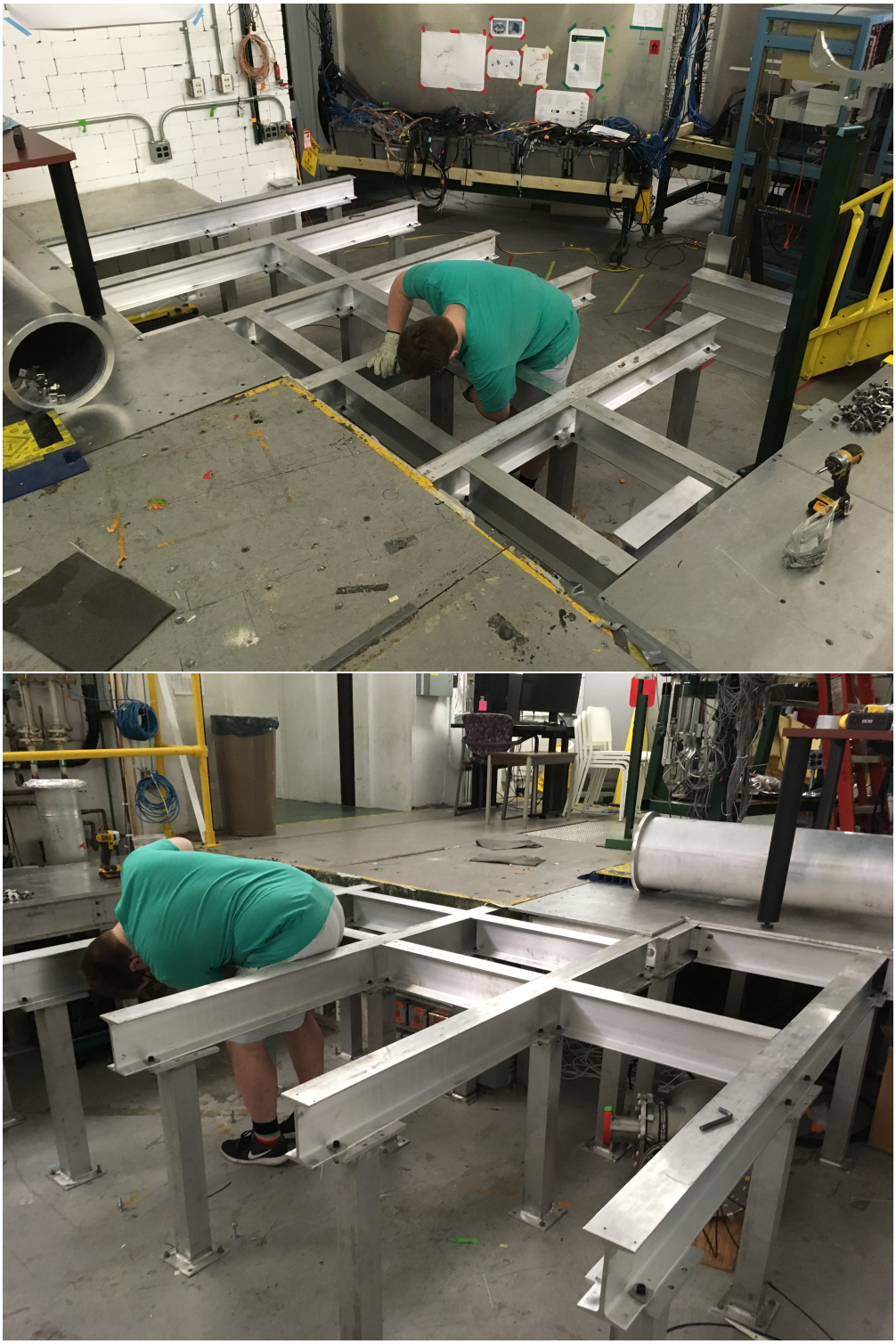

Figure 3.18: NSCL staff is removing part of aluminum floor in S2 vault for leaving space in order to nest the LANA. Above S2 vault's concrete floor, an aluminum layer of floor was built on which vacuum chamber sits.

from the target outside aluminum vacuum chamber. Figure 3.17 shows one of the shadow bars used in the experiments. Figure 3.19 shows the neutron hit distribution of NWB in lab Θ-Φ coordinates with 4 shadow bars installed. Red indicating area being hit by neutron more frequently than orange, yellow and blue. Areas labelled with A, B, C, D have less counts due to blocking of the shadow bars. Certain portions along LANA bar #8 and #16 are fully shadowed by shadow bars. The top left plot in figure 3.20 is a neutron hit position distribution plot of NWB bar #16 with the position range which is shadowed by shadow bar B. The red line in this plot indicates a fit function using the following form:

$$(1 + 0.5 * erf(-\frac{x - x_0}{\sqrt{2}\sigma_0}) + 0.5 * erf(\frac{x - x_1}{\sqrt{2}\sigma_1})) * a + b + c * x \tag{3.14}$$

where $(1 + 0.5 * erf(-\frac{x-x_0}{\sqrt{2}\sigma_0}) + 0.5 * erf(\frac{x-x_1}{\sqrt{2}\sigma_1})$ part shows the area between x_0 and x_1 is shadowed with associated standard deviation σ_0 and σ_1 coming from the LANA position resolution. The values of σ_0 and σ_1 are very similar. The rest of the term in Equation 3.14 indicates the general hit count drop when the X position is smaller (Θ is defined to be zero at the beam line). To get the fraction of background scattering, we scale the form in Equation 3.14 by:

$$\frac{(1 + 0.5 * erf(-\frac{x-x_0}{\sqrt{2}\sigma_0}) + 0.5 * erf(\frac{x-x_1}{\sqrt{2}\sigma_1})) * a + b + c * x}{a + b + c * x} \tag{3.15}$$

The right two plots in Figure 3.20 display the fit function after scaling. At the lowest Y value, the fraction of background scattering is 0.26 for shadow bar B and D area. Same analysis is also applied to shadow bar A and C area as shown in figure 3.21, the fractions of background scattering are found to be 0.27 and 0.29 for A and C respectively. The fitting uncertainty for this method is less than 1%. The slightly higher background from the A C is probably related to their polar angular positions. More neutrons are emitted in the forward

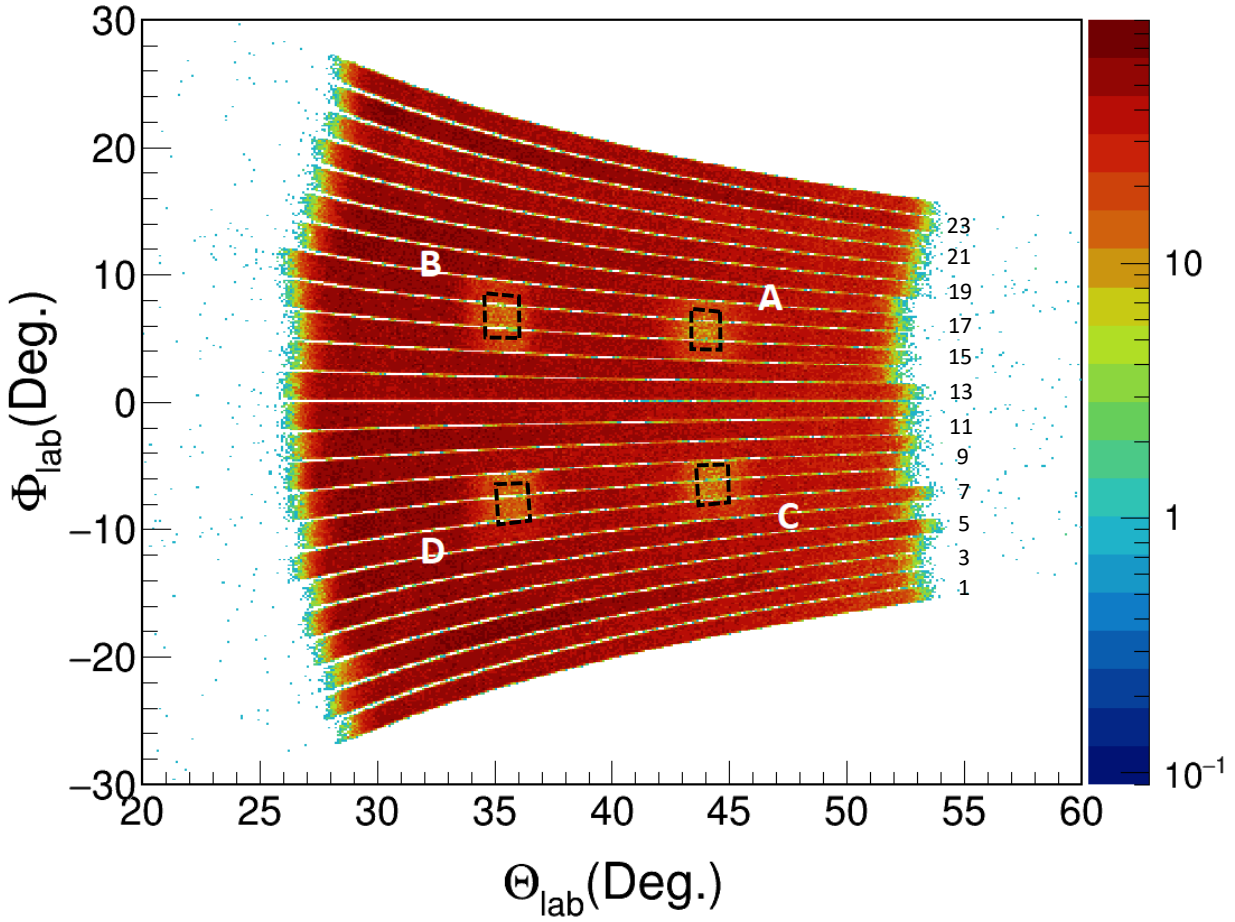

Figure 3.19: The front LANA's (NWB) neutron hit pattern with 4 shadow bar installed in Φ_{lab}-Θ_{lab} coordinates. 4 square areas with less counts of hits corresponds to 4 shadow bars labelled with A, B, C, D as shown. NWB bars are labelled from #1 to #25 corresponding to from the bottom bar to the top bar.Shadow bar A and B fully cover NWB bar #16 and shadow bar C and D fully cover NWB bar #8. The reaction system for this plot is $^{48}Ca +^{124} Sn$ at $E/A = 56\, MeV$.

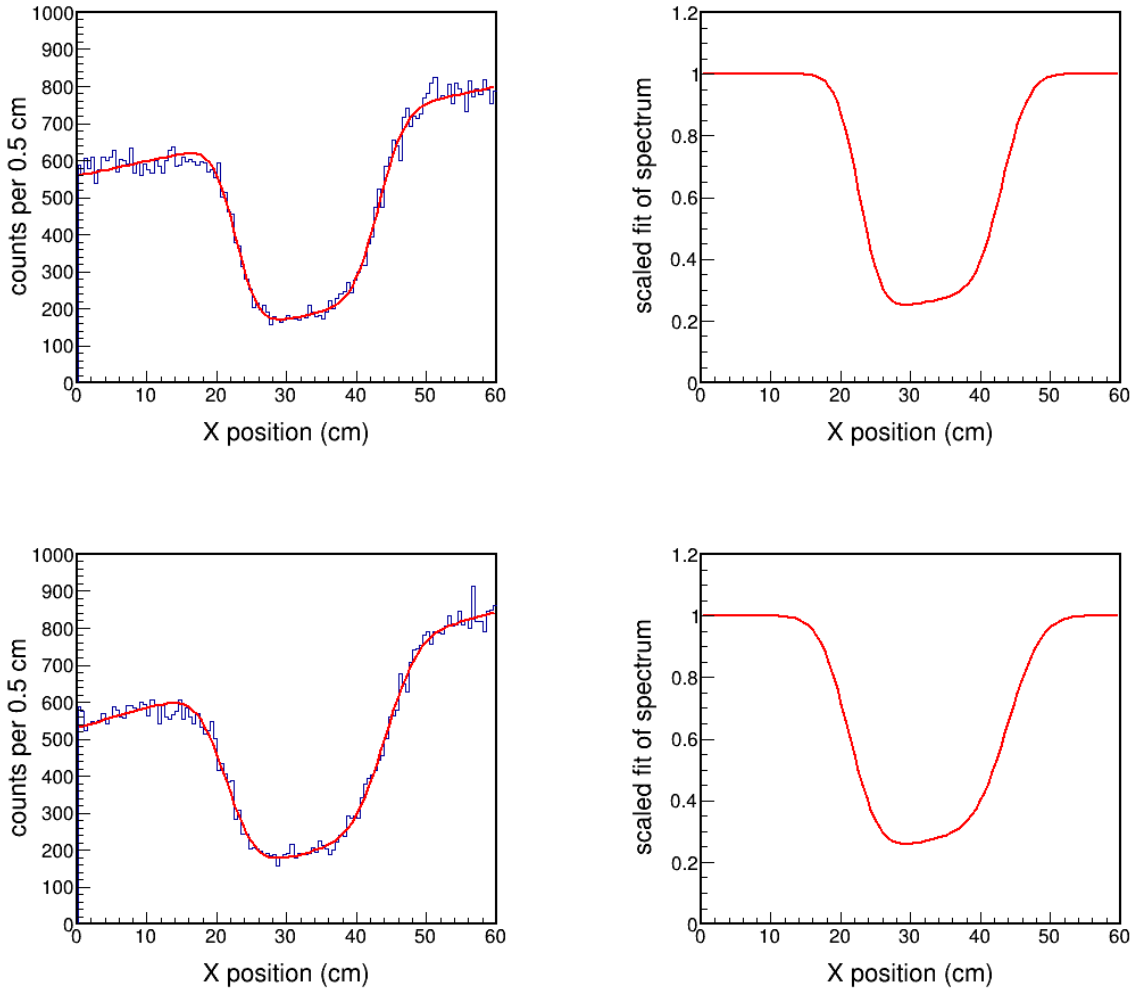

Figure 3.20: (left panels) Neutron hit position spectrum corresponding to shadow bar B (top) and D (bottom). Red lines indicates the fitted functions. (right panels) Scaled fitted functions indicating the background scattering neutron fraction. The lowest points' Y values are both 0.26. The light output threshold is set to 5 MeVee for all 4 plots here.

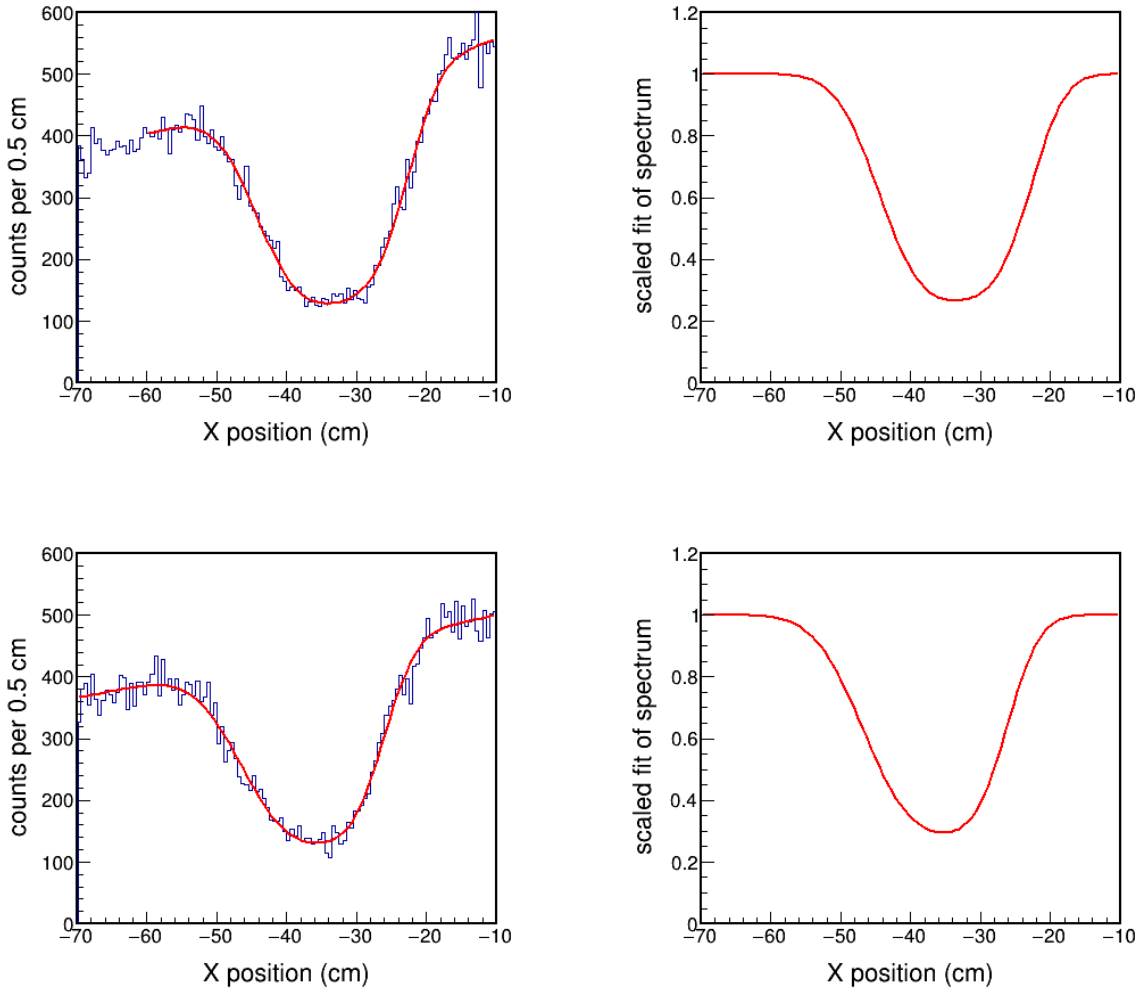

Figure 3.21: (left panels) Neutron hit position spectrum corresponding to shadow bar A (top) and C (bottom). Red lines indicates the fitted functions. (right panels) Scaled fitted functions indicating the background scattering neutron fraction. The lowest points' Y values are 0.27 and 0.29 for A and C respectively. The light output threshold is set to 5 MeVee for all 4 plots here.

angles resulting in higher signal to backgound.

3.3 Charged-Particle Veto Wall Pulse Height Calibration

Charged-Particle Veto Wall (VW) provides critical information to identify and veto charged-particle signals from neutron spectrum measured by LANA. Fig. 3.22 displays 2D plots of NWB light output versus normalized ToF. In the bottom panel of Fig. 3.22, the charged-particle events are vetoed from the spectrum after requiring there is no hit in VW and the top panel has no such requirement. Clearly there are charged-particle contamination lines over neutron spectrum in the top panel. The parabola edge of neutron spectrum is caused by the fact that the maximum light output a neutron could produce is proportional to the kinetic energy of neutron and thus the square of its velocity in non-relativistic case. And neutron velocity is inversely proportional to its ToF. For both plots in Fig. 3.22, most gamma events are filtered out by PPSD described in Ref. [16].

We calibrate the QDC pulse heights of 20 VW bars (only VW bars from #3 to #22 are needed to provide complete coverage of LANA) such that when a charged-particle with certain energy passes through any of 20 VW bars, we will have same QDC pulse height channel value. One way to do this is to use radioactive sources such as ^{60}Co and ^{137}Cs so that the QDC channels of Compton edge of the gamma spectra from several decay channels of ^{60}Co and ^{137}Cs can be calibrated to one value among 20 VW bars. This method is used during setup. It is time-consuming considering moving radioactive sources all over the VW and waiting for adequate statistics to identify Compton edges. Here we use the data taken from experiments with beams to calibrate the QDC pulse height of VW efficiently.

The calibration procedure is based on the fact that a certain charged-particle (for exam-

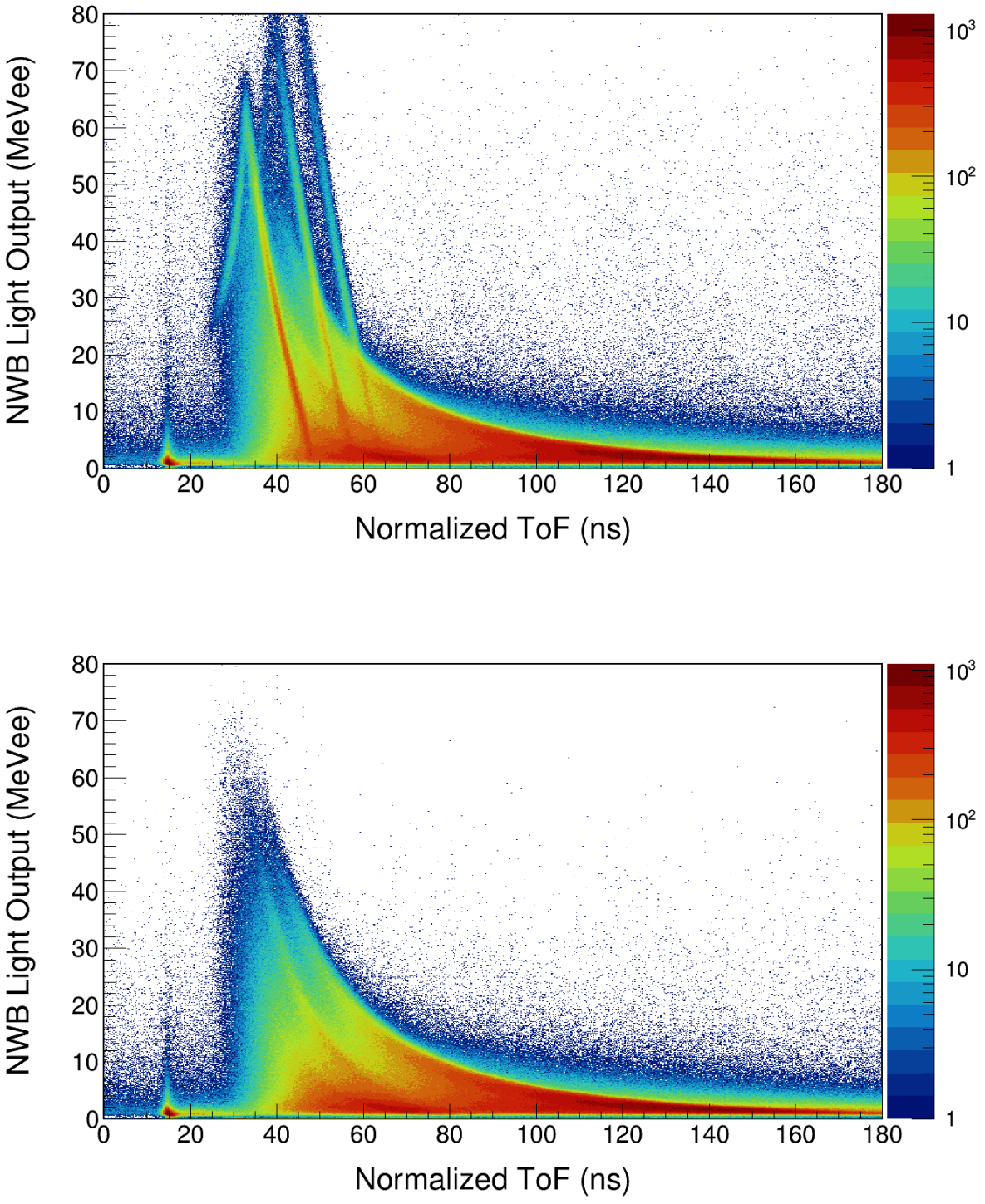

Figure 3.22: Light output versus ToF 2D spectrum from front LANA (NWB). The top panel is the spectrum without using any VW information. The bottom panel is the same spectrum but with the condition that VW should not be triggered. We can clearly see that by requiring no hit in VW, the charged-particle events (those slanted lines in the top panel) are removed completely while keeping the rest of the spectrum undisturbed.

ple, proton) at a fixed energy should produce the same light output in any VW bar when traversing it. We select protons with certain energy and check the VW QDC pulse height of all bars when these protons passing through them. Fig. 3.23 is a 2D Light output versus ToF plot from NWB gated on the events that must have VW triggered. We can see proton, deuteron and triton lines from left to right. By choosing a small window (blue window) on the proton line as shown in Fig. 3.23, we can select protons with ToF in range $[41.5, 43.5]$ ns, corresponding to $[58.6, 65.0]$ MeV in energy or $[10.16, 10.7]$ cm/ns in velocity.

Based on $LISE^{++}$ calculation [104], these protons should deposit 11.7 ± 0.7 MeV in 1-cm-thick BC-200 scintillator every time. Selecting on these events, then we plot the VW geometric mean value $\sqrt{Q_{top} * Q_{bottom}}$ for every bar as shown in the top panel of Fig. 3.24 where Q_{top} and Q_{bottom} are QDC values for top and bottom PMT. Due to PMTs' different gains, different VW bars have different geometric mean value although protons deposited about same energy in every bar. By assigning every bar one coefficient α such that $GM_{calibrated} = \alpha * GM_{raw}$, we calibrate all VW bars' geometric mean to be the same for those proton events, as shown in the bottom panel of Fig. 3.24.

Similar to what we do in Chapter 3.2.1.4, we can also investigate the geometric mean position dependence of VW bars. For a certain VW bar, we can check its geometric mean versus position 2D plot for events sitting in the blue window of Fig. 3.23 as shown in Fig. 3.25. Comparing Fig. 3.25 to the top panel of Fig. 3.8, we can see that the geometric mean of VW bar is much less dependent of VW bar's Y position, varying within 5% over the length of the bar.

Fig. 3.26 is the ΔE-E plot for VW and NWB. The Y-axis is VW calibrated geometric mean and the X-axis is NWB's light output. The three slanted charged-particle lines are protons, deuterons and tritons, from bottom to top, respectively. Because the proton line

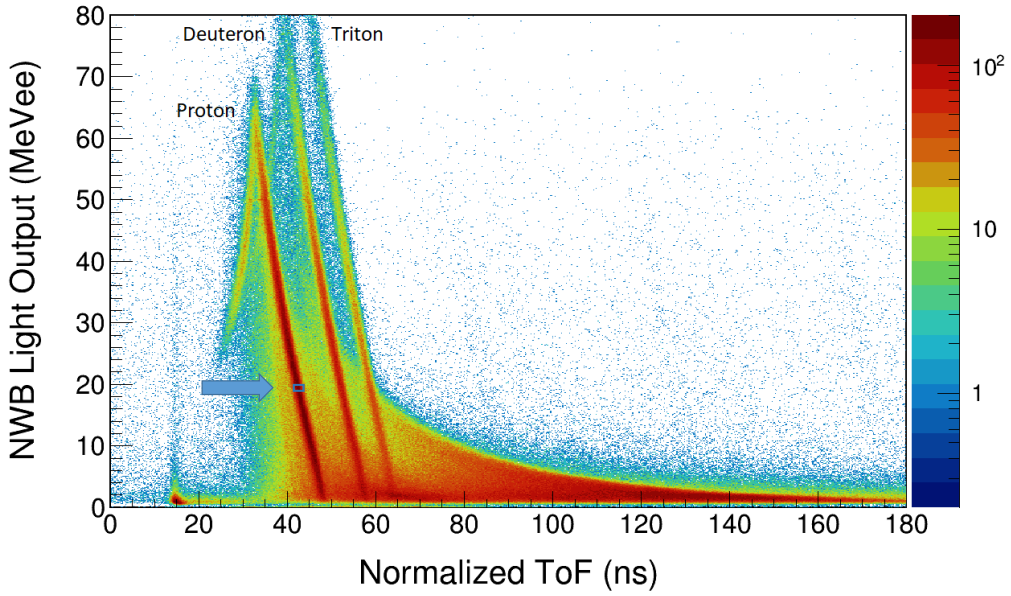

Figure 3.23: Light output versus ToF 2D spectrum from front LANA (NWB) gated on the events that must have VW triggered. The blue window (around 20 MeVee on Proton line) gating on proton line selects the events where a proton's normalized ToF is in range $[41.5, 43.5]$ ns and its light output is in range $[19.5, 20.0]$ MeVee.

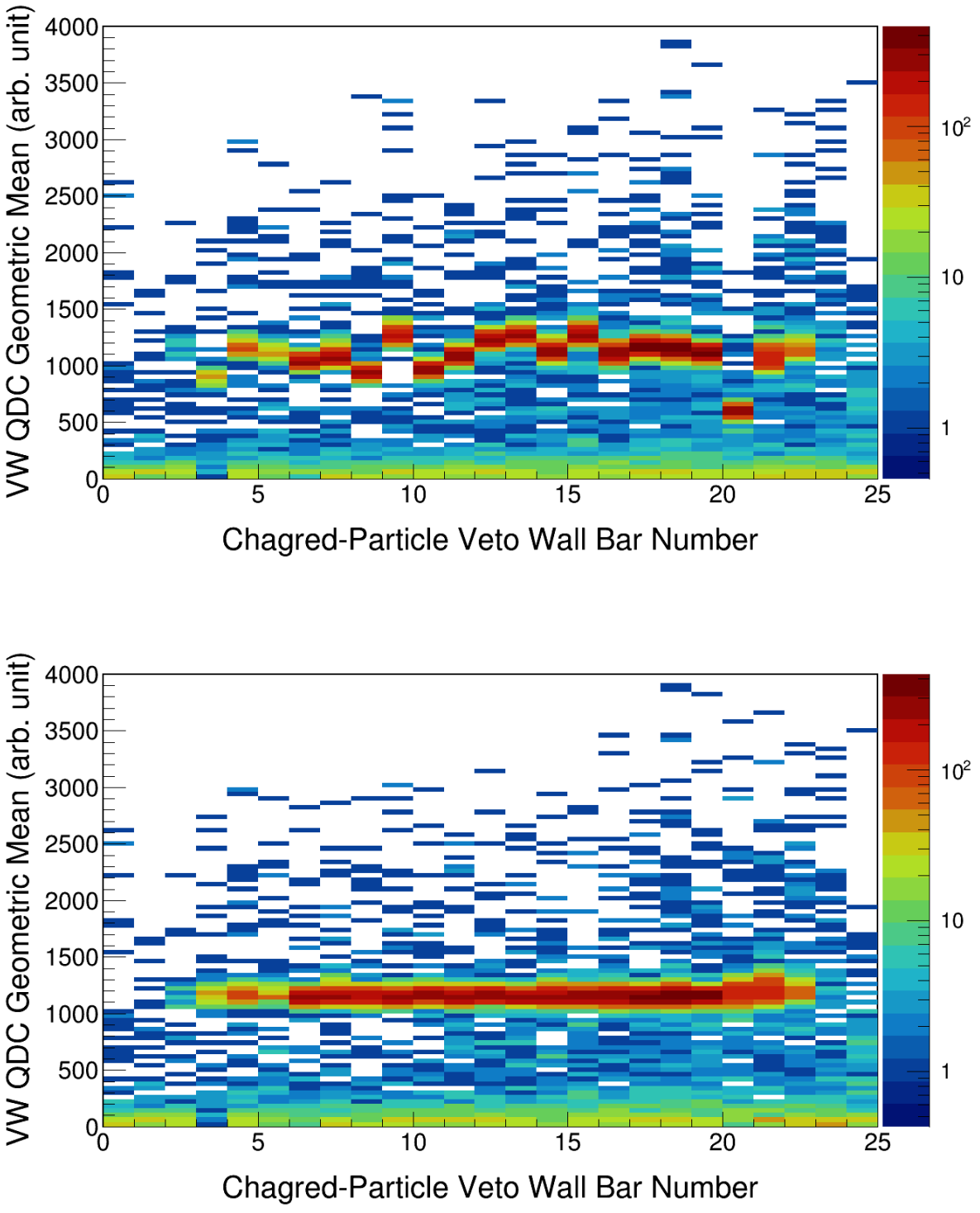

Figure 3.24: VW Geometric Mean $\sqrt{Q_{top} * Q_{bottom}}$ versus VW bar number 2D plot. The top panel is before geometric mean calibration and the bottom panel is after geometric mean calibration using $GM_{calibrated} = \alpha * GM_{raw}$.

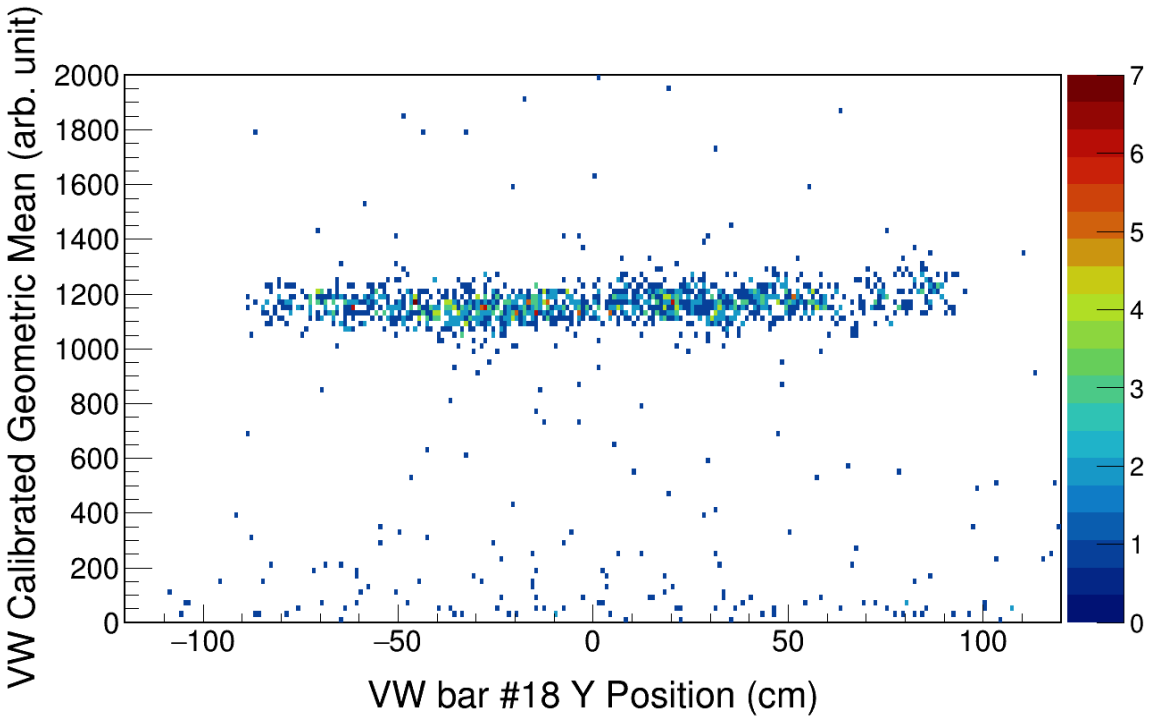

Figure 3.25: VW bar #18's geometric mean versus Y position 2D plot for events sitting in the blue window of Fig. 3.23. We can see that it is almost flat comparing to the top panel of Fig. 3.8.

vanishes at around (X = 25,Y = 500) in Fig. 3.26, any charged-particle that punches through VW and leaves a signal in LANA should deposit a signal in VW greater than 500 ADC channels as VW calibrated geometric mean. We can set 200 ADC channels as the threshold to indicate whether VW is triggered by any charged-particle and take events below threshold as noise. Bars need to be well calibrated among VW and LANA in order to see charged-particle lines as shown in Fig. 3.26.

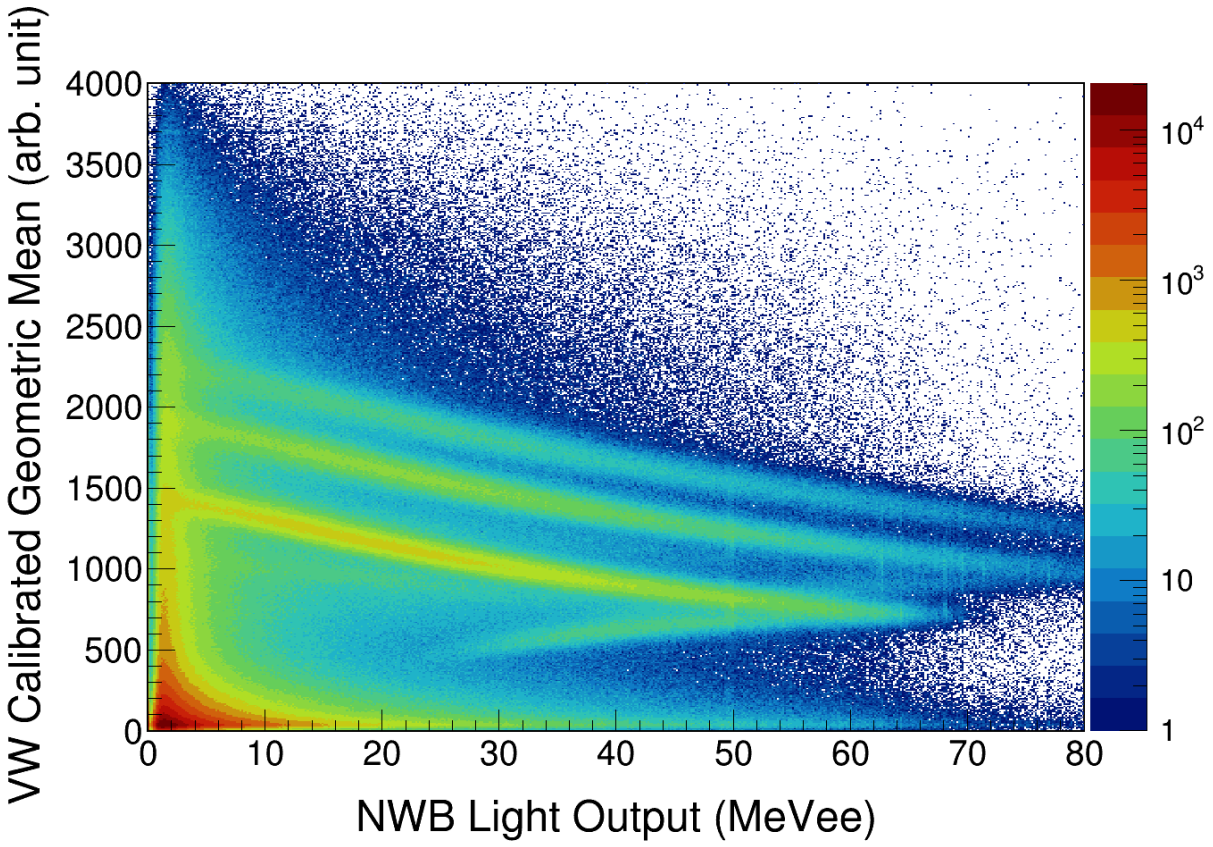

Figure 3.26: VW calibrated geometric mean versus NWB light output 2D plot.

Chapter 4

Performance of LANA

4.1 Neutron/γ Pulse Shape Discrimination

Pulse shape discrimination (PSD) technique is commonly used to distinguish whether a light signal from the scintillator originates from neutron or gamma ray. This technique is based on the characteristic of certain organic scintillators which have longer scintillation decay time for proton (induced by neutrons) and charged particles emitted from nucleus-nucleus collisions than for gamma rays [105, 106]. For scintillator molecules in configurations where π-electron spins are fully paired, singlet states (S_1) are created. Configurations with unpaired π-electron spins give rise to triplet states (T_1) where 3 spin component values are allowed: $m_s = -1, 0, 1$. The de-excitation of excited S_1 results in the short decay component while the kinetic of the excited T_1 diffusion process and the following triplet-triplet interaction and annihilation including $T_1 + T_1 \rightarrow S_0 + S_1$ is responsible for the long decay component. High concentration of triplets states are created from the short range of energetic protons knocked out by neutrons. Therefore, compared to gamma rays, neutron contributes a larger proportion in the long decay component of scintillation pulses. Figure 4.1 shows a schematic drawing of the different pulse shapes for neutron and gamma ray signals.

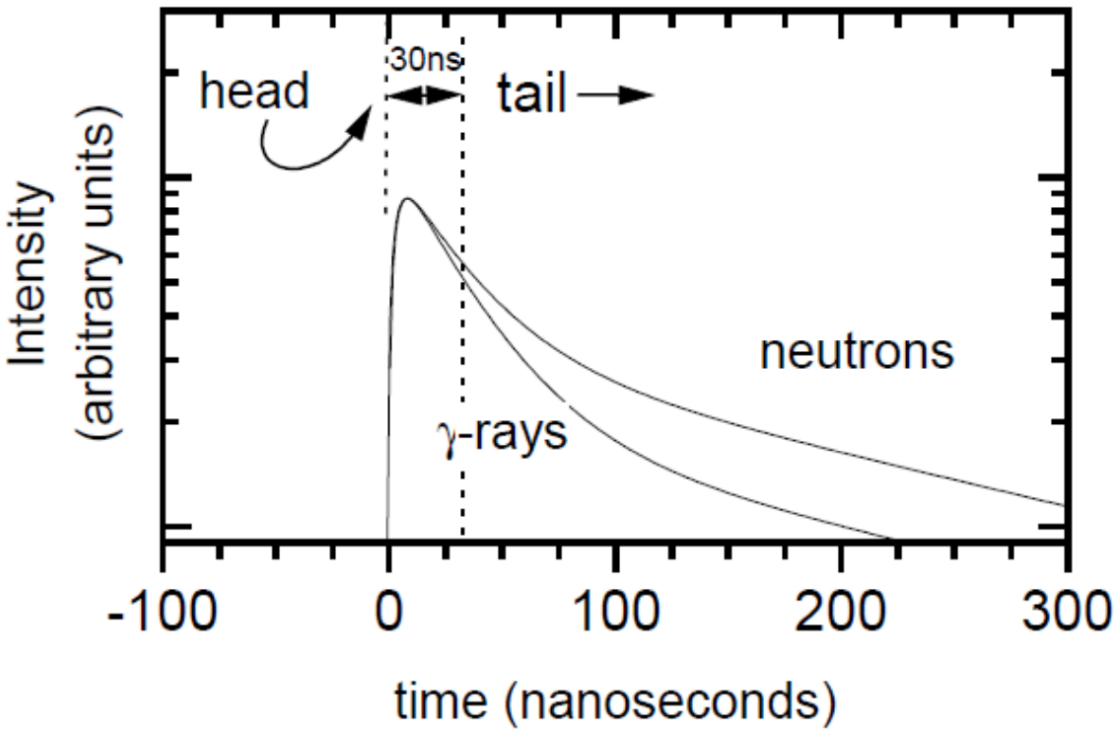

Figure 4.1: A schematic of different pulse shapes for neutron and gamma rays. The peak heights are normalized to be the same. This picture is adopted from Ref. [9].

4.1.1 Traditional PSD & VPSD comparison

In experiments, we applied two different gate widths to obtain the total (340 ns) and fast component (first 30 ns) of light signals from LANA. Details about the electronics that we used to enable PSD is described in Section 2.3. To minimize the position dependence of the light output and to utilize signals from both the left and right PMTs in each neutron bar, the geometric mean ($\sqrt{Q_{left} * Q_{right}}$) of the total and fast are constructed. Figure 4.2 shows a 2d plot with the GM of total component of light signals versus GM of fast component. Two groups representing gamma rays and neutrons can be seen. In the past [9] we calculate a value called "flattened geometric mean" to replace geometric mean in figure 4.2 so that the splitting between gamma rays and neutrons is enhanced, as shown in figure 4.3. Flattened geometric mean is calculated from the difference between total GM and scaled fast GM:

$$GM_{Flattened} = GM - constant * GM_{Fast} \tag{4.1}$$

While traditional PSD analysis method cancels out some of the position dependence effect due to the signal attenuation when the light travels along a scintillator bar to the PMT, this method compromises the signal resolution as it includes the light signal from scintillator bar's far end which can worsen the resolution because the light transmission through the scintillator to the far phototube reduces the signal size and consequently, the photon statistics for that signal. An innovative method called "Value-assigned Pulse Shape Discrimination" (VPSD) [16] which takes full advantage of the light signal that comes from one end with good resolution. The VSPD is mainly developed by Fanurs Teh, a graduate student in our group. For illustration, we use data obtained from Americium-Beryllium neutron source as described in section 3.2.1. In this method, instead of combining the information from left and right PMTs of a bar at early stage by calculating geometric mean, we retain the left

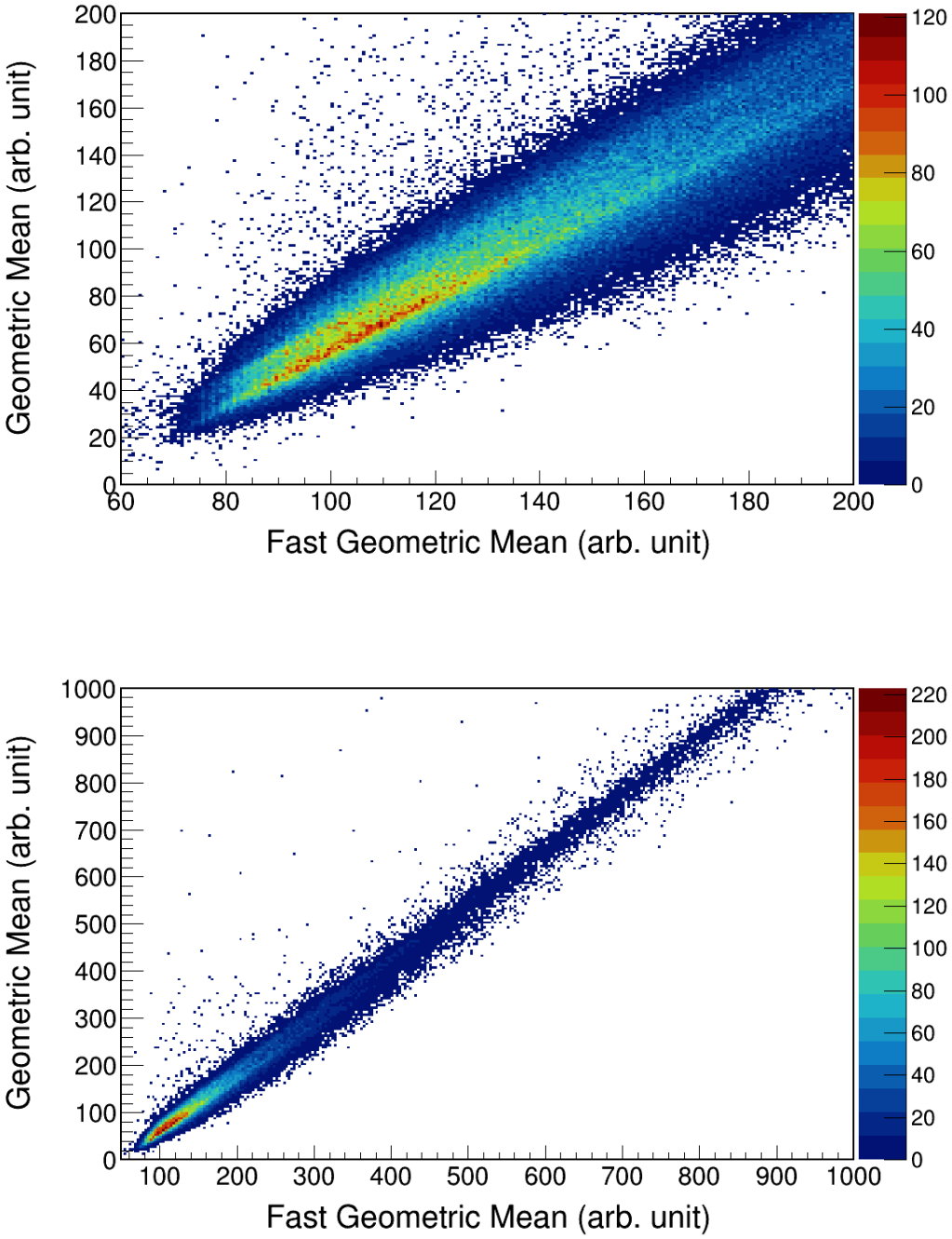

Figure 4.2: LANA geometric mean versus fast geometric mean 2D plots from a typical bar. The data was taken with ^{48}Ca+^{124}Sn at $E/A = 56$ MeV reaction. The top panel focuses on the low value end, which is a zoomed-in version of the bottom panel. We can barely see two lines in each panel, which are gamma rays (top) and neutrons (bottom).

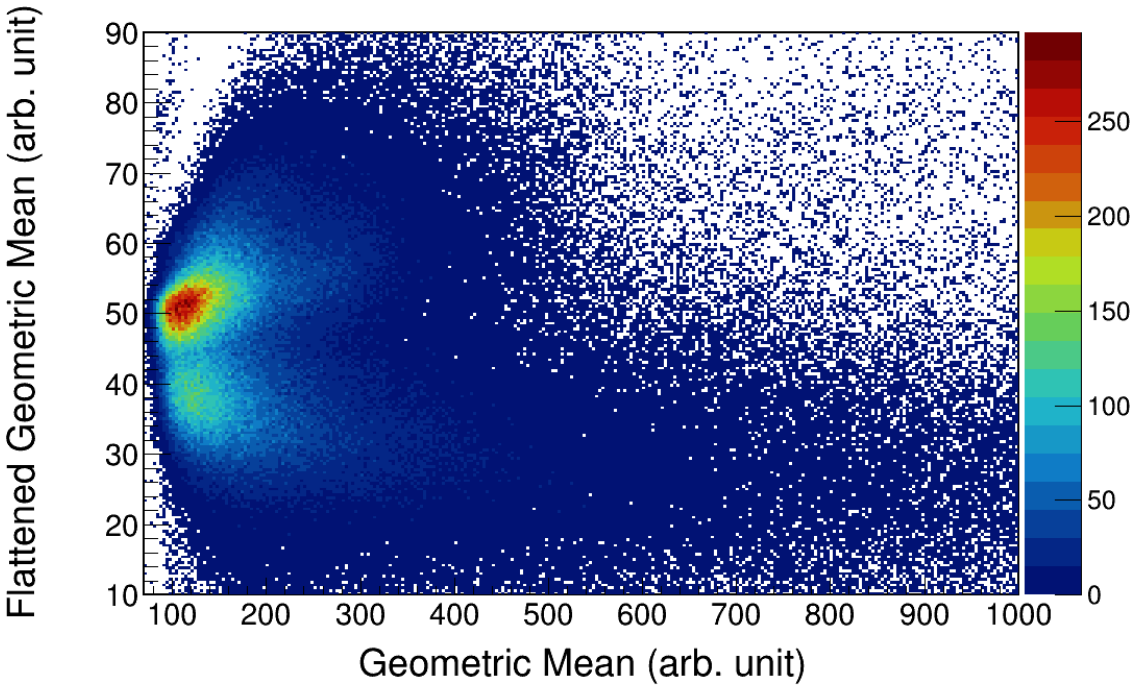

Figure 4.3: LANA flattened geometric mean versus fast geometric mean 2D plot. The data is the same as shown in figure 4.2 but the clustering of gamma rays (top) and neutrons (bottom) is much clearer.

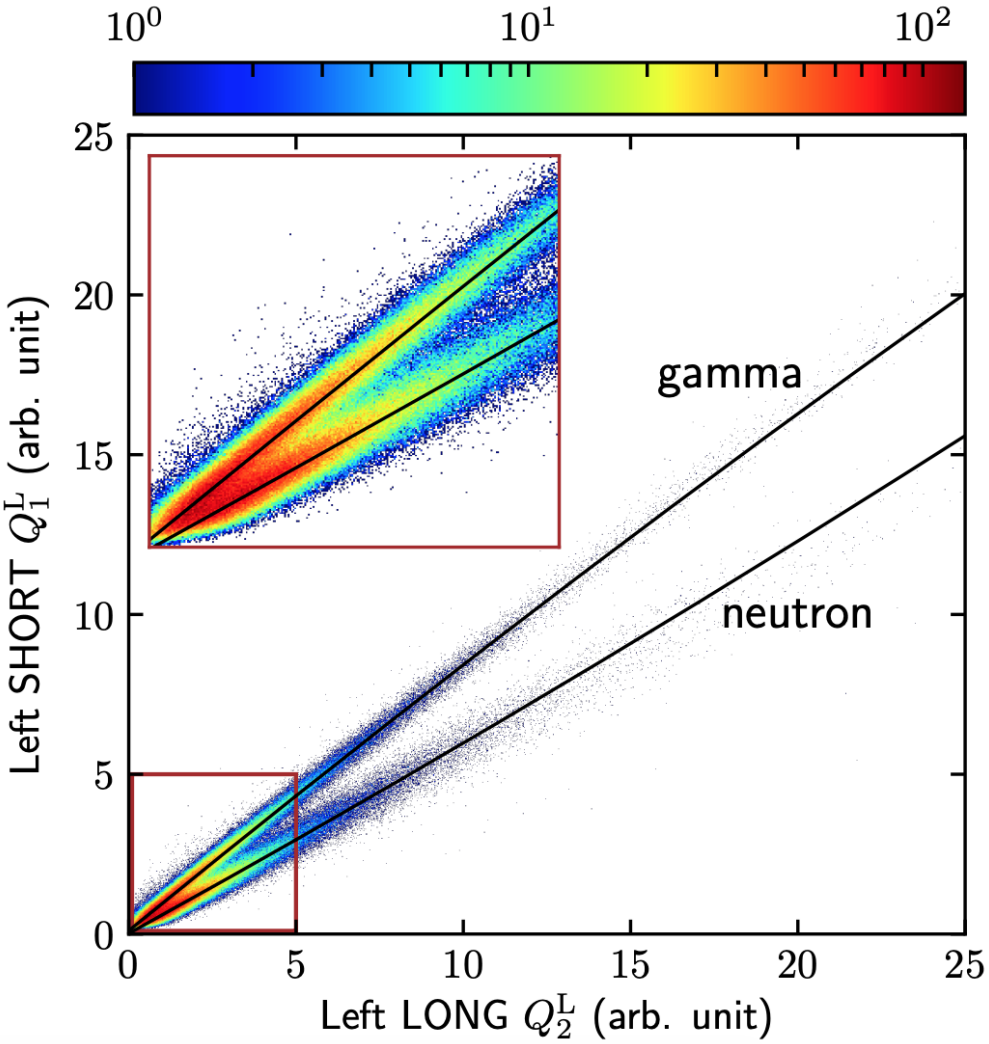

Figure 4.4: A two-dimensional histogram of (Q_{fast}, Q_{total}) from the left end of a LANA bar. The two solid curves are quadratic fits on the gamma ray cluster (top) and neutron cluster (bottom) respectively. Q_{fast} and Q_{total} correspond to SHORT Q and LONG Q in this plot. This picture is taken from Ref. [16].

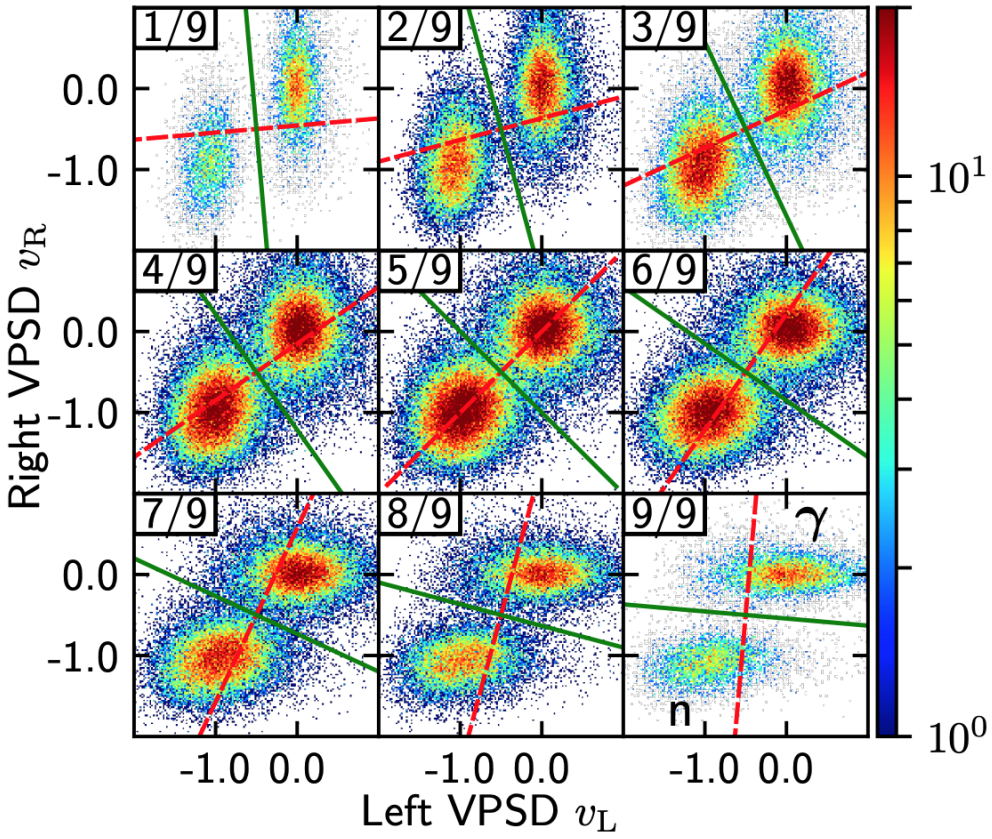

Figure 4.5: 2D $v_{L,R}$ plots for all the nine segments of one LANA bar, with 1/9 representing the leftmost segment and 9/9 representing the rightmost segment. The solid line represents the n/γ separation line, while the dashed line is the line perpendicular to the solid line that pass through (-0.5, -0.5). This picture is taken from Ref. [16].

right information on individual PMT i.e. we analyze the signal to the left and right PMTs separately. Figure 4.4 is an example of such 2D plot for the left end of a LANA bar. Two quadratic functions are fitted along the neutrons and gamma lines over the range of interest in figure 4.4. Then, we assign the value -1 and 0 to the points lying on the neutron and gamma fitted lines respectively. Each pulse is assigned a value according to:

$$v_{L,R}(Q_{fast}, Q_{total}) \equiv \frac{Q_{fast}^{L,R} - q_\gamma(Q_{total}^{L,R})}{q_\gamma(Q_{total}^{L,R}) - q_n(Q_{total}^{L,R})} \tag{4.2}$$

where q_γ and q_n are the fitted quadratic functions for gamma rays and neutrons, respectively. We called his procedure "valued assigned pulse shape discrimination" (VPSD). Note that VPSD does not correct for the position dependence of the neutron light output signal. To examine the position dependence, we plot the VPSD values from the left PMT (v_L) vs. the right PMT (v_R). Figure 4.5 shows the 2D histograms of v_R versus v_L for nine segments along the position of LANA bar. Near the ends of the bar, one can clearly see the separations of neutrons from gammas. To take into account the position resolution, we rotate the plots in figure 4.5 around point $(-0.5, 0.5)$ by position dependent angles such that the green separation lines are all vertical. This allows data from different segments along LANA bar to be plotted cumulatively together while retaining the maximal separation between neutron and γ. To be specific, mathematically, we propose a PSD metric named PPSD-X and PPSD-Y (position-corrected VPSD) that is defined as:

$$\begin{aligned} PPSD\text{-}X(x, v_L, v_R) &= \frac{v_L cos(\theta_{proj}) + v_R sin(\theta_{proj})}{cos(\theta_{proj}) + sin(\theta_{proj})} \\ PPSD\text{-}Y(x, v_L, v_R) &= \frac{-v_L sin(\theta_{proj}) + v_R cos(\theta_{proj})}{cos(\theta_{proj}) + sin(\theta_{proj})} \end{aligned} \tag{4.3}$$

where x is the hit position within range $[-l/2, l/2]$ (l is the scintillator bar length), v_R and v_L are the values calculated in VPSD as described in Equation 4.2. For a certain hit

position x, θ_{proj} is calculated as:

$$\theta_{proj}(x) = \frac{\pi}{2} \cdot \frac{x + l/2}{l} \tag{4.4}$$

This gives $\theta_{proj} = 0$ for $x = -l/2$ and $\theta_{proj} = \frac{\pi}{2}$ for $x = l/2$. The dominators in Equation 4.3 serve to normalize the projected neutron peak to be at $PPSD\text{-}X \equiv 1$. Figure 4.6 compares the PSD results using traditional flattened PSD method(left) and PPSD method (right) for both best (top row) and worst (bottom row) performance bars. The advantage of using the PPSD based on the VPSD method to separate the neutrons from gamma is clear.

The top panel of figure 4.7 shows the well separated neutrons and gamma in PPSD from ^{48}Ca+^{124}Sn at $E/A = 56$ MeV reaction. By projecting the PPSD spectra onto the x-axis, we can get a PSD spectra with two peaks representing neutrons and gammas. Their relative abundance can be obtained using a double Gaussian fit. This improves the resolution near the ends of the bar because you can rely essentially on the near phototube and ignore the far phototube because it is not required to resolve neutrons and gammas. As the separation achieved is quite good, there is little ambiguity in the determination of percentage of gammas which would be misidentified as neutrons if the neutron detector does not have PSD capability as is the case for plastic scintillator bar. For plastic scintillator bars, one can only set a gate to exclude prompt gamma-rays that travel to the bar from the target at the speed of light. Other gamma rays are created by reactions of gammas, neutrons and charged particles that come from the target and react with nuclei in the floor of the vault, for example creating a gamma that hits the LANA device. For ^{48}Ca+^{124}Sn at $E/A = 56$ MeV reaction, the fraction of such gammas that arrive after the prompt peak are shown in figure 4.8 as a function of neutron energy that would be computed from their time of flight. It varies from around 10

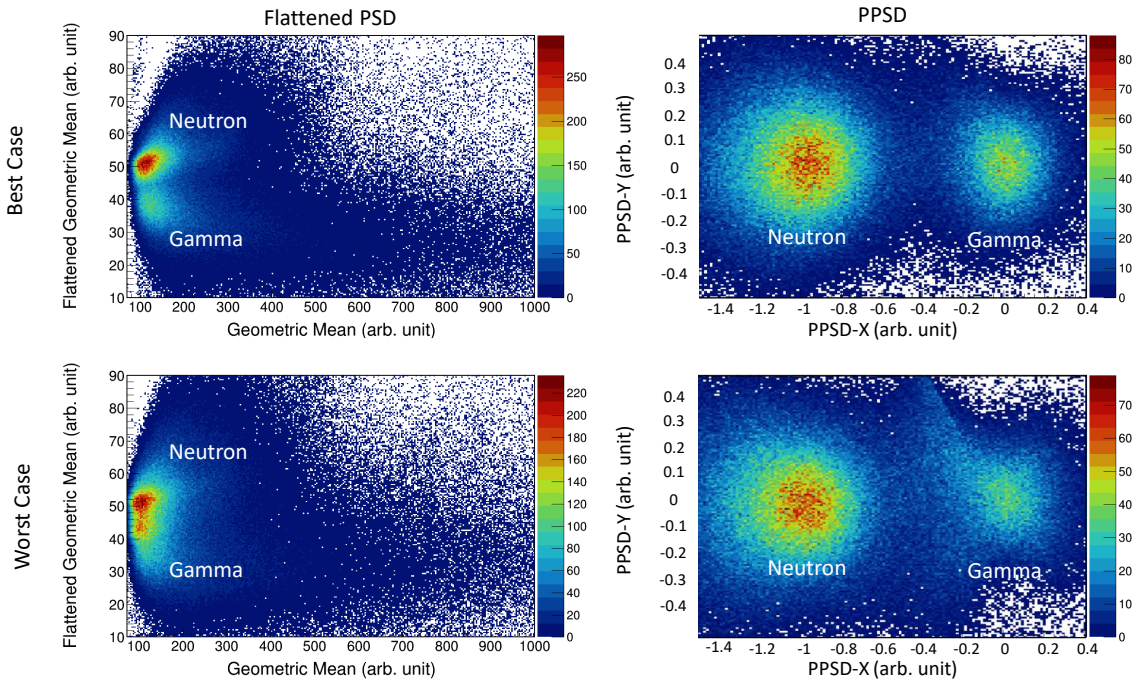

Figure 4.6: PSD results comparisons between traditional flattened PSD method (left column) and VPSD method (right column) for both best (top row) and worst (bottom row) performance bars.

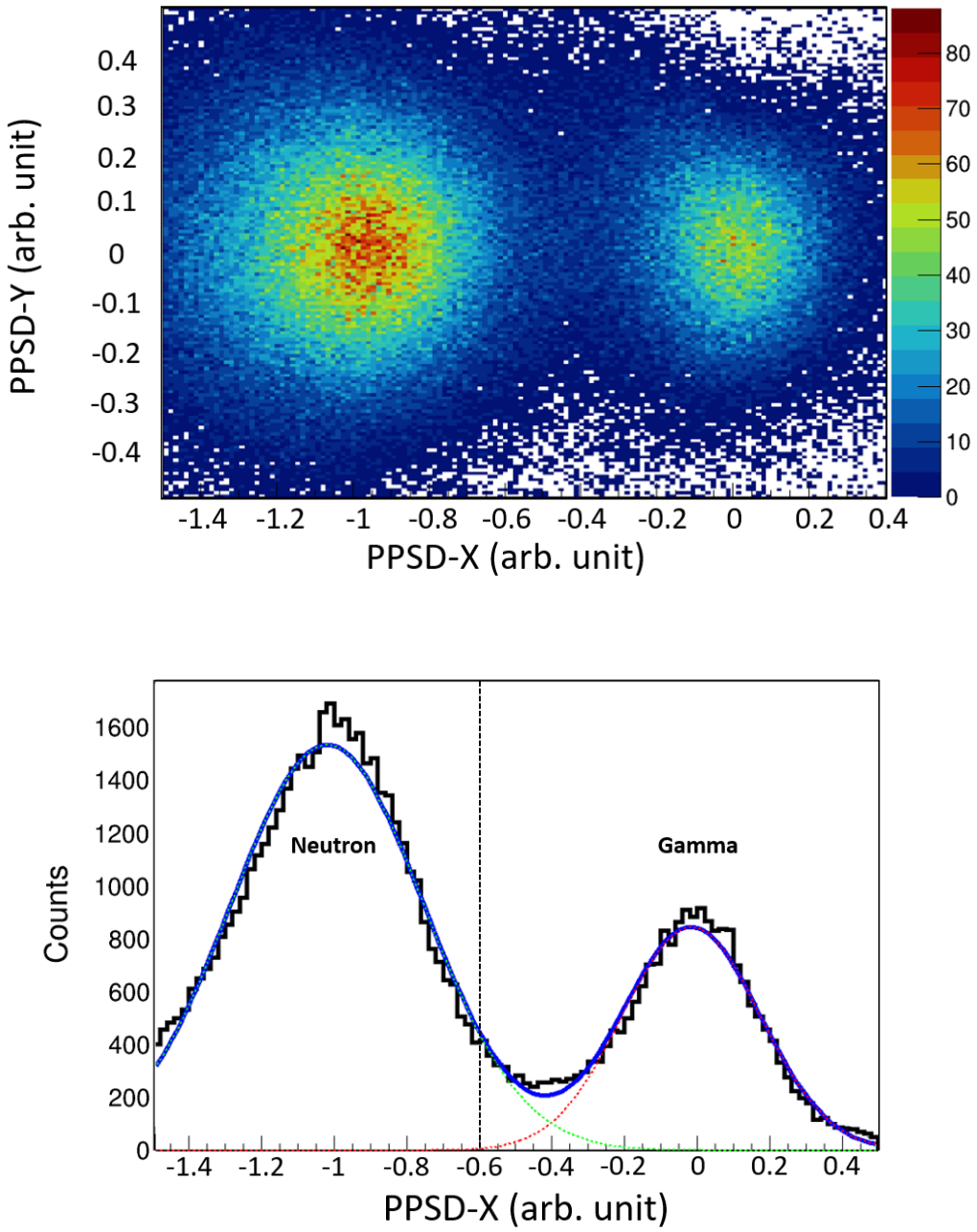

Figure 4.7: (top panel) Neutron/γ pulse shape discrimination obtained by PPSD method. The X and Y axes correspond to v_L and v_R of Figure 7 in Ref. [16], after rotation to match for different segments on LANA bar. The light output threshold is set to 2 MeVee. Gamma rays aggregate in right bubble and neutrons are clustered in left bubble. (bottom panel) 1D projection plot from the plot in top panel. Two Gaussian functions are fitted to γ events peak (red dash line) and neutron events peak (green dash line). The blue solid line represents the sum of two Gaussian functions. Taking events with gate of $PPSD\text{-}X < -0.6$ ensures getting neutrons with nearly no gamma contamination.

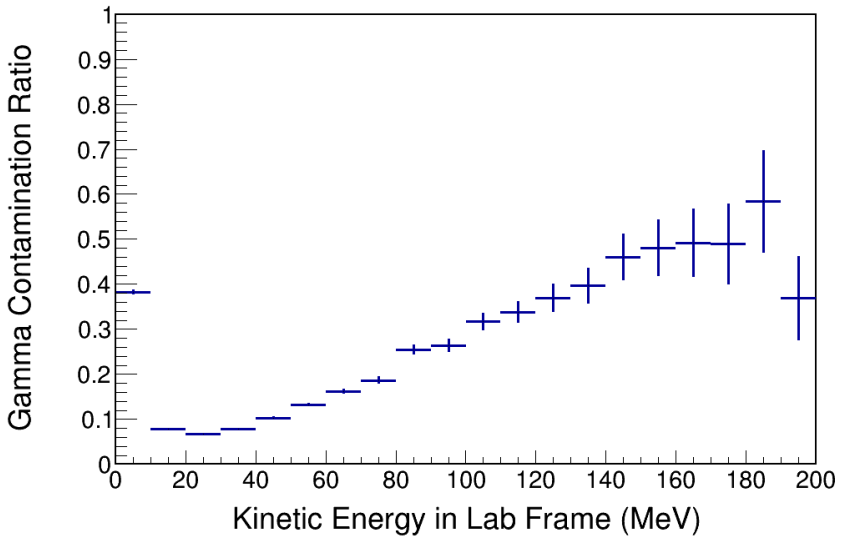

Figure 4.8: Gamma contamination as a function of particle incident energies, if the scintillation material used in this experiment to detect neutron has no PSD capability. The data was taken with ^{48}Ca+^{124}Sn at $E/A = 56$ MeV reaction. The light output threshold is set to 5 MeVee.

percent for 20 MeV neutrons to more than 50 percent for 200 MeV neutrons. For nuclear reaction studies above Fermi energies, where no sharp peaks of neutrons are observed, it is important to retain the ability to resolve gamma and neutrons in the neutron detectors.

4.1.2 PSD efficiency

In previous section, I give a brief summary and comparison of both tradition PSD and VPSD analysis method. While more details of VPSD can be found in Ref. [16], we can further illustrate the superiority of VPSD over traditional method with its application. In the following, based on the results from VPSD method, I will show how to estimate neutron PSD efficiency, gamma contamination and extract the corrected neutron spectrum.

To quantify the gamma ray background in neutron events, we examine the bottom panel of figure 4.7 which contains the 1D vertical projection plot of its top panel. We found that the sum of two Gaussian functions could reproduce the shape pretty well. Based on Gaussian fits, if we take events with "PPSD X<-0.6" condition, we will obtain 94.2 percent efficiency of the neutrons with gamma contamination less than 1 percent. The efficiency corrected neutron TOF spectrum using this method is shown in black dash line in figure 4.9. This is one way to get the neutron spectrum.

There is another way to obtain the neutron spectrum to verify the above estimation. To do this, we generated a series of TOF 1D spectra as shown in the bottom panel of figure 4.10. This time, we set a gate at "$PPSD\text{-}X = -0.1$" as indicated in the top panel of figure 4.10. We take all events with "$PPSD\text{-}X > -0.1$" as pure gamma ray events and the rest with "$PPSD\text{-}X < -0.1$" as neutron with gamma contamination. The time of flight spectrum for pure gamma events with "$PPSD\text{-}X > -0.1$" are shown in the bottom panel of figure 4.10. ToF spectrum for "$PPSD\text{-}X < -0.1$" corresponding to neutron with gamma

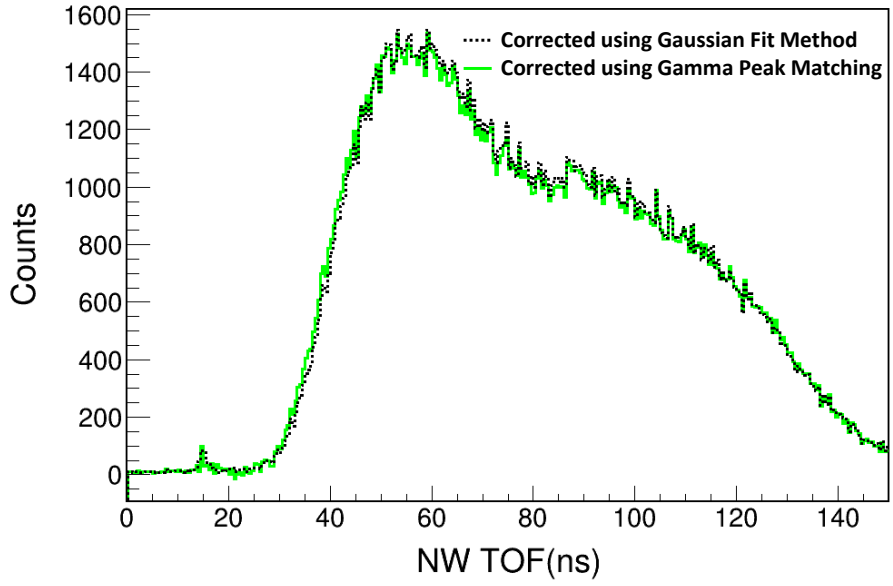

Figure 4.9: Pure neutron TOF spectra obtained by two correction methods. Black dash line is calculated based on the Gaussian fits in figure 4.7: Take neutron events with "PPSD X>0.6" and then correct for 94.2% efficiency. Green solid line is the same green line shown in figure 4.10 using gamma peak matching method.

contamination is drawn as the green line in figure 4.10. Red line representing pure gamma ray events has a strong prompt gamma peak at around 16 ns. It also has a long tail from reactions on surrounding material that looks like neutrons. While the majority of blue line includes ALL of the neutron events, there are also gamma ray events from the tail of the gamma ray Gaussian, and the (n,gamma) background reactions mixed in. To get rid of the gamma contamination in blue line, we first assume that the gamma events mixed in blue line have the same ToF spectrum shape as pure gamma ray ToF spectrum in red with some scaling constant. Then we use the prompt gamma peaks in red and blue lines as an indicator of this scaling constant. We can calculate this scaling constant by doing division between the prompt gamma peak count heights of red and blue lines. In the case of figure 4.10, the scaling constant is 0.449. To get pure neutron spectrum after correction, we multiply the pure Gamma Tof spectrum by 0.449 and subtract it from neutron ToF with gamma contamination. The neutron ToF after correction is shown in green line both in figure 4.10 and figure 4.9.

Figure 4.9 compares the pure neutron ToF spectra after correction using two methods described above. The black dots are the pure neutron spectrum rescaled by 1/0.94 as discussed in the first procedure. The green line is what we did second by taking everything in the neutron PSD peak and subtracting the gamma contamination. These two spectra agree with each other within 2 percent. The gamma contamination rate in these spectra is within 1 percent based on previous analysis and indeed we can see a small prompt gamma peak at around 16 ns. Because the speed of neutrons emitted from our experiments can not be close to the speed of light, particles with TOF below 20 ns will be eliminated from neutron events in further neutron energy and momentum spectra analysis. This will make the gamma contamination in neutron spectra much smaller than 1 percent.

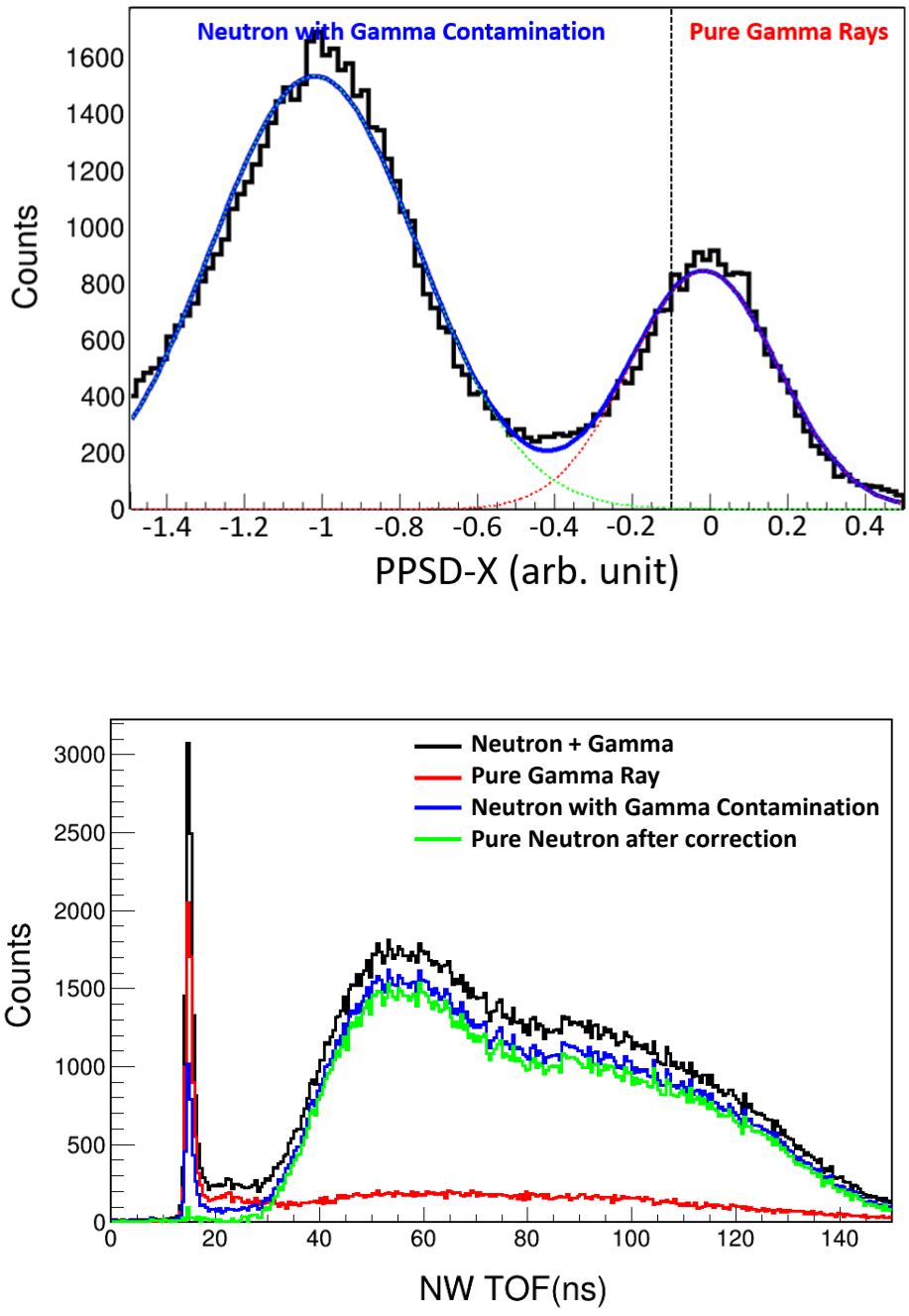

Figure 4.10: (top panel) Same as the bottom panel in figure 4.7 but set a gate at "$PPSD\text{-}X = -0.1$" to get pure gamma ray events and neutron with gamma contamination. (bottom panel) ToF spectra with different gate conditions. Spectrum of neutron and gamma where charged-particles are vetoed is drawn in black. Red line shows pure gamma ray events with condition "$PPSD\text{-}X > -0.1$" while blue line shows neutron with gamma contamination with condition "$PPSD\text{-}X < -0.1$". Green line displays the ToF spectra after correction using gamma peak matching method, which is the same line drawn also in green in figure 4.9.

4.2 Neutron Light Output Comparison with SCINFUL-QMD

To successfully detect a neutron in LANA, the neutron needs to interact with the scintillating material and deposit enough that it is above a threshold value for which electronics can generate a trigger signal reliably. Because neutrons are neutral, a neutron interacts with the detector via the strong interaction making the detection probability significantly less than unity (<10 percent) for a thickness of 6.35 cm of the LANA scintillator bars. There are two different ways that one can define the efficiency; therefore it is easy to become confused about what one is discussing. This is because the efficiency can be defined in a way that it includes the solid angle and it can also be defined in a way that it includes only the probability that a neutron interacts deposits energy above the threshold value if it goes through the solid angle subtended by the detector.

For the following discussion, we take the second definition and define the neutron detection efficiency as the probability of detecting a neutron that traverses a detector with a particular incoming kinetic energy. Determining this efficiency is indispensable in extracting the absolute magnitude and shape of neutron energy spectrum. It depends on the thickness of the scintillator and of the electronic threshold applied to the scintillator signal that must be overcome by the induced signal.

The NE213 scintillator in LANA is a hydrocarbon fluid containing both protons (hydrogen nuclei) and carbon atoms in it. Neutrons below 10 MeV are typically scattered elastically by these protons and subsequent interactions of the recoiling protons with the scintillators create the photons to be detected. Neutrons can be detected also through inelastic, fusion, or breakup nuclear reactions on the carbon nuclei in the scintillator fluid. This becomes increasingly important for more energetic neutrons. When a neutron reacts with a carbon

nucleus, one or more charged particles can thereby be generated. Besides considering various reaction channels between incident neutrons and scintillation material, we need to take how the scintillator geometry influences the induced signal into account because events can occur that involve recoiled protons escaping the detector without depositing all of their energies. The resulting signal may be above the detection threshold and be counted or below the detection threshold and be lost. Developing a simulation codes that can handle all these processes is a complex task because some of the reaction channels are not well described in current detector simulations and it is an ongoing project for one of our Korean collaborators. To obtain preliminary neutron spectra in this thesis, we used a code called SCINFUL-QMD [5] developed by Satoh et al. at the Japan Atomic Energy Agency. This code is one of the more complete simulation in modeling neutron reaction processes in the detector and reproducing experimental data. Using SCINFUL-QMD, we are able to determine the neutron detection efficiency in LANA. To validate the code, we compare the simulated neutron light response function to our experimental data.

SCINFUL-QMD code simulates the NE-213 scintillator light response of neutrons from 0.1 MeV to 3 GeV using the Monte Carlo technique. Above 150 MeV, multiparticle breakup is an important decay mode and to model this, SCINFUL-QMD incorporates a quantum molecular dynamics model (QMD) and the statistical decay model (SDM). The QMD semi-classically describes the behavior of nucleons and mesons during nucleus collision and thus simulates the process for these more complicated nucleon reactions. The current version of SCINFUL-QMD code restricts the configuration of detector to be in the shape of a cylinder with radius and height as input variables. We adjust the input variables including cylinder's height, radius similar to the geometry of our unit cell of 6.35cm and 7.62cm as depth and height, and light attenuation factor is then adjusted by comparing the simulated light

response to the data.

Figures 4.11 , 4.12 and 4.13 show a more comprehensive neutron light response comparison between experimental data and SCINFUL-QMD simulation using neutron light output versus incident neutron energy. Figure 4.14 shows a two dimensional representation of the light output response as a continuous function of the neutron energy E_n. In general, we find that SCINFUL-QMD reproduced the shapes of light output spectra pretty well for different incident neutron energies. This is consistent with the study by Coupland et al. [9]. For that work, accuracy in the shape of the spectrum was extremely important as the veto wall was not available then to eliminate charged particle contamination in the neutron walls. So it was necessary to know details of the light output response in the regions of neutron energy and light output where the charged particle contamination was absent.

The efficiency for detecting a neutron of a given energy in a given scintillator bar corresponds to the probability of getting a signal in the neutron wall that is over the experimental threshold when a neutron of that energy hits that bar in the neutron wall. To calculate the efficiency for a neutron at certain energy,we need to choose the threshold in the geometric mean signal in the bar the neutron signal must exceed. During the experiment, we set a hardware threshold on the bars so that a signal of 3 MeVee would be detected everywhere on the bar. Here, we raise that threshold to 5 MeVee. To calculate the efficiency for detection of an energy deposition above this threshold, we integrate the properly normalized light output spectra e.g. figures 4.11 , 4.12 and 4.13, over all light output values higher than that threshold value. Each of these light output curves gives the efficiency at one energy. Doing this at one MeV intervals in the incident neutron energy provides the neutron efficiency as a function of energy.

There are discrepancies between the observed light output in Figures 4.11, 4.12 and

4.13 and the simulation. These discrepancies between data and simulation may be caused by the significant limitations of changing the detector geometries and moving the position of neutron source in SCINFUL-QMD code. It is also hard to reproduce the light attenuation, scattering and collection processes in simulation. Ongoing efforts are being taken to embed SCINFUL-QMD into GEANT4 platform to make the code more versatile and more accurate for our purposes. The final neutron spectra will be obtained after that effort is complete. Nevertheless, we now examine the neutron spectra using the present efficiency calculations.

Based on SCINFUL-QMD simulation with a threshold of 5 MeVee, the neutron detection efficiency of LANA for neutrons with energies greater than 25 MeV is calculated as shown in figure 4.15. Low energy neutrons have larger contamination due to scattering from the beam dump and the floor and ceiling of the experimental vault and we have not studied that contamination extensively. 25 MeV also corresponds to the energy threshold of the charged particle detected in HiRA.

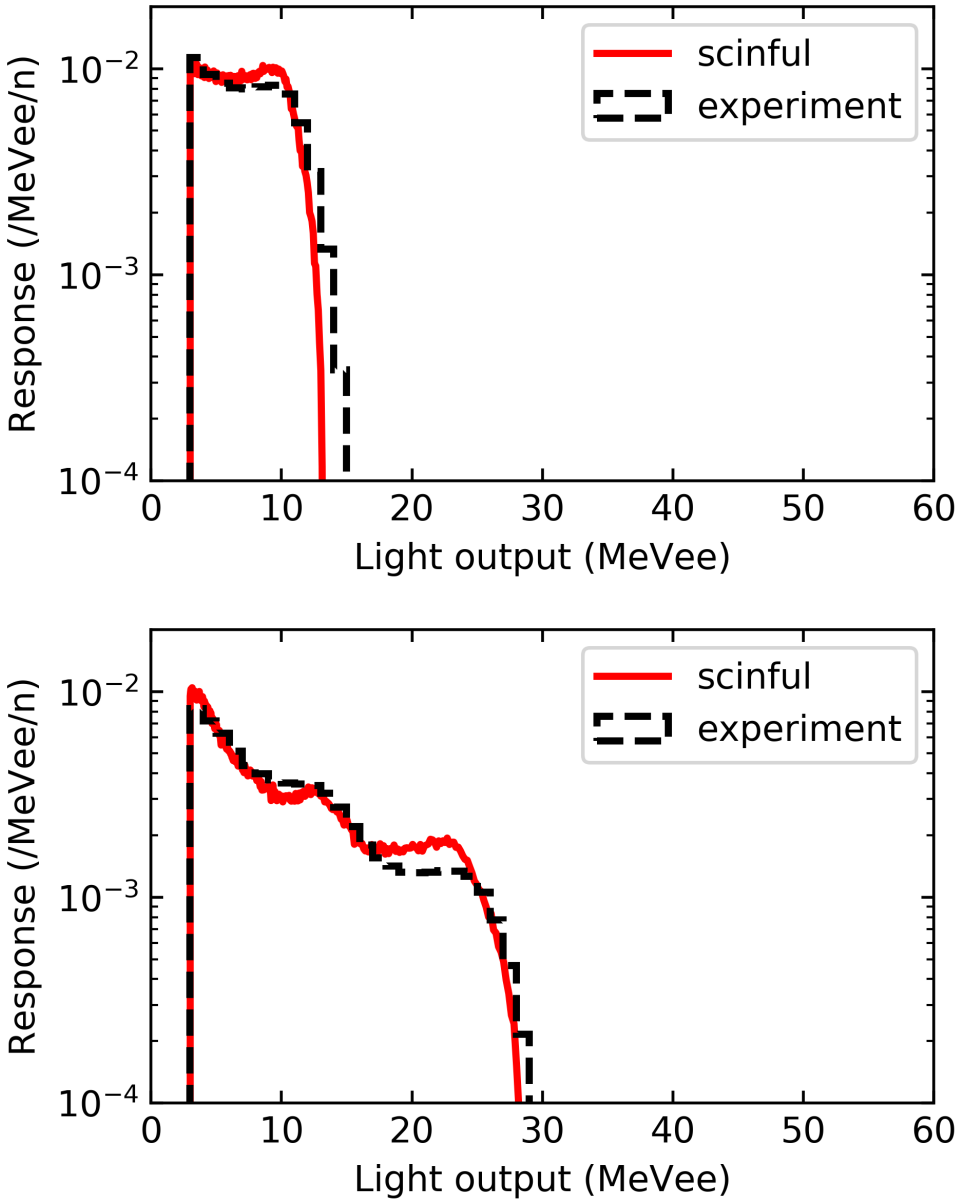

Figure 4.11: Comparison of neutron light output spectra from experiments and SCINFUL-QMD with different incident neutron energies at 20 MeV (top panel) and 40 MeV (bottom panel).

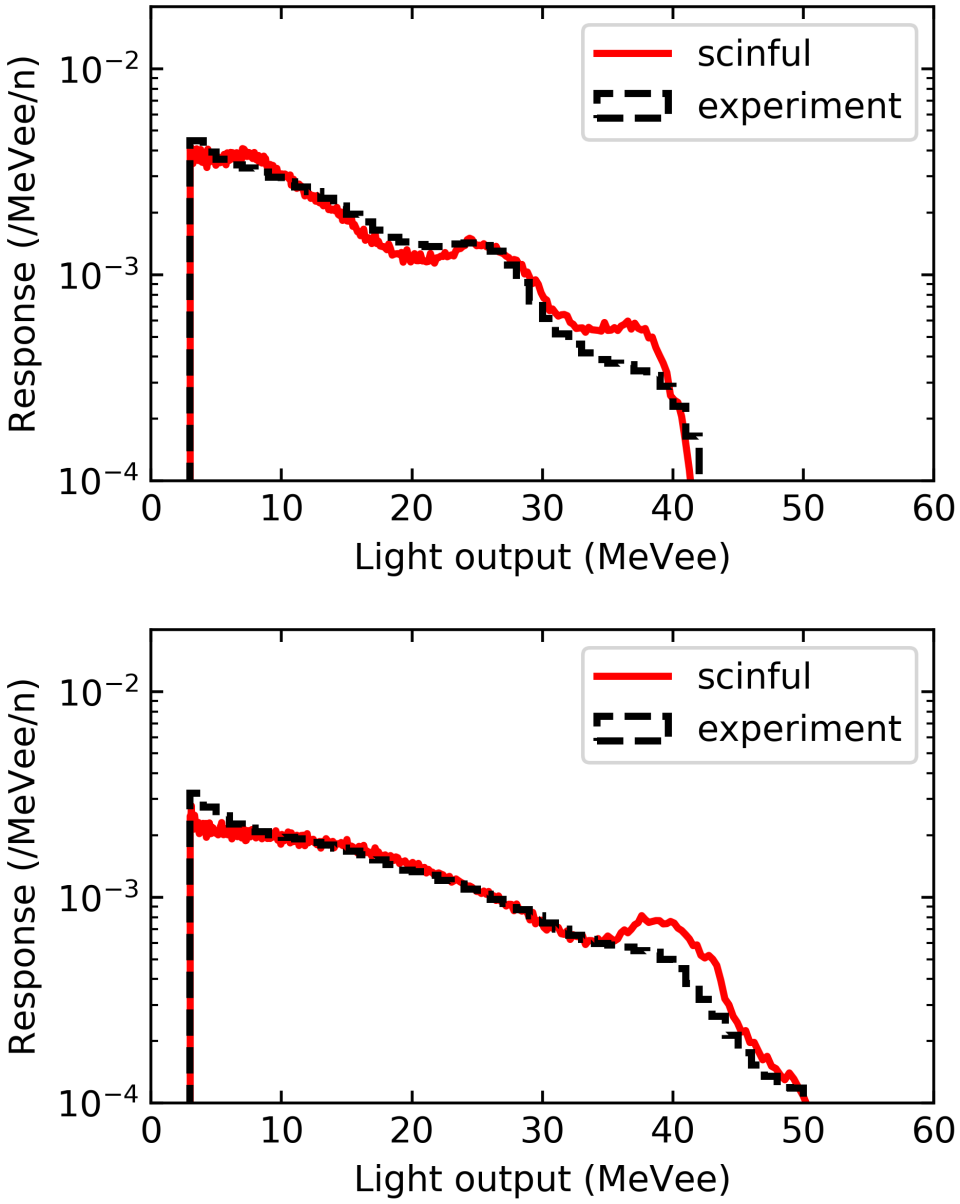

Figure 4.12: Comparison of neutron light output spectra from experiments and SCINFUL-QMD with different incident neutron energies at 60 MeV (top panel) and 80 MeV (bottom panel).

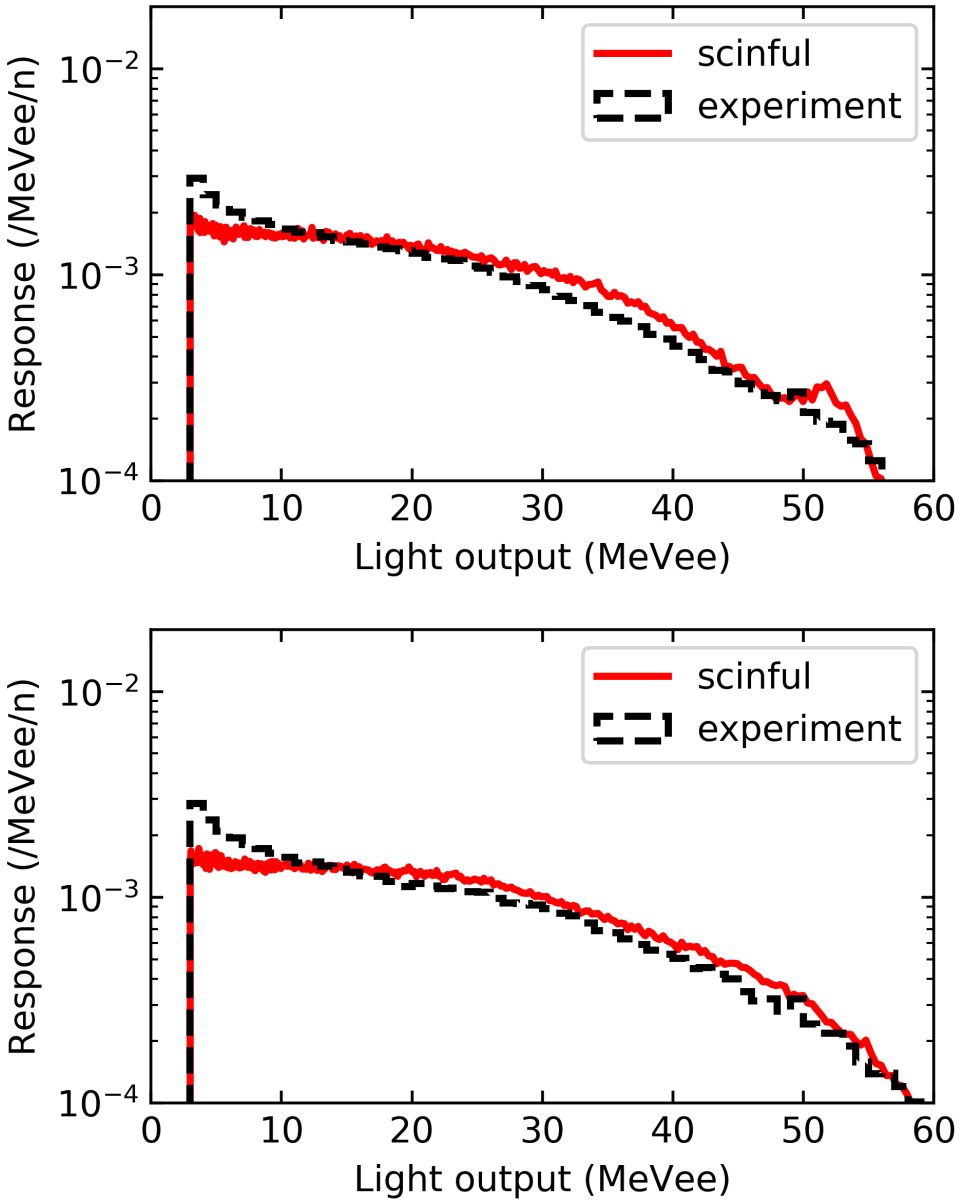

Figure 4.13: Comparison of neutron light output spectra from experiments and SCINFUL-QMD with different incident neutron energies at 100 MeV (top panel) and 120 MeV (bottom panel).

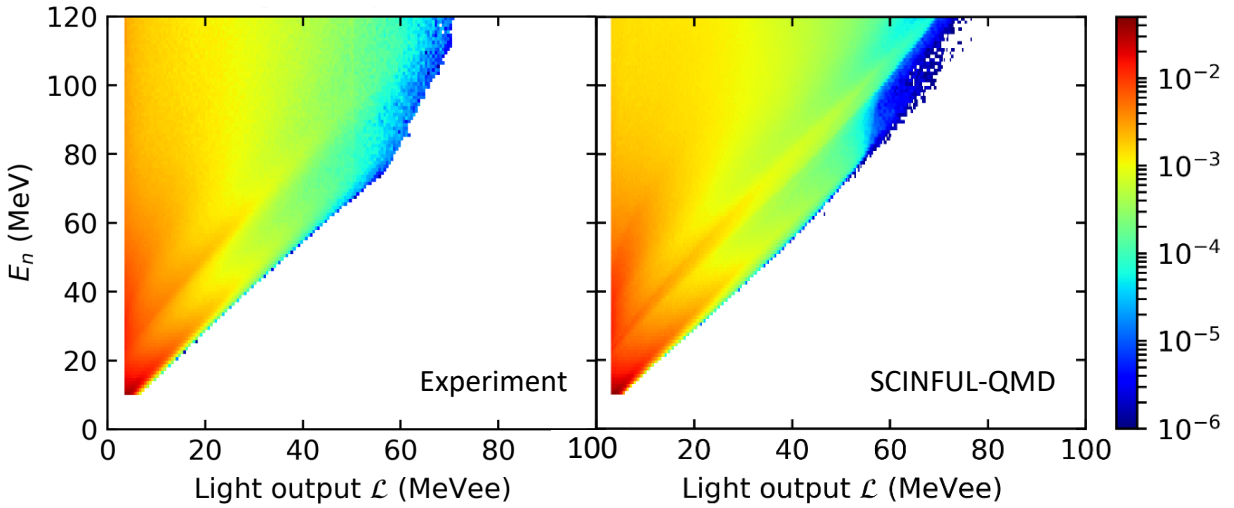

Figure 4.14: Comparison of neutron light output versus incident neutron energy 2D plots from experiment data (left) and SCINFUL-QMD simulation (right).

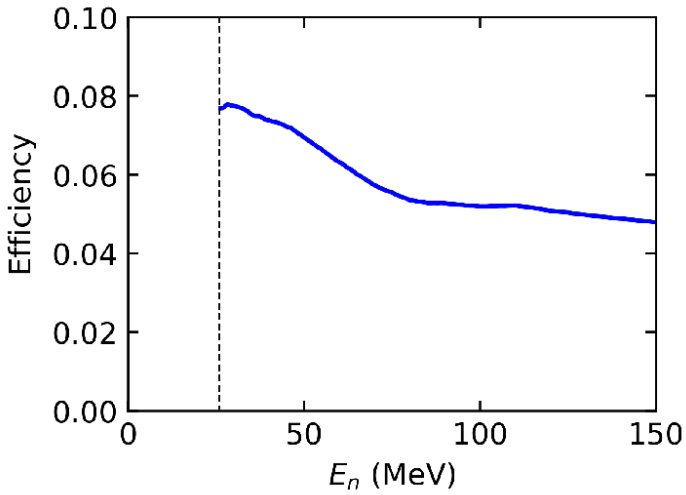

Figure 4.15: The neutron detection efficiency of LANA as a function of neutron incident energy. Detection efficiencies for neutrons with incident energies more than 25 MeV are used.

4.3 Preliminary Neutron Spectrum

We extracted preliminary neutron spectrum from ^{48}Ca+^{64}Ni at $E/A = 140\ MeV$ reaction as shown in figure 4.16. Firstly, when calculating the raw energy spectra of neutron drawn in black, we adopt a light output threshold of 5 MeVee to ensure the whole LANA can detect particle hits uniformly. The majority of gamma contamination comes as prompt gamma so they are filtered out naturally by the time-of-flight gate cut. For gammas that hit the LANA within the time window of neutrons, most of them come from the experiment vault background. Most of them are eliminated by utilizing the neutron/γ discrimination method described in Chapter 4.1. To measure the neutrons from central collisions, a deduced impact parameter gate from [0,0.4) is applied. The red line above the black line in figure 4.16 takes the detection efficiency correction into account by using the SCINFUL simulation results from figure 4.15.

In figure 4.17, neutron spectra with several angular cuts are shown for the same reaction system. The Y-axis is count per bin and the X-axis is neutron energy in MeV in lab frame. A moving source model is applied to extract the following parametrizations of this moving source: apparent temperatures T, velocities V_s, multiplicities N and Coulomb energy E_c. Here, the Coulomb energy is the energy gained by Coulomb repulsion of the exciting proton by the rest of the system. In the context of compound nucleus, that would be called the Coulomb barrier. In this model, the particles are assumed to be emitted isotropically from one moving sources, following Maxwell-Boltzman distribution in source rest frame [107]:

$$\frac{d^2\sigma}{d\Omega dE} = \frac{N}{2(\pi T)^{3/2}}(E - E_c)^{1/2} exp[-(E - E_c)/T] \tag{4.5}$$

To apply this model to neutron energy spectrum measured in lab frame, we need to do

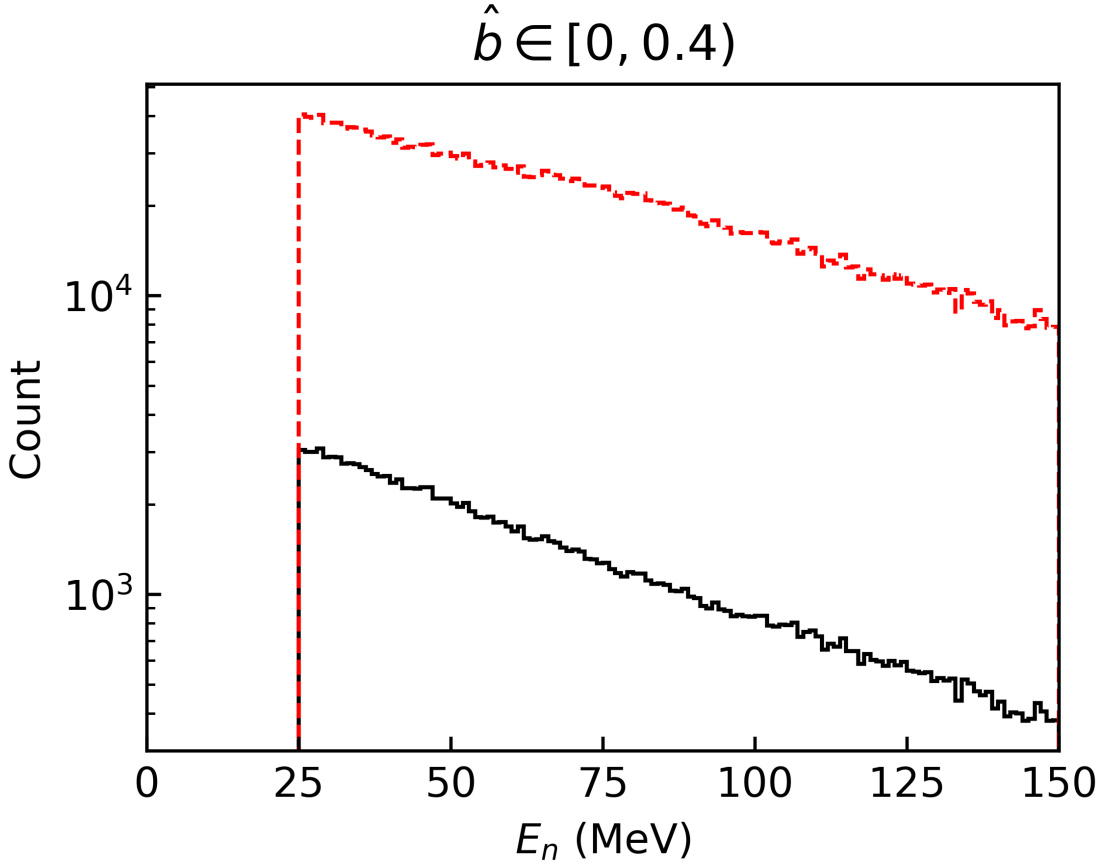

Figure 4.16: Neutron energy spectrum measured by the front LANA from ^{48}Ca+^{64}Ni at $E/A = 140\ MeV$ reaction. The data come from a batch of continuous runs of around 18 hours. The Y-axis is counts per bin and the X-axis is neutron energy in MeV in lab frame. The black line represents the raw spectra and the red line shows the spectra after detection efficiency correction using the efficiency data from Fig. 4.15. All data shown here have a deduced impact parameter gate from [0,0.4).

the following transformation [108]:

$$\frac{d^2\sigma}{d\Omega_{lab}dE_{lab}} = \frac{N}{2(\pi T)^{3/2}}(E^{'})^{1/2}exp[-(E^{''})/T] \tag{4.6}$$

$$E^{'} = E_{lab} - E_c \tag{4.7}$$

$$E^{''} = E^{'} - 2\sqrt{E^{'}(\frac{1}{2}mV_s^2)}cos(\theta_{lab}) + \frac{1}{2}mV_s^2 \tag{4.8}$$

where θ_{lab} is the emitting angle measured in lab frame, m is the mass of the emitted particle and E_{lab} is the energy of the emitted particle measured in lab frame. To do this moving source fit for figure 4.17, because neutron has no charge, we set E_c to be 0. T, N and V_s are the global free parameters for 3 spectra with different angular cuts. The surface temperature is determined to be 26±1 MeV from the fitting using moving source model. The best fit value for the source velocity V_s is found to be 0.48 times of the beam velocity. The extracted temperature is consistent with a mid rapidity source created in heavy ion collisions at 140 MeV/u incident energy[1]. Consider the case of a moving black body: its black body spectrum shows a frequency shift due to the relativistic Doppler effect which depends on the angle α between the observer and the source: $f' = f\frac{1-\frac{v}{c}cos(\theta)}{\sqrt{1-(\frac{v}{c})^2}}$. This leads to an angle dependent temperature and the observer will not detect an isotropic black body spectrum [109, 110].

[1]Transformation assumes same temperature in the center-of-mass frame. However, recent studies suggest that the temperature could be different in different frame.

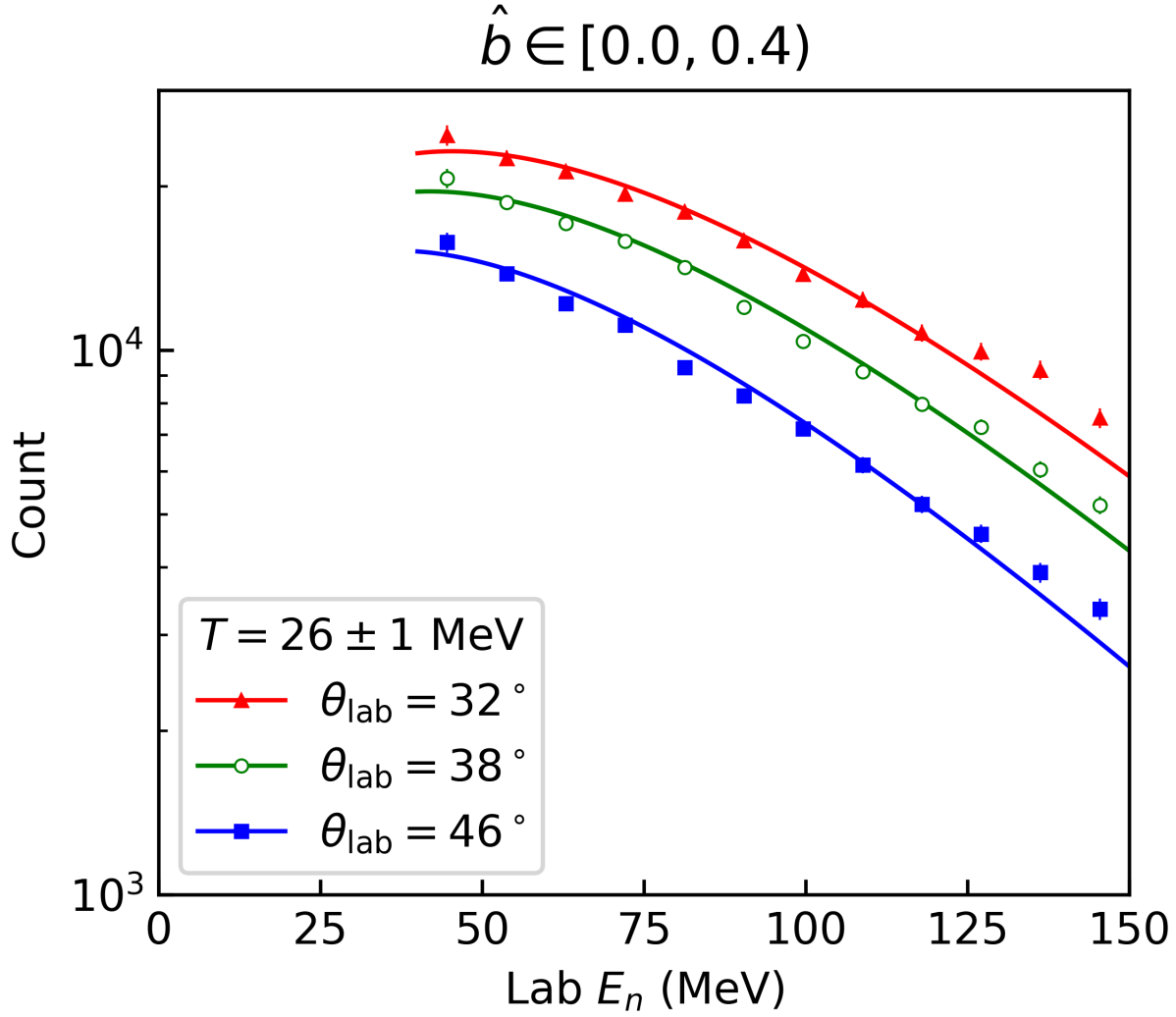

Figure 4.17: Neutron energy spectrum from ^{48}Ca+^{64}Ni at $E/A = 140\ MeV$ reaction with angular cuts. The Y-axis is count per bin from a batch of continuous runs of ^{48}Ca+^{64}Ni at $E/A = 140\ MeV$ reaction and the X-axis is neutron energy in MeV in lab frame. The error bars only reflect statistical uncertainties. From red, green and blue lines, different polar angular cuts from around 32°, 38° and 46° are applied respectively. Solid lines show the result after fitting with moving source model. The surface temperature of the moving source model is extracted to be 26±1 MeV. Similar moving source fits of the proton spectra in the same angular range yield similar results.

Chapter 5

Summary

The goal of detecting neutrons in experiment 14030 and 15190 is to construct neutron/proton ratios observable to study the symmetry energy. Detection of the charged-particles (including protons) using the upgraded HiRA10 array has been analyzed. This dissertation describes the initial effort to analyze the neutrons.

Following is a list of major improvements of this thesis experiment compared to the earlier version of experiment done in our group:

1. Full removal of charged-particle contamination from neutron spectra using the newly-built Charged-Particle Veto Wall.

2. Development of an innovative method that can calibrate the time, position and light output of neutron scintillation detectors using only cosmic rays.

3. Development of a new algorithm for neutron/γ pulse shape discrimination using VPSD method.

4. Measurement of charged-particles with greater extended kinetic energy ranges. For example, HiRA10 can measure protons with kinetic energy up to 200 MeV, compared to 116 MeV for the original HiRA.

The ability to fully remove charged-particle contaminations from neutron spectra is one of the essential requirements to successfully compare experimental n/p yield ratios with

simulation results, especially for the high kinetic energy regions where the observable of yield is much more sensitive to the effective mass splitting as shown in Fig. 1.3. By successfully vetoing the charged-particles in the LANA walls, we can successfully measure the neutron energy spectra beyond 200 MeV which was not achieved in previous study.

This thesis describes the measurement of neutrons emitted in heavy ion collisions. In experiment E14030 and 15190, we studied 16 reaction systems including 2 beam isotopes of ^{40}Ca and ^{48}Ca, 2 beam energies of E/A = 56 MeV and 140 MeV, and 4 targets of ^{58}Ni, ^{64}Ni, ^{112}Sn and ^{124}Sn. Neutrons and charged-particles were measured in these reaction systems in order to ultimately identify and construct observables that are sensitive to symmetry energy, and extract EoS constraints using transport calculations.

The major part of this dissertation focuses on the measurements of neutrons with improved detection equipment and analysis methods. A Forward Array used as the start timing detector for the neutron wall, was upgraded to increase its forward angle coverage. A new Charged-Particle Veto Wall was designed, constructed and placed in front of LANA to produce clean neutron spectrum without charged-particle contamination. An accurate, fast and convenient calibration method of LANA using cosmic muons was tested [111] and used to determine the intrinsic timing and position resolution of the LANA. Amazingly, the resolution is nearly the same as 20 years ago. We also developed a new neutron/γ discrimination procedure based on LANA's PSD capability which can better separate neutrons from gammas when compared to the traditional method. The discrimination provides accurate quantitative gamma contamination and neutron loss estimation [16] suggesting that PSD is needed in heavy ion collisions as contamination from gammas reaches 50 percent for high energy neutrons. We found that neutron light output spectrum acquired from LANA is comparable to the simulation results of SCINFUL-QMD code [5] by adjusting the attenuation length

parameter in the code. This allows us to use SCINFUL to simulate the neutron efficiencies of LANA from 10 to 100 MeV neutrons. To validate the analysis procedure, we generate the efficiency corrected neutron spectra for ^{48}Ca+^{64}Ni reactions at $E/A = 140\,MeV$. Using a moving source model, the source's surface temperature (20±1 MeV) and velocity (0.5 v_{beam}) are extracted. These parameters are reasonable and similar to those extracted from the proton spectra.

Due to the complexity of the experiment and the large amount of data acquired (27 TB), only the neutrons emitted in two reactions and WallB of the two LANA walls have been studied in details. The data presented in this dissertation mainly comes from ^{48}Ca+^{124}Sn and ^{48}Ca+^{64}Ni reaction system to demonstrate various analysis procedures needed for neutron measurements. Care is needed to extend the analysis to the remaining 14 systems. This thesis provides more of a preview of the data to come than a conclusion of the project. More careful investigation in the future is needed to validate every analysis step and determine the corresponding uncertainties. On the transport model side, efforts are being taken to identify better observables and address uncertainties in the simulations of heavy ion collisions.

BIBLIOGRAPHY

BIBLIOGRAPHY

[1] A. Klett, *Neutron Detection*, pp. 759–790. Berlin, Heidelberg: Springer Berlin Heidelberg, 2012.

[2] B. Alex Brown, "Neutron radii in nuclei and the neutron equation of state," *Phys. Rev. Lett.*, vol. 85, pp. 5296–5299, Dec 2000.

[3] M. B. Tsang, J. R. Stone, F. Camera, P. Danielewicz, S. Gandolfi, K. Hebeler, C. J. Horowitz, J. Lee, W. G. Lynch, Z. Kohley, R. Lemmon, P. Möller, T. Murakami, S. Riordan, X. Roca-Maza, F. Sammarruca, A. W. Steiner, I. Vidaña, and S. J. Yennello, "Constraints on the symmetry energy and neutron skins from experiments and theory," *Phys. Rev. C*, vol. 86, p. 015803, Jul 2012.

[4] Y. Zhang, M. Tsang, Z. Li, and H. Liu, "Constraints on nucleon effective mass splitting with heavy ion collisions," *Physics Letters B*, vol. 732, pp. 186 – 190, 2014.

[5] D. Satoh, T. Sato, N. Shigyo, and K. Ishibashi, "Scinful-qmd: Monte carlo based computer code to calculate response function and detection efficiency of a liquid organic scintillator for neutron energies up to 3 gev."

[6] D. D. S. Coupland, M. Youngs, Z. Chajecki, W. G. Lynch, M. B. Tsang, Y. X. Zhang, M. A. Famiano, T. K. Ghosh, B. Giacherio, M. A. Kilburn, J. Lee, H. Liu, F. Lu, P. Morfouace, P. Russotto, A. Sanetullaev, R. H. Showalter, G. Verde, and J. Winkelbauer, "Probing effective nucleon masses with heavy-ion collisions," *Phys. Rev. C*, vol. 94, p. 011601, Jul 2016.

[7] P. Morfouace, C. Tsang, Y. Zhang, W. Lynch, M. Tsang, D. Coupland, M. Youngs, Z. Chajecki, M. Famiano, T. Ghosh, G. Jhang, J. Lee, H. Liu, A. Sanetullaev, R. Showalter, and J. Winkelbauer, "Constraining the symmetry energy with heavy-ion collisions and bayesian analyses," *Physics Letters B*, vol. 799, p. 135045, 2019.

[8] P. Morfouace, W. Lynch, and M. Tsang, "Charged-particle detection efficiencies of close-packed csi arrays," *Nuclear Instruments and Methods in Physics Research Section A: Accelerators, Spectrometers, Detectors and Associated Equipment*, vol. 848, pp. 45 – 53, 2017.

[9] D. Coupland, *Probing the nuclear symmetry energy with heavy ion collisions*. PhD thesis, Michigan State University, 2013.

[10] D. Sarantites, P.-F. Hua, M. Devlin, L. Sobotka, J. Elson, J. Hood, D. LaFosse, J. Sarantites, and M. Maier, "The microball design, instrumentation and response

characteristics of a 4Ï-multidetector exit channel-selection device for spectroscopic and reaction mechanism studies with gammasphere," *Nuclear Instruments and Methods in Physics Research Section A: Accelerators, Spectrometers, Detectors and Associated Equipment*, vol. 381, no. 2, pp. 418 – 432, 1996.

[11] "Faroarm."

[12] D. DellâAquila, S. Sweany, K. Brown, Z. Chajecki, W. Lynch, F. Teh, C.-Y. Tsang, M. Tsang, K. Zhu, C. Anderson, A. Anthony, S. Barlini, J. Barney, A. Camaiani, G. Jhang, J. Crosby, J. Estee, M. Ghazali, F. Guan, O. Khanal, S. Kodali, I. Lombardo, J. Manfredi, L. Morelli, P. Morfouace, C. Niu, and G. Verde, "Non-linearity effects on the light-output calibration of light charged particles in csi(tl) scintillator crystals," *Nuclear Instruments and Methods in Physics Research Section A: Accelerators, Spectrometers, Detectors and Associated Equipment*, vol. 929, pp. 162 – 172, 2019.

[13] P. Zecher, A. Galonsky, J. Kruse, S. Gaff, J. Ottarson, J. Wang, F. Deák, A. Horváth, A. Kiss, Z. Seres, K. Ieki, Y. Iwata, and H. Schelin, "A large-area, position-sensitive neutron detector with neutron/γ-ray discrimination capabilities," *Nuclear Instruments and Methods in Physics Research Section A: Accelerators, Spectrometers, Detectors and Associated Equipment*, vol. 401, no. 2, pp. 329 – 344, 1997.

[14] "Faro vantage laser trackers."

[15] R. H. Showalter, *Determination of density and momentum dependence of nuclear symmetry potentials with asymmetric heavy ion reactions*. PhD thesis, Michigan State University, 2015.

[16] F.C.E. Teh, "Value-assigned pulse shape discrimination for neutron detectors," 2020.

[17] E. Rutherford, "Retardation of the alpha particle from radium in passing through matter," *Philosophical Magazine*, vol. 12, pp. 134–146, 1906.

[18] C. J., "The existence of a neutron," *Proc. Roy. Soc. A*, vol. 136, pages = 692-708, year = 1932,.

[19] W. D. Myers and W. J. Swiatecki, "Nuclear masses and deformations," *Nuclear Physics*, vol. 81, no. 1, pp. 1 – 60, 1966.

[20] W. D. Myers, "Droplet model nuclear density distributions and single-particle potential wells," *Nuclear Physics A*, vol. 145, no. 2, pp. 387 – 400, 1970.

[21] M. Bender, P.-H. Heenen, and P.-G. Reinhard, "Self-consistent mean-field models for nuclear structure," *Rev. Mod. Phys.*, vol. 75, pp. 121–180, Jan 2003.

[22] M. Baldo and G. Burgio, "The nuclear symmetry energy," *Progress in Particle and Nuclear Physics*, vol. 91, pp. 203 – 258, 2016.

[23] B.-A. Li, "Nuclear symmetry energy extracted from laboratory experiments," *Nuclear Physics News*, vol. 27, no. 4, pp. 7–11, 2017.

[24] J. M. Lattimer and M. Prakash, "Neutron star structure and the equation of state," *The Astrophysical Journal*, vol. 550, pp. 426–442, mar 2001.

[25] H. Shen, "Complete relativistic equation of state for neutron stars," *Phys. Rev. C*, vol. 65, p. 035802, Feb 2002.

[26] D. Page, J. M. Lattimer, M. Prakash, and A. W. Steiner, "Minimal cooling of neutron stars: A new paradigm," *The Astrophysical Journal Supplement Series*, vol. 155, pp. 623–650, dec 2004.

[27] A. Steiner, M. Prakash, J. Lattimer, and P. Ellis, "Isospin asymmetry in nuclei and neutron stars," *Physics Reports*, vol. 411, no. 6, pp. 325 – 375, 2005.

[28] A. W. Steiner, "Neutron star inner crust: Nuclear physics input," *Phys. Rev. C*, vol. 77, p. 035805, Mar 2008.

[29] B. G. Todd-Rutel and J. Piekarewicz, "Neutron-rich nuclei and neutron stars: A new accurately calibrated interaction for the study of neutron-rich matter," *Phys. Rev. Lett.*, vol. 95, p. 122501, Sep 2005.

[30] J. M. Lattimer and M. Prakash, "The physics of neutron stars," *Science*, vol. 304, no. 5670, pp. 536–542, 2004.

[31] B. P. Abbott et al, "Gw170817: Observation of gravitational waves from a binary neutron star inspiral," *Phys. Rev. Lett.*, vol. 119, p. 161101, Oct 2017.

[32] B. P. Abbott et al, "Gw170817: Measurements of neutron star radii and equation of state," *Phys. Rev. Lett.*, vol. 121, p. 161101, Oct 2018.

[33] B. P. Abbott et al, "Properties of the binary neutron star merger gw170817," *Phys. Rev. X*, vol. 9, p. 011001, Jan 2019.

[34] K. Chatziioannou, C.-J. Haster, and A. Zimmerman, "Measuring the neutron star tidal deformability with equation-of-state-independent relations and gravitational waves," *Phys. Rev. D*, vol. 97, p. 104036, May 2018.

[35] M. Tsang, W. Lynch, P. Danielewicz, and C. Tsang, "Symmetry energy constraints from gw170817 and laboratory experiments," *Physics Letters B*, vol. 795, pp. 533 – 536, 2019.

[36] C. Tsang, M. Tsang, P. Danielewicz, F. Fattoyev, and W. Lynch, "Insights on skyrme parameters from gw170817," *Physics Letters B*, vol. 796, pp. 1 – 5, 2019.

[37] P. Danielewicz, P. Singh, and J. Lee, "Symmetry energy iii: Isovector skins," *Nuclear Physics A*, vol. 958, pp. 147 – 186, 2017.

[38] A. Klimkiewicz, N. Paar, P. Adrich, M. Fallot, K. Boretzky, T. Aumann, D. Cortina-Gil, U. D. Pramanik, T. W. Elze, H. Emling, H. Geissel, M. Hellström, K. L. Jones, J. V. Kratz, R. Kulessa, C. Nociforo, R. Palit, H. Simon, G. Surówka, K. Sümmerer, D. Vretenar, and W. Waluś, "Nuclear symmetry energy and neutron skins derived from pygmy dipole resonances," *Phys. Rev. C*, vol. 76, p. 051603, Nov 2007.

[39] O. Wieland and A. Bracco, "The pygmy dipole resonance in 68ni and the neutron skin," *Progress in Particle and Nuclear Physics*, vol. 66, no. 2, pp. 374 – 378, 2011. Particle and Nuclear Astrophysics.

[40] A. Carbone, G. Colò, A. Bracco, L.-G. Cao, P. F. Bortignon, F. Camera, and O. Wieland, "Constraints on the symmetry energy and neutron skins from pygmy resonances in ^{68}Ni and ^{132}Sn," *Phys. Rev. C*, vol. 81, p. 041301, Apr 2010.

[41] M. Kortelainen, T. Lesinski, J. Moré, W. Nazarewicz, J. Sarich, N. Schunck, M. V. Stoitsov, and S. Wild, "Nuclear energy density optimization," *Phys. Rev. C*, vol. 82, p. 024313, Aug 2010.

[42] B. A. Brown, "Constraints on the skyrme equations of state from properties of doubly magic nuclei," *Phys. Rev. Lett.*, vol. 111, p. 232502, Dec 2013.

[43] D. M. Rossi, P. Adrich, F. Aksouh, H. Alvarez-Pol, T. Aumann, J. Benlliure, M. Böhmer, K. Boretzky, E. Casarejos, M. Chartier, A. Chatillon, D. Cortina-Gil, U. Datta Pramanik, H. Emling, O. Ershova, B. Fernandez-Dominguez, H. Geissel, M. Gorska, M. Heil, H. T. Johansson, A. Junghans, A. Kelic-Heil, O. Kiselev, A. Klimkiewicz, J. V. Kratz, R. Krücken, N. Kurz, M. Labiche, T. Le Bleis, R. Lemmon, Y. A. Litvinov, K. Mahata, P. Maierbeck, A. Movsesyan, T. Nilsson, C. Nociforo, R. Palit, S. Paschalis, R. Plag, R. Reifarth, D. Savran, H. Scheit, H. Simon, K. Sümmerer, A. Wagner, W. Waluś, H. Weick, and M. Winkler, "Measurement of the dipole polarizability of the unstable neutron-rich nucleus ^{68}Ni," *Phys. Rev. Lett.*, vol. 111, p. 242503, Dec 2013.

[44] A. Tamii, I. Poltoratska, P. von Neumann-Cosel, Y. Fujita, T. Adachi, C. A. Bertulani, J. Carter, M. Dozono, H. Fujita, K. Fujita, K. Hatanaka, D. Ishikawa, M. Itoh, T. Kawabata, Y. Kalmykov, A. M. Krumbholz, E. Litvinova, H. Matsubara, K. Nakanishi, R. Neveling, H. Okamura, H. J. Ong, B. Özel-Tashenov, V. Y. Ponomarev, A. Richter, B. Rubio, H. Sakaguchi, Y. Sakemi, Y. Sasamoto, Y. Shimbara, Y. Shimizu, F. D. Smit, T. Suzuki, Y. Tameshige, J. Wambach, R. Yamada, M. Yosoi, and J. Zeni-

hiro, "Complete electric dipole response and the neutron skin in ^{208}Pb," *Phys. Rev. Lett.*, vol. 107, p. 062502, Aug 2011.

[45] Z. Zhang and L.-W. Chen, "Constraining the symmetry energy at subsaturation densities using isotope binding energy difference and neutron skin thickness," *Physics Letters B*, vol. 726, no. 1, pp. 234 – 238, 2013.

[46] H. S. Xu, M. B. Tsang, T. X. Liu, X. D. Liu, W. G. Lynch, W. P. Tan, A. Vander Molen, G. Verde, A. Wagner, H. F. Xi, C. K. Gelbke, L. Beaulieu, B. Davin, Y. Larochelle, T. Lefort, R. T. de Souza, R. Yanez, V. E. Viola, R. J. Charity, and L. G. Sobotka, "Isospin fractionation in nuclear multifragmentation," *Phys. Rev. Lett.*, vol. 85, pp. 716–719, Jul 2000.

[47] M. B. Tsang, T. X. Liu, L. Shi, P. Danielewicz, C. K. Gelbke, X. D. Liu, W. G. Lynch, W. P. Tan, G. Verde, A. Wagner, H. S. Xu, W. A. Friedman, L. Beaulieu, B. Davin, R. T. de Souza, Y. Larochelle, T. Lefort, R. Yanez, V. E. Viola, R. J. Charity, and L. G. Sobotka, "Isospin diffusion and the nuclear symmetry energy in heavy ion reactions," *Phys. Rev. Lett.*, vol. 92, p. 062701, Feb 2004.

[48] M. B. Tsang, C. K. Gelbke, X. D. Liu, W. G. Lynch, W. P. Tan, G. Verde, H. S. Xu, W. A. Friedman, R. Donangelo, S. R. Souza, C. B. Das, S. Das Gupta, and D. Zhabinsky, "Isoscaling in statistical models," *Phys. Rev. C*, vol. 64, p. 054615, Oct 2001.

[49] H. L. Liu, F. R. Xu, S. W. Xu, R. Wyss, and P. M. Walker, "High-spin isomeric structures in exotic odd-odd nuclei: Exploration of the proton drip line and beyond," *Phys. Rev. C*, vol. 76, p. 034313, Sep 2007.

[50] Z. Y. Sun, M. B. Tsang, W. G. Lynch, G. Verde, F. Amorini, L. Andronenko, M. Andronenko, G. Cardella, M. Chatterje, P. Danielewicz, E. De Filippo, P. Dinh, E. Galichet, E. Geraci, H. Hua, E. La Guidara, G. Lanzalone, H. Liu, F. Lu, S. Lukyanov, C. Maiolino, A. Pagano, S. Piantelli, M. Papa, S. Pirrone, G. Politi, F. Porto, F. Rizzo, P. Russotto, D. Santonocito, and Y. X. Zhang, "Isospin diffusion and equilibration for Sn + Sn collisions at $e/a = 35$ mev," *Phys. Rev. C*, vol. 82, p. 051603, Nov 2010.

[51] S. F. Ban, J. Li, S. Q. Zhang, H. Y. Jia, J. P. Sang, and J. Meng, "Density dependencies of interaction strengths and their influences on nuclear matter and neutron stars in relativistic mean field theory," *Phys. Rev. C*, vol. 69, p. 045805, Apr 2004.

[52] B. Liu, V. Greco, V. Baran, M. Colonna, and M. Di Toro, "Asymmetric nuclear matter: The role of the isovector scalar channel," *Phys. Rev. C*, vol. 65, p. 045201, Mar 2002.

[53] K. A. Brueckner, "Two-body forces and nuclear saturation. iii. details of the structure of the nucleus," *Phys. Rev.*, vol. 97, pp. 1353–1366, Mar 1955.

[54] W. Zuo, A. Lejeune, U. Lombardo, and J.F. Mathiot, "Microscopic three-body force for asymmetric nuclear matter," *Eur. Phys. J. A*, vol. 14, no. 4, pp. 469–475, 2002.

[55] B.-A. Li, "Constraining the neutron-proton effective mass splitting in neutron-rich matter," *Phys. Rev. C*, vol. 69, p. 064602, Jun 2004.

[56] A. Lane, "Isobaric spin dependence of the optical potential and quasi-elastic (p, n) reactions," *Nuclear Physics*, vol. 35, pp. 676 – 685, 1962.

[57] B.-A. Li and X. Han, "Constraining the neutron–proton effective mass splitting using empirical constraints on the density dependence of nuclear symmetry energy around normal density," *Physics Letters B*, vol. 727, no. 1, pp. 276 – 281, 2013.

[58] J. Dobaczewski, "Structure of nuclei at extreme values of the isospin," *ACTA PHYSICA POLONICA B*, vol. 30, p. 1647, 1999.

[59] M. Baldo, G. F. Burgio, H.-J. Schulze, and G. Taranto, "Nucleon effective masses within the brueckner-hartree-fock theory: Impact on stellar neutrino emission," *Phys. Rev. C*, vol. 89, p. 048801, Apr 2014.

[60] O. Sjoberg, "On the Landau effective mass in asymmetric nuclear matter," *Nucl. Phys. A*, vol. 265, pp. 511–516, July 1976.

[61] W. Zuo, A. Lejeune, U. Lombardo, and J.F. Mathiot, "Microscopic three-body force for asymmetric nuclear matter," *Eur. Phys. J. A*, vol. 14, no. 4, pp. 469–475, 2002.

[62] F. Hofmann, C. M. Keil, and H. Lenske, "Density dependent hadron field theory for asymmetric nuclear matter and exotic nuclei," *Phys. Rev. C*, vol. 64, p. 034314, Aug 2001.

[63] P. Danielewicz, R. Lacey, and W. G. Lynch, "Determination of the equation of state of dense matter," *Science*, vol. 298, no. 5598, pp. 1592–1596, 2002.

[64] B.-A. Li, L.-W. Chen, and C. M. Ko, "Recent progress and new challenges in isospin physics with heavy-ion reactions," *Physics Reports*, vol. 464, no. 4, pp. 113 – 281, 2008.

[65] Y. Zhang, D. D. S. Coupland, P. Danielewicz, Z. Li, H. Liu, F. Lu, W. G. Lynch, and M. B. Tsang, "Influence of in-medium nn cross sections, symmetry potential, and impact parameter on isospin observables," *Phys. Rev. C*, vol. 85, p. 024602, Feb 2012.

[66] M. A. Famiano, T. Liu, W. G. Lynch, M. Mocko, A. M. Rogers, M. B. Tsang, M. S. Wallace, R. J. Charity, S. Komarov, D. G. Sarantites, L. G. Sobotka, and G. Verde, "Neutron and proton transverse emission ratio measurements and the density dependence of the asymmetry term of the nuclear equation of state," *Phys. Rev. Lett.*, vol. 97, p. 052701, Aug 2006.

[67] M. B. Tsang, Y. Zhang, P. Danielewicz, M. Famiano, Z. Li, W. G. Lynch, and A. W. Steiner, "Constraints on the density dependence of the symmetry energy," *Phys. Rev. Lett.*, vol. 102, p. 122701, Mar 2009.

[68] T. X. Liu, W. G. Lynch, M. B. Tsang, X. D. Liu, R. Shomin, W. P. Tan, G. Verde, A. Wagner, H. F. Xi, H. S. Xu, B. Davin, Y. Larochelle, R. T. d. Souza, R. J. Charity, and L. G. Sobotka, "Isospin diffusion observables in heavy-ion reactions," *Phys. Rev. C*, vol. 76, p. 034603, Sep 2007.

[69] W. G. Lynch and M. B. Tsang, "The nuclear symmetry energy at sub-saturation densities," 2018.

[70] P. Danielewicz, "Determination of the mean-field momentum-dependence using elliptic flow," *Nuclear Physics A*, vol. 673, no. 1, pp. 375 – 410, 2000.

[71] N. Wang, Z. Li, and X. Wu, "Improved quantum molecular dynamics model and its applications to fusion reaction near barrier," *Phys. Rev. C*, vol. 65, p. 064608, May 2002.

[72] N. Wang, X. Wu, and Z. Li, "Dynamic study of fusion reactions for ^{40,48}Ca+^{90,96}Zr around the coulomb barrier," *Phys. Rev. C*, vol. 67, p. 024604, Feb 2003.

[73] N. Wang, Z. Li, X. Wu, J. Tian, Y. Zhang, and M. Liu, "Further development of the improved quantum molecular dynamics model and its application to fusion reactions near the barrier," *Phys. Rev. C*, vol. 69, p. 034608, Mar 2004.

[74] Douchin, F. and Haensel, P., "A unified equation of state of dense matter and neutron star structure," *Astron. Astrophys.*, vol. 380, no. 1, pp. 151–167, 2001.

[75] J. Bartel, P. Quentin, M. Brack, C. Guet, and H.-B. HÃ¥kansson, "Towards a better parametrisation of skyrme-like effective forces: A critical study of the skm force," *Nuclear Physics A*, vol. 386, no. 1, pp. 79 – 100, 1982.

[76] G. F. Knoll, *Radiation detection and measurement; 4th ed.* New York, NY: Wiley, 2010.

[77] M. Wallace, M. Famiano, M.-J. van Goethem, A. Rogers, W. Lynch, J. Clifford, F. Delaunay, J. Lee, S. Labostov, M. Mocko, L. Morris, A. Moroni, B. Nett, D. Oostdyk, R. Krishnasamy, M. Tsang, R. de Souza, S. Hudan, L. Sobotka, R. Charity, J. Elson, and G. Engel, "The high resolution array (hira) for rare isotope beam experiments," *Nuclear Instruments and Methods in Physics Research Section A: Accelerators, Spectrometers, Detectors and Associated Equipment*, vol. 583, no. 2, pp. 302 – 312, 2007.

[78] B. Davin, R. de Souza, R. Yanez, Y. Larochelle, R. Alfaro, H. Xu, A. Alexander, K. Bastin, L. Beaulieu, J. Dorsett, G. Fleener, L. Gelovani, T. Lefort, J. Poehlman,

R. Charity, L. Sobotka, J. Elson, A. Wagner, T. Liu, X. Liu, W. Lynch, L. Morris, R. Shomin, W. Tan, M. Tsang, G. Verde, and J. Yurkon, "Lassa: a large area silicon strip array for isotopic identification of charged particles," *Nuclear Instruments and Methods in Physics Research Section A: Accelerators, Spectrometers, Detectors and Associated Equipment*, vol. 473, no. 3, pp. 302 – 318, 2001.

[79] E. Pollacco, D. Beaumel, P. Roussel-Chomaz, E. Atkin, P. Baron, J. P. Baronick, E. Becheva, Y. Blumenfeld, A. Boujrad, A. Drouart, F. Druillole, P. Edelbruck, M. Gelin, A. Gillibert, C. Houarner, V. Lapoux, L. Lavergne, G. Leberthe, L. Leterrier, V. Le Ven, F. Lugiez, L. Nalpas, L. Olivier, B. Paul, B. Raine, A. Richard, M. Rouger, F. Saillant, F. Skaza, M. Tripon, M. Vilmay, E. Wanlin, and M. Wittwer, "Must2: A new generation array for direct reaction studies," in *The 4th International Conference on Exotic Nuclei and Atomic Masses* (C. J. Gross, W. Nazarewicz, and K. P. Rykaczewski, eds.), (Berlin, Heidelberg), pp. 287–288, Springer Berlin Heidelberg, 2005.

[80] L. Acosta, E. Pagano, T. Minniti, G. Verde, F. Amorini, A. Anzalone, L. Auditore, M. Buscemi, G. Cardella, A. Chbihi, E. De Filippo, L. Francalanza, E. Geraci, S.GianÃ¬, C. Guazzoni, E. Guidara, G. Lanzalone, I. Lombardo, S. Nigro, and M. Vigilante, "Farcos, a new array for femtoscopy and correlation spectroscopy," *The European Physical Journal Conferences*, vol. 31, pp. 1–8, 07 2012.

[81] Eljen Technologies, "Ej-301," 2016.

[82] J. Scherzinger, R. A. Jebali, J. Annand, K. Fissum, R. Hall-Wilton, K. Kanaki, M. Lundin, B. Nilsson, H. Perrey, A. Rosborg, and H. Svensson, "The light-yield response of a ne-213 liquid-scintillator detector measured using 2â6mev tagged neutrons," *Nuclear Instruments and Methods in Physics Research Section A: Accelerators, Spectrometers, Detectors and Associated Equipment*, vol. 840, pp. 121 – 127, 2016.

[83] "Costruzioni apparecchiature elettroniche nucleari s.p.a.."

[84] "Lecroy corporation."

[85] M. Youngs, *Using light emitted clusters as a probe of the symmetry energy in the nuclear equation of state*. PhD thesis, Michigan State University, 2013.

[86] "MSU Electrical and Computer Engineering Department ECE Testing Facility."

[87] Eljen Technologies, "EJ-200," 2016.

[88] R. D. Souza, N. Carlin, Y. Kim, J. Ottarson, L. Phair, D. Bowman, C. Gelbke, W. Gong, W. Lynch, R. Pelak, T. Peterson, G. Poggi, M. Tsang, and H. Xu, "The msu miniball 4Ï fragment detection array," *Nuclear Instruments and Methods in Physics*

Research Section A: Accelerators, Spectrometers, Detectors and Associated Equipment, vol. 295, no. 1, pp. 109 – 122, 1990.

[89] SYLGARD tech, "Sylgard 182 silicone elastomer."

[90] C. Cavata, M. Demoulins, J. Gosset, M.-C. Lemaire, D. L'Hôte, J. Poitou, and O. Valette, "Determination of the impact parameter in relativistic nucleus-nucleus collisions," *Phys. Rev. C*, vol. 42, pp. 1760–1763, Oct 1990.

[91] T. X. Liu, W. G. Lynch, R. H. Showalter, M. B. Tsang, X. D. Liu, W. P. Tan, M. J. van Goethem, G. Verde, A. Wagner, H. F. Xi, H. S. Xu, M. A. Famiano, R. T. de Souza, V. E. Viola, R. J. Charity, and L. G. Sobotka, "Isospin observables from fragment energy spectra," *Phys. Rev. C*, vol. 86, p. 024605, Aug 2012.

[92] J. R. Winkelbauer, *PRECISION MEASUREMENT OF ISOSPIN DIFFUSION IN PERIPHERAL SN+SN COLLISIONS AT 70 MEV/U*. PhD thesis, Michigan State University, 2015.

[93] L. Phair, D. Bowman, C. Gelbke, W. Gong, Y. Kim, M. Lisa, W. Lynch, G. Peaslee, R. de Souza, M. Tsang, and F. Zhu, "Impact-parameter filters for 36ar+197au collisions at ea = 50, 80 and 110 mev," *Nuclear Physics A*, vol. 548, no. 3, pp. 489 – 509, 1992.

[94] Y. D. Kim, R. T. de Souza, D. R. Bowman, N. Carlin, C. K. Gelbke, W. G. Gong, W. G. Lynch, L. Phair, M. B. Tsang, and F. Zhu, "Intermediate mass fragment emission in ^{36}Ar+^{197}au collisions at e/a=35 mev," *Phys. Rev. C*, vol. 45, pp. 338–352, Jan 1992.

[95] K. Drozdowicz, M. Hoek, and D. Aronsson, "Energy calibration of neutron detectors for the neutron spectrometer tansy," *Nuclear Instruments and Methods in Physics Research Section A: Accelerators, Spectrometers, Detectors and Associated Equipment*, vol. 306, no. 1, pp. 315 – 330, 1991.

[96] S. Meigo, "Measurements of the response function and the detection efficiency of an ne213 scintillator for neutrons between 20 and 65 mev," *Nuclear Instruments and Methods in Physics Research Section A: Accelerators, Spectrometers, Detectors and Associated Equipment*, vol. 401, no. 2, pp. 365 – 378, 1997.

[97] N. Nakao, T. Kurosawa, T. Nakamura, and Y. Uwamino, "Absolute measurements of the response function of an ne213 organic liquid scintillator for the neutron energy range up to 206 mev," *Nuclear Instruments and Methods in Physics Research Section A: Accelerators, Spectrometers, Detectors and Associated Equipment*, vol. 463, no. 1, pp. 275 – 287, 2001.

[98] W. Betts, F. Bieser, R. Bossingham, M. Botlo, M. Cherney, J. Chrin, P. Colarco, H. Crawford, K. Dao, H. Diaz, D. E. Greiner, L. Greiner, E. L. Hjort, S. Jacobson, R. C. Jared, E. Judd, S. R. Klein, A. N. Lebedev, M. J. LeVine, V. Lindenstruth, M. A.

Lisa, K. Marks, C. McParland, T. S. McShane, J. Meier, M. T. Nguyen, D. L. Olson, I. Sakrejda, J. Schambach, R. A. Scheetz, N. T. B. Stone, C. E. Tull, G. Visser, C. Vu, H. Wieman, and E. Yee, "Results from the star tpc system test," *IEEE Transactions on Nuclear Science*, vol. 44, pp. 592–597, June 1997.

[99] B. C. Rastin, "An accurate measurement of the sea-level muon spectrum within the range 4 to 3000 GeV/c," *Journal of Physics G: Nuclear Physics*, vol. 10, pp. 1609–1628, nov 1984.

[100] J. Wiechula, "Commissioning and calibration of the alice tpc," *Nuclear Physics A*, vol. 830, no. 1, pp. 531c – 534c, 2009. Quark Matter 2009.

[101] C. Hagmann, D. Lange, and D. Wright, "Cosmic-ray shower generator (cry) for monte carlo transport codes," in *2007 IEEE Nuclear Science Symposium Conference Record*, vol. 2, pp. 1143–1146, Oct 2007.

[102] "Physical constants," *Physics Letters B*, vol. 204, pp. IN3 – 127, 1988.

[103] E. Siciliano, J. Ely, R. Kouzes, J. Schweppe, D. Strachan, and S. Yokuda, "Energy calibration of gamma spectra in plastic scintillators using compton kinematics," *Nuclear Instruments and Methods in Physics Research Section A: Accelerators, Spectrometers, Detectors and Associated Equipment*, vol. 594, no. 2, pp. 232 – 243, 2008.

[104] NSCL, GANIL, GSI, and RIKEN, "LISE," 2003.

[105] F. Brooks, "A scintillation counter with neutron and gamma-ray discriminators," *Nuclear Instruments and Methods*, vol. 4, no. 3, pp. 151 – 163, 1959.

[106] N. Zaitseva, B. L. Rupert, I. Paweaczak, A. Glenn, H. P. Martinez, L. Carman, M. Faust, N. Cherepy, and S. Payne, "Plastic scintillators with efficient neutron/gamma pulse shape discrimination," *Nuclear Instruments and Methods in Physics Research Section A: Accelerators, Spectrometers, Detectors and Associated Equipment*, vol. 668, pp. 88 – 93, 2012.

[107] R. Wada, D. Fabris, K. Hagel, G. Nebbia, Y. Lou, M. Gonin, J. B. Natowitz, R. Billerey, B. Cheynis, A. Demeyer, D. Drain, D. Guinet, C. Pastor, L. Vagneron, K. Zaid, J. Alarja, A. Giorni, D. Heuer, C. Morand, B. Viano, C. Mazur, C. Ng, S. Leray, R. Lucas, M. Ribrag, and E. Tomasi, "Temperatures and excitation energies of hot nuclei in the reactions of ^{32}S+ag and ^{16}O+ag at 30 mev/nucleon," *Phys. Rev. C*, vol. 39, pp. 497–515, Feb 1989.

[108] R. Wang, *Investigating the symmetry energy effect in fission reaction from the emission of the light charged-particle.* PhD thesis, Tsinghua University, 2015.

[109] P. Landsberg and G. Matsas, "The impossibility of a universal relativistic temperature transformation," *Physica A: Statistical Mechanics and its Applications*, vol. 340, no. 1, pp. 92 – 94, 2004. News and Expectations in Thermostatistics.

[110] P. T. Landsberg and G. E. Matsas, "Laying the ghost of the relativistic temperature transformation," *Physics Letters A*, vol. 223, no. 6, pp. 401 – 403, 1996.

[111] K. Zhu, M. Tsang, D. Dell'Aquila, K. Brown, Z. Chajecki, W. Lynch, S. Sweany, F. Teh, C. Tsang, C. Anderson, A. Anthony, J. Barney, J. Crosby, J. Estee, I. Gasparic, G. Jhang, O. Khanal, S. Kodali, J. Manfredi, C. Niu, and R. Wang, "Calibration of large neutron detection arrays using cosmic rays," *Nuclear Instruments and Methods in Physics Research Section A: Accelerators, Spectrometers, Detectors and Associated Equipment*, vol. 967, p. 163826, 2020.